Title

INFRARED EMISSION SPECTROSCOPY OF CARBON MONOXIDE ON NICKEL

Author

Chiang, S.

Publication Date

1983-05-01

Thesis/dissertation

Lawrence Berkeley Laboratory
UNIVERSITY OF CALIFORNIA

Materials & Molecular Research Division

INFRARED EMISSION SPECTROSCOPY OF CARBON MONOXIDE ON NICKEL

S. Chiang
(Ph.D. Thesis)

May 1983

Prepared for the U.S. Department of Energy under Contract DE-AC03-76SF00098

DISCLAIMER

LBL-16151

INFRARED EMISSION SPECTROSCOPY OF CARBON MONOXIDE ON NICKEL

Shirley Chiang
(Ph.D. Thesis)

Lawrence Berkeley Laboratory
University of California
Berkeley, California 94720

May 1983

This work was supported by the Director, Office of Energy Research, Office of Basic Energy Sciences, Materials Sciences Division of the U.S. Department of Energy under Contract Number DE-AC03-76SF00098.

TABLE OF CONTENTS

LIST OF FIGURES

LIST OF TABLES

INFRARED EMISSION SPECTROSCOPY OF CARBON MONOXIDE ON NICKEL

Shirley Chiang

Department of Physics, University of California, Berkeley
and Materials and Molecular Research Division,
Lawrence Berkeley Laboratory
Berkeley, California 94720

ABSTRACT

The technique of infrared emission spectroscopy has been developed in order to observe vibrational modes of molecules adsorbed on clean, single crystal metal surfaces. A novel apparatus which measures the emission from a single crystal sample in thermal equilibrium at room temperature has been designed and built. The apparatus consists of a liquid helium cooled infrared grating spectrometer coupled to an ultrahigh vacuum system equipped with surface preparation and characterization facilities. The system is capable of measuring the range of frequencies from 330 to 3000 cm^{-1} with a resolution of 1 to 15 cm^{-1}. The apparatus is currently able to measure a molecular surface signal which is 5×10^{-4} of the bulk emission signal.

Using the infrared emission technique, we have made the first measurement of the linewidth of the molecule-substrate vibration of monolayer coverage of CO on Ni(100). The line position is 472 cm^{-1}, and the observed linewidth is 15 cm^{-1}, which is unexpectedly broad. We have also observed the carbon-oxygen stretching vibration from CO on Ni(100) as a function of coverage, measuring the frequencies and linewidths of both on-top and bridge site bands.

I. INTRODUCTION

Many chemical reactions take place at surfaces and interfaces between media. Therefore, it is important to learn about the properties of surfaces in order to better understand the reactions which can take place there. In particular, the study of the solid-gas interface has relevance to many practical problems, including heterogeneous catalysis, corrosion, and integrated circuits. But since complex chemical reactions at a surface are difficult to understand, surface scientists usually prefer to study first the properties of clean, single crystal surfaces on which well controlled experiments can be performed.

The development of ultrahigh vacuum technology in the last 20 years enabled the growth of surface science as a viable field of study. If the sticking coefficient is one, and the density of adsorption sites is $3 \times 10^{14}/cm^2$, an exposure of one Langmuir ($1L = 10^{-6}$ torr for one second) will cause one monolayer of molecules to stick to a clean surface.[1] Thus, the use of ultrahigh vacuum environments is necessary in order to permit a reasonable amount of time in which to perform an experiment on a clean surface. When the pressure in the vicinity of the sample is reduced to about 10^{-10} torr, about two and a half hours elapse before one monolayer of molecules can accumulate on the surface.

Surface structure and composition both have an important role in surface reactions. The careful characterization of surfaces can lead to an understanding of the relationships between the properties of the surface and the chemical reactions which can take place there. Many techniques exist for studying the properties of surfaces. Each one yields information of a specific type about the surface. For example,

low energy electron diffraction (LEED) gives information about the structure of the surface, while Auger electron spectroscopy shows lines characteristic of the types of atomic species on the surface.[2] By combining several complementary techniques, we can put together a more complete picture of the surface and the interactions there.

Vibrational spectroscopy is an important tool for the study of surfaces because it can give information on the chemical bonds at the surface. It can be used to identify the types of adsorbed atoms and molecules on a surface. It can also yield information on adsorption sites and on the geometrical arrangement of the atoms of adsorbed molecules. Bond strengths and distances can be determined from the vibrational frequencies. In addition, linewidth information can be used to study relaxation effects and coupling between vibrational modes.[3]

Many techniques can be used to obtain vibrational spectra, but each has its own advantages and limitations. In electron energy loss spectroscopy (EELS),[4] a beam of monochromatic electrons strikes a surface and the inelastically scattered electrons are detected. The losses in energy of the detected electrons are attributed to excitation of the vibrational modes of the molecules on the surface. Most electron spectroscopies have the advantage of very high surface sensitivity, since the electrons which they use as a probe of the surface have a very short mean free path in materials, ranging from 5 to 30 Å.[5] EELS also has the ability to scan a large spectral range, typically from 100 to 3600 cm^{-1} during a one half hour spectrum. One major disadvantage of the technique is its relatively poor resolution. Typical EELS spectrometers have resolutions of 80 to 100 cm^{-1}, while the best

instruments can only with great difficulty attain resolution of ~30 cm^{-1}.[6] Such resolution makes the observation of small frequency shifts and of the linewidths of adsorbed molecules, which vary from <2 to 50 cm^{-1}, very difficult to observe. Another disadvantage of spectroscopies which use electrons as probes is that they cannot be used in environments where the pressure is above 10^{-3} torr because scattering of the electrons from gas molecules becomes too large.

Inelastic tunneling spectroscopy is a technique which has both good resolution and high surface sensitivity, but because the sample must be in the form of a tunnel junction, the interpretation of the results is not always clear.[7] In addition, the sample must be cooled to liquid helium temperature to obtain high resolution.

Photon spectroscopies, such as Raman and infrared spectroscopies, have the advantage that resolutions of 1 to 10 cm^{-1} are easily obtainable. In addition, experiments in high pressure or liquid environments are possible because the mean free path of photons in materials is very long. Since the frequency of vibration of an adsorbed molecule is usually shifted from that of a molecule in the gas phase, the signal from the adsorbate is readily distinguished from that of the gas. Unfortunately, photons are not very surface specific, penetrating hundreds of Angstroms into a solid material, resulting in a very small surface signal compared to that caused by the bulk.

Recently, surface enhanced Raman spectroscopy[8] and nonlinear optical spectroscopies[9] have become very popular methods for studying vibrational spectra at surfaces. These techniques, however, seem to be particularly suited only to certain types of experimental systems.

especially to those with adsorbates on metals with a high imaginary part of the dielectric constant and rough surfaces. The recent reports of non-enhanced Raman spectroscopy on surfaces may make such techniques more generally applicable.[10]

Other optical techniques which have been used to obtain vibrational spectra on surfaces include infrared ellipsometry,[11] surface electromagnetic wave spectroscopy,[12] photoacoustic techniques,[13] and electroreflectance vibrational spectroscopy.[14] All of these techniques are in an advanced stage of development and may soon become applicable to more adsorbate-substrate systems. The development of more powerful tunable infrared sources, such as tunable laser sources, synchrotron sources, and free electron laser sources, in the near future may make other types of optical surface vibrational spectroscopy feasible.

Several methods of doing infrared spectroscopy on surfaces exist. Infrared transmission experiments on supported metal catalysts have been performed for many years.[15] Most infrared experiments on adsorbates on single crystal metal samples have used the reflection-absorption technique.[16] This technique uses an infrared beam which is reflected from the sample and detected. The molecular vibrations absorb energy from the beam and thus cause reductions in intensity of the reflected signal at their vibrational frequencies. Reflection-absorption spectroscopy from metal substrates suffers from the difficulty that the high reflectivity of the metal results in a very high background signal from the bulk.[17] The surface molecular signal is very small compared to this experimental background. Multiple reflections can, of course, be used to increase the surface sensitivity of the technique.[18]

By placing a thermometer onto the sample, one can measure the infrared absorption directly.[19] This technique allows the observation of the same small surface signal on top of the smaller background arising from the absorption of the bulk. Adequate sensitivity with thermal sources, however, can only be obtained at extremely low temperature (~1.5K). In addition, the sample must have low heat capacity in order to be used as a detector. It must also be specially designed and fabricated for this type of experiment. Finally, it is very difficult to clean the sample with the thermometer attached.

Since emissivity is thermodynamically the same as absorptivity, an infrared emission experiment benefits from the same reduction of background as a direct absorption experiment. In addition, conventional single crystal samples at room temperature can easily be used. Because of this background reduction, an infrared emission experiment should also be less influenced by the instability of the source and apparatus than a reflection experiment. The calculations in Chapter II demonstrate that the emission experiment should have particularly good signal to noise ratio in the low frequency range of 300 to 1000 cm^{-1} where many adsorbate-substrate vibrations fall.

The emission experiment is conceptually very simple. In this experiment the sample <u>is</u> the source. The experiment involves the observation of thermal radiation from a sample in thermal equilibrium at room temperature. Thus, the technique does not require that any probing particles strike the surface. Instead, the adsorbate molecules are placed onto the surface, and their thermal emission is detected. The emission from the bulk material will be that of a 300K blackbody times

the emissivity of the substrate. Since the adsorbate molecules have higher emissivity than the substrate, their vibrational lines will appear on top of the broadband emission from the substrate.

Although infrared emission spectroscopy has not been a popular technique, it has been previously used by several groups to observe adsorbates on surfaces. Most spectra measured by this technique have used samples with multilayer films, high sample temperatures, or supported metal catalysts in order to increase the total signal so as to see the small contribution from adsorbates. Spectra of 9 layers of stearate film on a gold substrate have been reported by Blanke et al.[20] Kember et al. report spectra from an oxide layer of 6 nm. thickness on aluminum at 100°C.[21] Infrared emission has also been used by Primet et al. to study the interaction of propene on supported V_2O_5 between 110 and 250°C.[22] They have also studied the adsorption of pyridine and of CO on platinum supported on Zeolite Y at 110°C.[23] The oxidation of molybdenum metal has been studied by infrared emission techniques by Gratton et al.[24]

The technique of infrared emission has also been used by Allara et al. to observe a monolayer quantity of chemisorbed p-nitrobenzoic acid adsorbed on a thin native oxide overlayer on copper at 300K.[25] They used an interferometer operating at 77K to provide low background signals and high sensitivity.

Our goal has been the development of a high resolution spectroscopic technique with sufficient sensitivity to measure the linewidths of weak low frequency adsorbate-substrate vibrations on clean, single crystal samples. In order to exploit the advantages of an

emission experiment for this purpose, we have designed and built an apparatus to measure the infrared emission from a single crystal sample in thermal equilibrium at room temperature. This apparatus consists of a liquid helium temperature grating spectrometer coupled to a conventional ultrahigh vacuum system. The apparatus is capable of measuring the range of infrared frequencies from 330 to 3000 cm^{-1} with an instrumental resolution of 1 to 15 cm^{-1}. This thesis describes the design and construction of this apparatus and the development of the infrared emission technique as a viable tool for the study of the vibrational modes of molecules adsorbed on clean, single crystal metal surfaces.

We have studied the system of CO adsorbed on Ni(100), using this infrared emission technique to measure both the carbon-oxygen stretching vibration at about 2000 cm^{-1} and the carbon-nickel stretching vibration at about 470 cm^{-1}. Our infrared emission apparatus is currently the only surface apparatus capable of studying these lines with sufficient sensitivity and resolution to measure the linewidths of both of these lines on a single crystal surface.

The remainder of the thesis is briefly summarized as follows. In Chapter II, we discuss the feasibility of the infrared emission experiment and the parameters which influenced the design of the apparatus to do this experiment. In Chapter III, we discuss the apparatus in detail. In Chapter IV, we compare the actual system performance with theoretical calculations. The data for carbon monoxide on nickel which we show in Chapter V demonstrate that indeed the infrared emission technique works and produces useful data on the

vibrational modes of adsorbate molecules. Finally, in Chapter VI, we conclude with a summary of our observations and suggestions for further work.

II. FEASIBILITY OF THE EMISSION EXPERIMENT

A. Advantages of the Emission Experiment

For the measurement of the vibrational modes of adsorbed molecules, infrared experiments can be performed in four different ways: transmission, reflection, absorption, and emission. For flat metal substrates, only the last three methods are useful and will be compared in the following discussion. The conventional reflection-absorption experiment, to be called simply reflection in the following discussion, detects radiation from an external source which is reflected from the sample. In the direct absorption experiment, to be called simply absorption, the sample is made into a sensitive infrared bolometric detector. In the emission experiment, on the other hand, the sample is the source of the radiation.

For a metal which is a good conductor and therefore has a high reflectivity, the primary advantage of the infrared emission or absorption experiment is the larger surface signal to background ratio as compared with the reflection experiment. Therefore, the dynamic range requirements on the detector will be less severe by at least one order of magnitude. In addition, the dependence of the total detected signal on the source stability will also be smaller by about the same factor.

We expect the emission and absorption experiments to be particularly suited to metals with low emissivity, such as platinum and silver, because the background rejection will be good. These methods would also be well suited to studying adsorbates on infrared transparent insulators and semiconductors because the background from such

substrates would be small. An apparatus designed to observe emission should also be capable of measuring systems in equilibrium at high temperatures and pressures, as well as being able to observe exothermic chemical reactions.

Conversely, the emission technique would not be well suited to systems with strongly absorbing substrates which would cause a large background signal. The technique also should not be used for studying cold samples at temperatures less than ~200K, since the total signal from the sample is due to its thermal emission and decreases as the sample is cooled. Depending on the sample temperature to be investigated, either a reflection experiment or an absorption experiment is better suited to studying a cold sample. The direct absorption technique is very useful for the study of low temperature samples, since the measurements are all performed at 1.5K.

An emission experiment is expected to be possible in some cases where a reflection experiment is not. If the sample is not flat or highly reflective, a reflection experiment might not be possible because not enough signal could be collected. In addition, an emission experiment might be better suited to observing a high temperature chemical reaction in situ, which would have a high flux of photons from the source.

The greatest advantage of the emission experiment over the absorption experiment is that samples do not have to be specially fabricated just for this technique. Instead, the apparatus can be equipped with conventional surface cleaning and characterization tools, such as LEED and Auger spectroscopy. The infrared emission technique

can then be used as an auxiliary surface tool to study the nature of the chemical bonds on the surface.

Some of these arguments will be made more quantitative in the following sections in which we will calculate the expected sensitivity of the emission experiment and compare it to that of the reflection and absorption experiments.

B. Polarization of the Surface Radiation

In the measurement of the infrared surface signal on a metal, the boundary conditions on the electric field at the surface are extremely important in determining the polarization of the radiation and the optimum angles for observation. Inside an ideal conductor, the electric field is of course zero. Since the boundary conditions at the surface require that the component of the electric field parallel to the surface be continuous, that component is also zero just outside the metal.[26] Thus, only a component of electric field perpendicular to the surface can exist just outside the conductor, and only this component can interact with adsorbed molecules on the surface. Therefore, in order to obtain the maximum infrared emission signal from the surface, the perpendicular component of the electric field should be as large as possible. Since the electric field vector is always perpendicular to the direction of propagation of the light, this condition is obtained by observing the light at near grazing angles. The radiation from the surface will thus be polarized with its electric field vector perpendicular to the metal surface, which is, in other terminology, the electric field component parallel to the plane of incidence of the light (p-polarized).

C. Dependences of the Surface Signal

Several workers have calculated the absorption of a dielectric layer on a metal substrate.[17,27-29] Bailey has calculated the expected absorption for a surface layer of carbon monoxide on a nickel film.[30] He uses a dipole model for the adsorbed CO molecules to estimate the dielectric constant of the layer and uses the measured dielectric constant of nickel at room temperature from Beattie[31] to estimate the dielectric constant for the cold nickel sample in the direct absorption experiment. The results from Bailey's calculations are shown in Figures 1 and 2 and will be described below.

The absorption by the cold bulk nickel as a function of the angle of incidence is shown in Figure 1a. It is clear that there is very little absorption of the polarization perpendicular to the plane of incidence (s-polarization), as expected from the discussion in the previous section. The radiation polarized parallel to the plane of incidence (p-polarized), on the other hand, is able to interact strongly with the surface layer.

Bailey has also calculated the ratio of the signal expected from 0.1 monolayer of CO to that of a cold nickel substrate. In Figure 1b, this fractional surface signal is shown as a function of the angle of incidence for both the absorption experiment and the reflection experiment at a frequency of 2000 cm^{-1} with a resolution of 6 cm^{-1}. The total absorbed power by the metal will be the same as the emitted power in an emission experiment, so these results apply directly to the experiments described in this thesis. For the emission or absorption experiment, the maximum fractional surface signal is about twice that

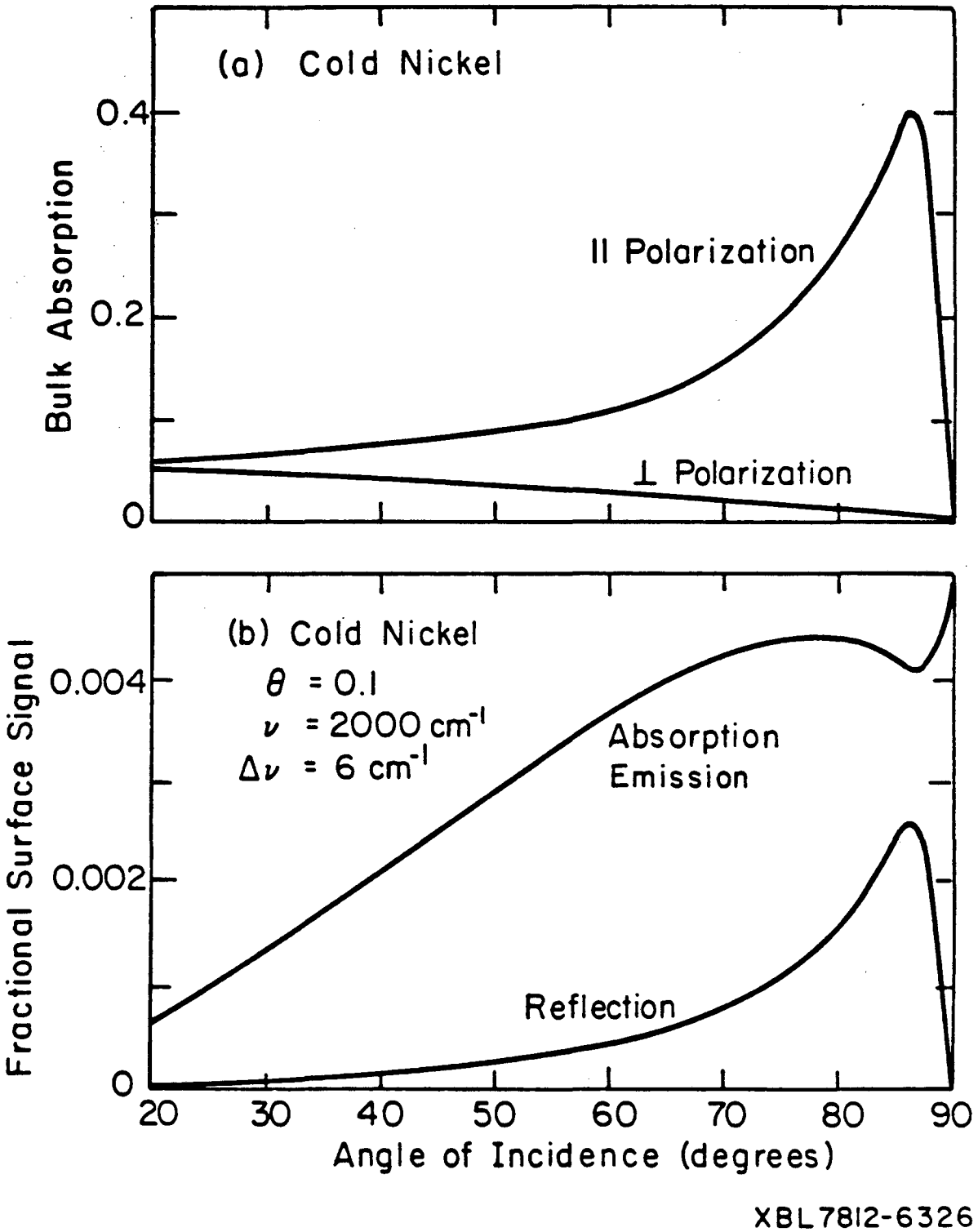

Fig. 1. Bulk and surface signal versus angle of incidence. From Ref. 30.

for the reflection experiment. The range of angles for which the surface signal is high is also greater for the emission or absorption technique. As expected, the maximum fractional surface signal should be obtained near grazing incidence.

Figure 2a shows the results of Bailey's calculation of the bulk absorption of both warm and cold nickel and copper surfaces as a function of the infrared frequency for an angle of incidence of 80^{o}. The expected emission from the bulk in thermal equilibrium is of course the same as the bulk absorption. We see that the absorption and emission experiments will have a larger advantage over the reflection experiment for frequencies less than 2000 cm^{-1} where the interband absorption by the bulk nickel is smaller. Also, for frequencies less than 2000 cm^{-1}, as a result of the temperature dependent phonon scattering, the bulk emission from a warm nickel sample is expected to be about a factor of two higher than the bulk absorption from the cold substrate in the absorption experiment.

Finally, for a molecule identical to carbon monoxide except for the frequency of its resonance, Bailey calculated the fractional surface signal as a function of infrared frequency. Figure 2b shows his curves for reflection by a cold nickel substrate, absorption by a cold substrate, and absorption (or emission) by a warm substrate. We can see that the difference between dielectric properties of warm and cold nickel cause the absorption experiment to have the largest fractional surface signal, followed by the emission experiment with a warm substrate, followed by the reflection experiment from a cold substrate. For frequencies less than 1000 cm^{-1}, the emission experiment should have

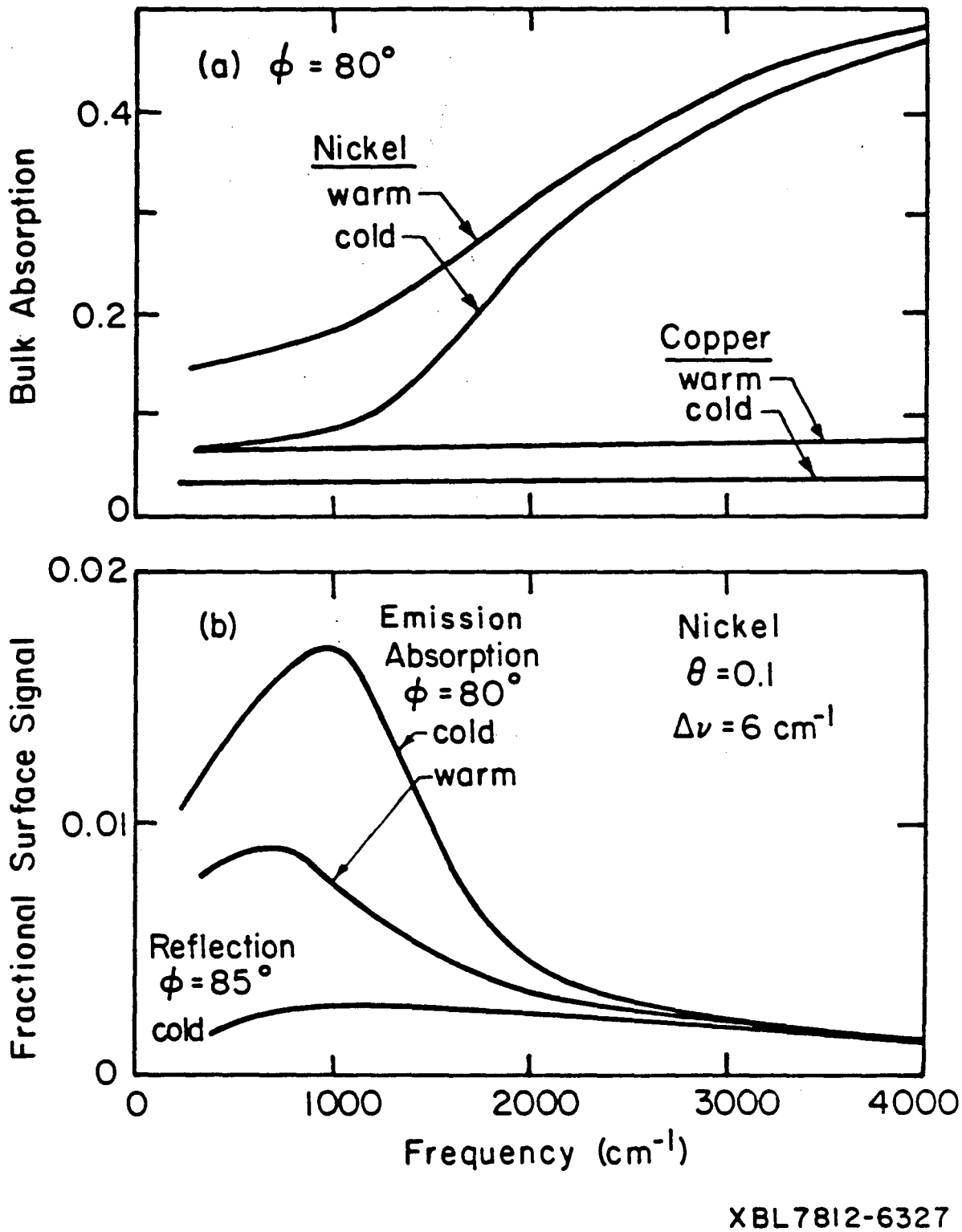

Fig. 2. Bulk and surface signal versus infrared frequency. From Ref. 30.

a fractional surface signal which is a factor of 3 to 4 higher than that of the reflection experiment.

D. Calculations Demonstrating the Feasibility of the Emission Experiment

In order to decide whether we would be able to see the room temperature emission signal from adsorbed molecules on a metal surface, calculations were performed to estimate the signal and noise for such a measurement. These values were then compared with performance specifications for state-of-the-art photoconductive detectors to decide whether the experiment would be feasible. Estimates of the necessary temperatures of various components in the system were also made. A room temperature sample is desirable because it is convenient to use and because many practical chemical reactions take place near room temperature. In addition, the calculations show that a room temperature sample gives a significant emission signal in the useful spectral range from 400 to 3000 cm^{-1} which comprises the chemical "fingerprint" region of the infrared spectrum.

For a room temperature blackbody source, we can easily calculate from statistical mechanics the number of photons per second which can be measured by the detector in our spectrometer.[32] Blackbody radiation is electromagnetic radiation in equilibrium inside an enclosure of volume V at temperature T. The Planck distribution gives $\bar{n}_i$, the average number of photons in the i-th energy state, which has energy $h\nu$.

$$\bar{n}_i = \frac{1}{e^{h\nu/kT} - 1} \qquad (1)$$

M, the number of modes per unit volume in a small frequency interval of width $d\nu$ for each polarization, is

$$M = \frac{4\pi \nu^2 \, d\nu}{c^3} . \tag{2}$$

With a factor of 2 for the two polarizations of blackbody radiation, we obtain $\bar{n}_\nu$, the mean number of photons per unit volume as

$$\bar{n}_\nu = 2M\bar{n} = \frac{8\pi \nu^2 \, d\nu}{c^3} \; \frac{1}{e^{h\nu/kT} - 1} . \tag{3}$$

Since blackbody photons move isotropically, the number of photons per volume moving in the direction of an infinitesimal solid angle $d\Omega$ is $\bar{n}_\nu d\Omega/4\pi$. We want to know the number of photons incident upon a detector area A. For angle of incidence θ of the photons on area A, all photons in a volume c dt A cosθ will strike an area A in time dt, where the speed of light is c. Therefore, integrating over the solid angle of acceptance of the spectrometer, the number of photons which will cross area A in unit time is

$$N = \bar{n}_\nu \int \frac{d\Omega}{4\pi} cA \cos\theta . \tag{4}$$

This formula gives the number of photons per second from a blackbody source which would be incident upon a detector in an ideal spectrometer with 100% efficiency.

In the emission experiment described here, a low emissivity metal is used as a substrate. Therefore, for a real spectrometer with efficiency E and substrate emissivity ε, the number of photons per second incident upon the detector will be

$$N = \bar{n}_\nu \int \frac{d\Omega}{4\pi} cA \cos\theta \, \epsilon E \tag{5}$$

$$= \frac{8\pi \nu^2 \, d\nu}{c^3} \frac{1}{e^{h\nu/kT} - 1} cA\epsilon E \int \frac{d\Omega}{4\pi} \cos\theta \, .$$

If α is the half angle of acceptance of the spectrometer, the solid angle integral is simply

$$\int \frac{d\Omega}{4\pi} \cos\theta = \frac{1}{4\pi} \int_0^\alpha \cos\theta \sin\theta \, d\theta \int_0^{2\pi} d\phi = \frac{\sin^2\alpha}{4} \, . \tag{6}$$

If we let $\bar{\nu} = \nu/c$, we obtain the form

$$N = 2\pi \bar{\nu}^3 \frac{d\bar{\nu}}{\bar{\nu}} \frac{1}{e^{hc\bar{\nu}/kT} - 1} cA\epsilon E \sin^2\alpha \, . \tag{7}$$

By multiplying N by $hc\bar{\nu}$, the energy per photon, we can compute the power P which will be incident upon the detector.

$$P = hc\bar{\nu} N \tag{8}$$

We can also calculate the mean square fluctuation in the number of photons per second incident upon the detector. For photons, the mean square fluctuation in the number per state is[33]

$$\overline{(\Delta n_s)^2} = \bar{n}_s (1 + \bar{n}_s) \tag{9}$$

$$= \bar{n}_s \frac{1}{1 - e^{-hc\bar{\nu}/kT}} \, .$$

Following the same arguments on the solid angle and volume of photons incident on the detector as above, we obtain for the mean square fluctuation in the number of photons per second on the detector,

$$\overline{(\Delta N)^2} = 2\pi \bar{\nu}^{-3} \frac{d\bar{\nu}}{\bar{\nu}} \frac{\bar{n}_s}{1 - e^{-hc\bar{\nu}/kT}} cA\varepsilon E \sin^2\alpha \qquad (10)$$

$$= \frac{N}{1 - e^{-hc\bar{\nu}/kT}} .$$

To find the noise fluctuations within a bandwidth Δf near frequency f of the amplifier, we must put in a factor $2\Delta f$.[34] We obtain the following equation for the ratio of photon noise to signal:

$$\frac{\Delta N(f)}{N} = \frac{\sqrt{\overline{(\Delta N(f))^2}}}{N} = \sqrt{\frac{2\,\Delta f}{N(1 - e^{-hc\bar{\nu}/kT})}} \qquad (11)$$

$$= \frac{\Delta P}{P}$$

Finally, we can obtain the fluctuation in the power incident on the detector due to the photon noise.

$$\Delta P = \left(\frac{\Delta P}{P}\right) P \qquad (12)$$

Using Eqs. (7), (8), (11), and (12), we can compute N, P, $\Delta N/N$, and ΔP as a function of ν for several different temperatures T. In these computations, we will now use the parameters for the grating instrument which we actually built.

The resolving power of the instrument is $\lambda/d\lambda$. This can be obtained from the grating equation as follows.[35]

$$n\lambda = 2d \sin\theta \cos\phi \qquad (13)$$

Here λ is the wavelength of the light, n is the order of diffraction, d is the groove spacing of the grating, ϕ is one half of the fixed angle between the incident and diffracted beams at the grating, and θ is the angle of the grating which changes as we measure a spectrum.

Differentiating this equation with respect to θ,

$$nd\lambda = 2d \cos\theta \cos\phi \, d\theta \, . \tag{14}$$

Dividing Eq. (14) by Eq. (13), we obtain

$$\frac{d\lambda}{\lambda} = \frac{d\nu}{\nu} = \frac{d\theta}{\tan\theta} \, . \tag{15}$$

Assume that the entrance slit is the same size as the width of the detector, which is 1 mm. We can estimate the angular resolution of the instrument from the width of the detector, dx, and the focal length, f, of the mirror which focuses the radiation on the detector.

$$d\theta = dx \, / \, f \tag{16}$$

Since f = 183 mm, $d\theta = 0.31^{o}$. For the purposes of these calculations, we will assume the value of θ at the blaze angle of one of our diffraction gratings, which is 36.87^{o}, so that $\tan\theta = 0.75$. Then we have $d\nu/\nu = 7.21 \times 10^{-3}$.

The throughput of the system is limited at the detector. The area of the detector is 2 mm^2 and the half angle of acceptance of the radiation in the spectrometer is 11.5^{o}. Thus we obtain

$$A\Omega/4\pi = A \, \frac{\sin^2\alpha}{4} \tag{17}$$

$$= 2 \times 10^{-4} \ cm^2 .$$

We will use $\varepsilon = 0.25$, which is the calculated emissivity of nickel at 2000 cm^{-1} at an angle of incidence of 85^{o}, and ignore its dependence on frequency ν. Finally let us assume that the efficiency of the instrument, E, is equal to 0.10.

Inserting all of these values, we obtain the expected values of N, P, $\Delta N/N$, and ΔP which are given in Table I. A plot of N versus

TABLE I

Results of Blackbody Calculations

(cm^{-1})	N (photons/sec)	P (watts)	N/N	P (watts/$Hz^{1/2}$)
T = 77K				
100	5.52×10^{9}	1.09×10^{-11}	2.08×10^{-5}	2.29×10^{-16}
500	4.65×10^{8}	4.63×10^{-12}	6.55×10^{-5}	3.03×10^{-16}
1000	5.09×10^{5}	1.01×10^{-14}	1.98×10^{-3}	2.00×10^{-17}
1500	2.35×10^{2}	7.03×10^{-18}	9.21×10^{-2}	6.47×10^{-19}
T = 300K				
100	4.69×10^{10}	9.34×10^{-11}	1.07×10^{-5}	1.00×10^{-15}
500	3.85×10^{11}	3.83×10^{-9}	2.40×10^{-6}	9.22×10^{-15}
1000	2.85×10^{11}	5.68×10^{-9}	2.65×10^{-6}	1.51×10^{-14}
1500	9.73×10^{10}	2.90×10^{-9}	4.53×10^{-6}	1.31×10^{-14}
2000	2.35×10^{10}	9.35×10^{-10}	9.22×10^{-6}	8.62×10^{-15}
2500	4.67×10^{9}	2.32×10^{-10}	2.06×10^{-5}	4.81×10^{-15}
3000	8.24×10^{8}	4.91×10^{-11}	4.92×10^{-5}	2.42×10^{-15}
3500	1.33×10^{8}	9.28×10^{-12}	1.22×10^{-4}	1.13×10^{-15}
4000	2.03×10^{7}	1.61×10^{-12}	3.13×10^{-4}	5.07×10^{-16}
T = 400K				
100	6.65×10^{10}	1.32×10^{-10}	1.01×10^{-5}	1.34×10^{-15}
500	7.48×10^{11}	7.44×10^{-9}	1.80×10^{-6}	1.34×10^{-14}
1000	9.15×10^{11}	1.82×10^{-8}	1.50×10^{-6}	2.73×10^{-14}
1500	5.42×10^{11}	1.61×10^{-8}	1.92×10^{-6}	3.11×10^{-14}
2000	2.30×10^{11}	9.18×10^{-9}	2.94×10^{-6}	2.70×10^{-14}
2500	8.12×10^{10}	4.04×10^{-9}	4.96×10^{-6}	2.00×10^{-14}
3000	2.53×10^{10}	1.51×10^{-9}	8.88×10^{-6}	1.34×10^{-14}
3500	7.25×10^{9}	5.05×10^{-10}	1.66×10^{-5}	8.38×10^{-15}
4000	1.95×10^{9}	1.55×10^{-10}	3.19×10^{-5}	4.97×10^{-15}

frequency for T=77K, 300K, and 400K is shown in Figure 3. We can draw a number of conclusions from this plot. First, the room temperature sample emits a significant amount of radiation for frequencies between 100 and 3000 cm^{-1}, a range which include most intramolecular and molecule-substrate vibrations. Clearly, the blackbody curve is falling off exponentially at 2000 cm^{-1}, which is the frequency of the C=O stretching vibration on a surface. But at lower frequencies between 300 and 1200 cm^{-1}, the source has much more intensity. Therefore, if the dominant noise source is the photon noise, the signal to noise ratio will be larger at those frequencies. We also see that the radiation from liquid nitrogen temperature objects is negligible for frequencies above 200 cm^{-1}. Finally, raising the temperature of the sample to 400K only increases the signal by about a factor of 2 or 3 in the range from 300 to 1000 cm^{-1}.

The noise equivalent power (NEP) of a photoconductive detector is the amount of incident power which can be measured with a signal to noise ratio of one in a one hertz bandwidth. For the best photoconductive detectors, the NEP is about 10^{-16} watts/$Hz^{1/2}$.[36] We can compare this value of the detector NEP with the fluctuations in the power from photon noise, given in the table. We see that the detector noise should be negligible for frequencies below 4000 cm^{-1}. If other sources of noise can be made smaller than the photon noise, an emission experiment should have excellent signal to noise ratio for those frequencies. For the photon noise limited experiment, we note from the table that the signal to noise ratio is greater than 10^4 for all frequencies below 3000 cm^{-1}, which we expect to be sufficient to see a wide variety of adsorbed

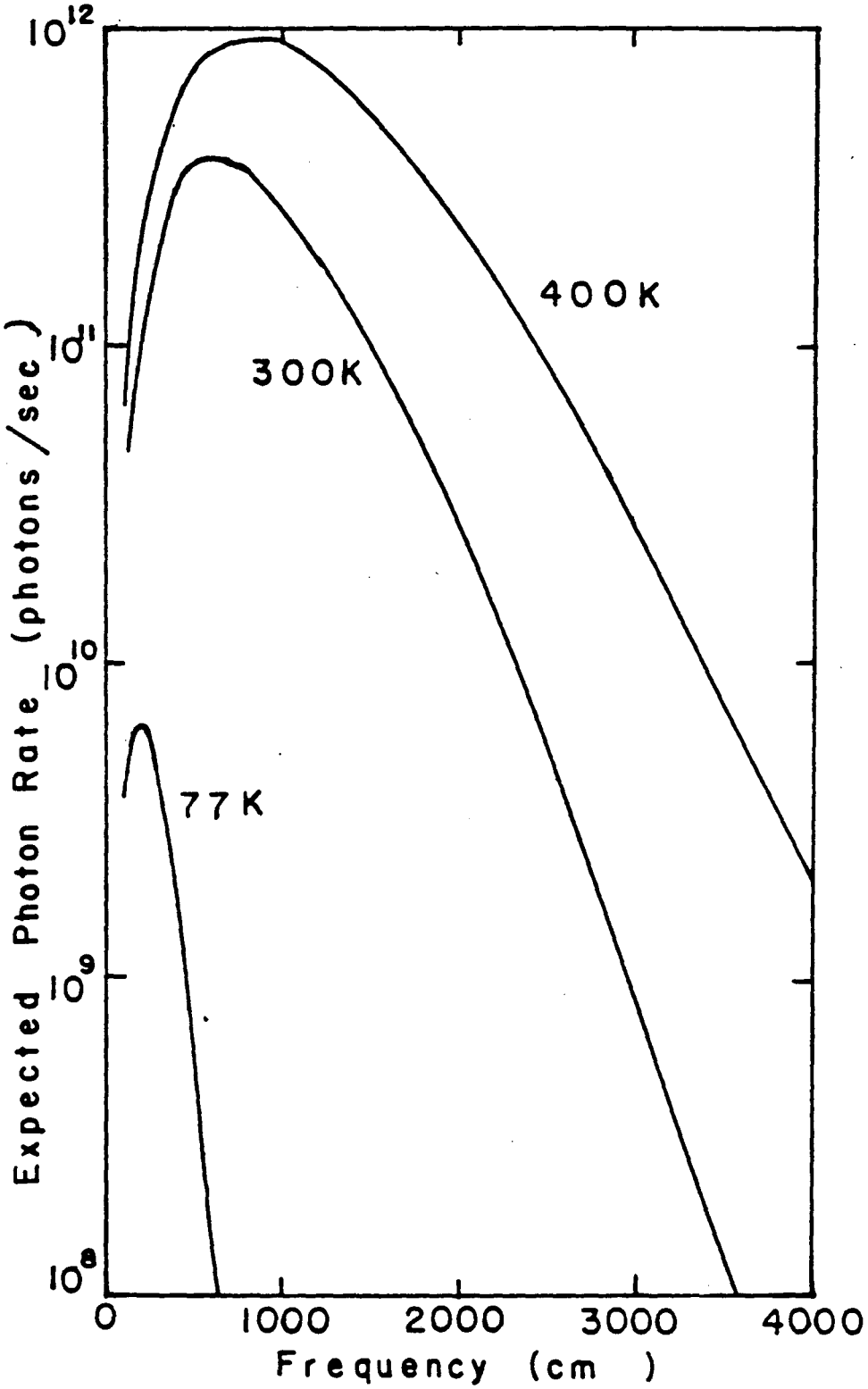

Fig. 3. Expected photon rate at our detector as a function of frequency for source temperatures of 77K, 300K, and 400K.

species. In Chapter IV, we shall discuss in more detail the ability of a photon noise limited emission apparatus to detect small surface signals.

These calculations indicated to us that it would be possible to build a photon noise limited apparatus to measure infrared emission spectra from adsorbed monolayers using state-of-the-art infrared photoconductive detectors.

E. Comparison of Reflection, Absorption and Emission Experiments

We can also use the same blackbody formulas given in the previous section to calculate the surface signal to noise ratio for the reflection, absorption, and emission experiments. We assume the same spectrometer throughput and resolution parameters which were given above for all three types of experiments. For the molecular signal, we assume an emissivity of 0.01. Of course, for a real molecular layer with an emissivity e, the results of the calculations can be scaled by e/0.01 to obtain the expected surface signal to noise ratio. For the substrate emissivity, we assume $\varepsilon = 0.25$, which is the emissivity of nickel at 2000 cm^{-1} at an observation angle of 85^{o} to the surface normal. The reflectivity is then assumed to be $(1-\varepsilon) = 0.75$. We assume that all three types of experiments are background photon noise limited. Note, however, that this is an extremely optimistic assumption; if the photon noise is very small, it is unlikely to be the dominant source of noise in the experiment.

The differences among the three types of experiments are the source temperature and the noise on the substrate background signal. For the emission experiment, we assume a source temperature of 300K. The

surface signal from the molecules will then be given by a 300K blackbody curve with emissivity equal to 0.01. We assume the noise is caused by photon noise on the substrate signal, which we can calculate from our blackbody formulas with emissivity $\varepsilon = 0.25$.

For the reflection experiment, we assume a source temperature of 1300K. The surface signal from the molecules will then be given by a 1300K blackbody curve with emissivity equal to 0.01. The noise, however, will be the photon noise on the large reflected signal, which we calculate from a 1300K blackbody curve with $\varepsilon = 0.75$.

Finally, for the absorption experiment, we also assume that light is incident from a 1300K source. The molecular surface signal is then given by the same formula as in the reflection experiment. The noise, however, will be the photon noise on the smaller signal absorbed by the substrate, which we calculate from a 1300K blackbody curve with $\varepsilon = 0.25$.

For the three types of experiments, we obtain the surface signal to photon noise ratios as a function of frequency, which we show in Figure 4. We see that the reflection experiment is expected to have a larger surface signal to noise ratio than the emission experiment for frequencies above 350 cm^{-1}. The absorption experiment has a larger surface signal to noise ratio than the emission experment throughtout the range from 100 to 10000 cm^{-1}. The primary reason that the curves for the reflection and absorption experiments are larger than that for the emission experiment is the higher source temperature for the former two, resulting in a larger ratio of the signal to the photon noise. We expect, however, that it would be more difficult for the reflection and

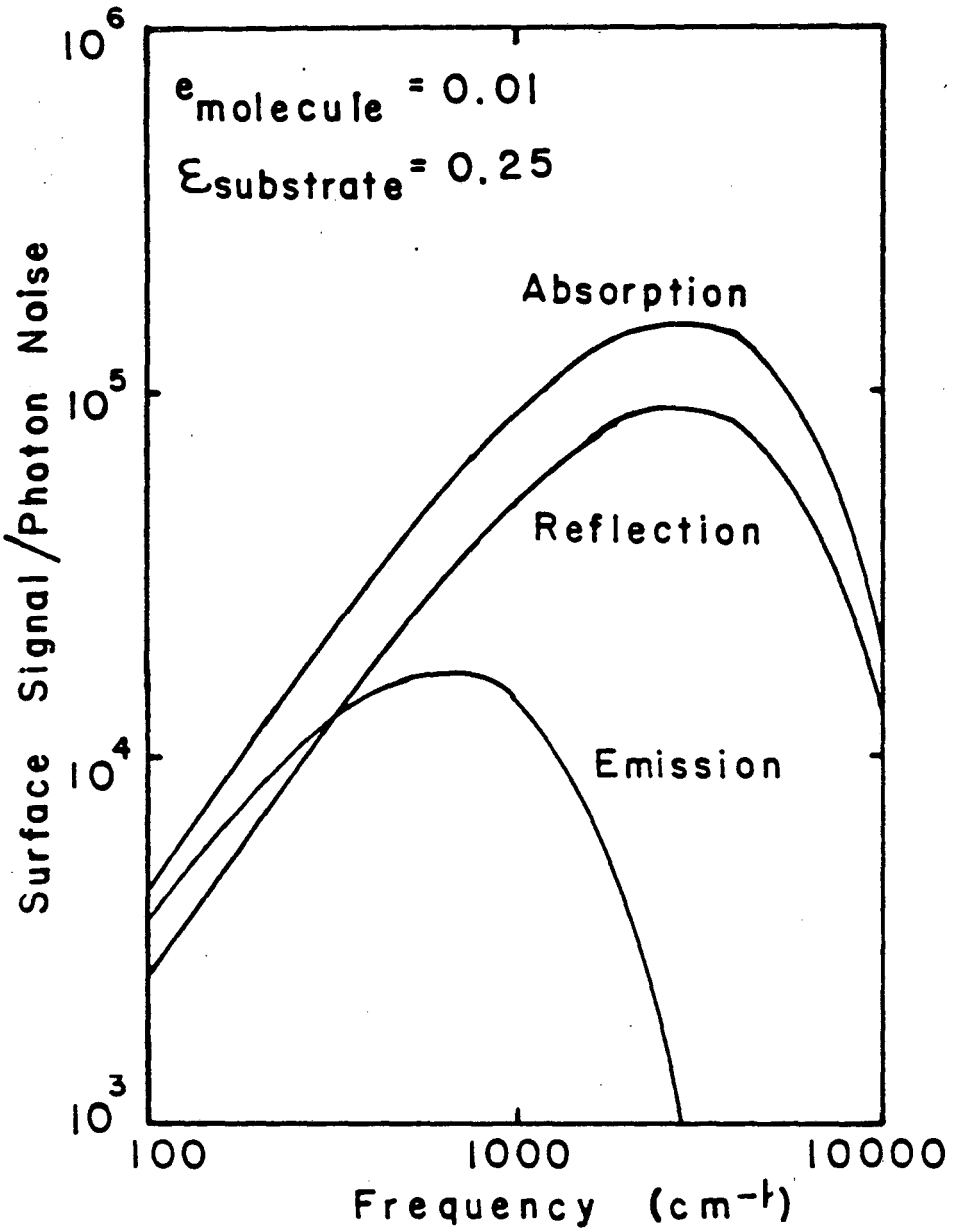

Fig. 4. Ratio of surface signal to photon noise as a function of frequency for absorption, reflection, and emission experiments, with molecular emissivity of 0.01 and substrate emissivity of 0.25.

absorption experiments to operate in the photon noise limit because they would be more sensitive to problems with the source stability and the limited dynamic range of the detector. The emission experiment should be about an order of magnitude less sensitive to these effects.

F. Design of the Apparatus

To observe the room temperature emission from a sample in thermal equilibrium, it is necessary to cool the environment around the sample to reduce the stray background signal. We decided to cool our entire spectrometer with liquid helium (4.2K) for two reasons: (1) The emission from the optical elements inside the spectrometer is then completely negligible, even at very low optical frequencies, down to less than 20 cm^{-1}. Once the light enters the entrance slit of the spectrometer, no further background radiation from any of the elements inside the spectrometer can make any contribution to the signal at the detector. (2) The doped silicon photoconductive detectors which we planned to use need to be cooled to less than 20K in order to operate. Such low temperatures freeze all of the carriers in the detector down to their lowest energy levels. Incoming infrared photons excite carriers across the small energy gap, thus causing a large change in the conductivity of the detector.

Having made the decision to build a liquid helium cooled spectrometer, the next question was what type to build: a grating spectrometer or a Fourier transform infrared spectrometer (FTIR). The decision as to which type of spectrometer is best depends on the conditions under which it will be used. In particular, if the system is limited by detector noise, the Fourier transform instrument has the well

known multiplex advantage.[37] If this is not the dominant noise source in the system, the signal to noise ratio (S/N) of the grating instrument may be the same or better than that of the FTIR, as summarized in Table II. By extending the discussion in Ref. 37, we will now derive the results shown in the table.

Different types of noise sources have different dependences on the signal power. Let us consider three possible dependences of the noise on the signal power, which will characterize the noise for the purposes of this discussion. Since detector noise is independent of the signal power, $\Delta P \propto P^0$. For photon noise, $\Delta P \propto P^{1/2}$. Finally, for source fluctuations, microphonic noise, or other such instabilities in the signal, $\Delta P \propto P$. We want to compute the S/N ratio in a small band, $\Delta\nu$, for both types of instruments for these three cases.

First, consider the case $\Delta P \propto P^0$, where the noise is independent of the signal and depends only on the measuring time. Let T=total time spent measuring a spectrum containing M spectral elements. Then for the grating instrument, in a small bandwidth, $\Delta\nu$, the signal will be proportional to the amount of time spent measuring in that band.

$$S_G \sim T/M \tag{18}$$

The noise will just be proportional to the square root of the time spent measuring that band.

$$N_G \sim (T/M)^{1/2} \tag{19}$$

Thus, for the grating instrument,

$$(S/N)_G \sim (T/M)^{1/2} \tag{20}$$

For the FTIR, on the other hand, the signal is proportional to the total time for measuring the whole spectrum, since the interferometer measures

TABLE II

Comparison of Grating Spectrometer with Fourier Transform Spectrometer

Dependence of Noise on Signal Power	Type of Noise	Comparison of S/N Ratio
$\Delta P \propto P^0$	Detector	FT Multiplex Advantage
$\Delta P \propto P^{1/2}$	Photon	Same for Grating and FT
$\Delta P \propto P$	Source fluctuations.	Grating Advantage

all frequencies at one time. Thus, the signal in a small bandwidth, $\Delta\nu$, is

$$S_I \sim T. \tag{21}$$

The noise is $N_I \sim T^{1/2}$, (22)

so that $(S/N)_I \sim T^{1/2}$ (23)

Thus, the FTIR has a signal to noise ratio larger than the grating instrument by a factor $M^{1/2}$.

Now consider the case $\Delta P \propto P^{1/2}$. Let $I(\Delta\nu)$ be the power in a small band, assumed independent of frequency ν.

Then, the grating spectrometer will have

$$S_G \sim \frac{T}{M} I(\Delta\nu) \tag{24}$$

The noise will be proportional to the square root of the signal.

$$N_G \sim \sqrt{\frac{T}{M} I(\Delta\nu)} \tag{25}$$

and thus $(S/N)_G \sim \sqrt{\frac{T}{M} I(\Delta\nu)}$ (26)

But for the FTIR, the signal in a small band, $\Delta\nu$, is

$$S_I \sim T\, I(\Delta\nu) \tag{27}$$

The noise, on the other hand, will be proportional to the square root of the <u>entire</u> signal on the detector, which comes from all M spectral elements at once. Thus,

$$N_I \sim \sqrt{TMI(\Delta\nu)}. \tag{28}$$

So in a small band, $\Delta\nu$, the signal to noise ratio is

$$(S/N)_I \sim \sqrt{\frac{T}{M} I(\Delta\nu)} \tag{29}$$

Both instruments will thus have the <u>same</u> signal to noise ratio in this case.

Finally, consider the case where $\Delta P \propto P$. Then the grating instrument will again have the signal

$$S_G \sim \frac{T}{M} I(\Delta\nu) \tag{30}$$

Since the noise is proportional to the signal,

$$N_G \sim \frac{T}{M} I(\Delta\nu) \tag{31}$$

so that $$(S/N)_G \sim 1. \tag{32}$$

The FTIR, on the other hand will have

$$S_I \sim T\, I(\Delta\nu) \tag{33}$$

and $$N_I \sim TMI(\Delta\nu) \tag{34}$$

so that $$(S/N)_I \sim 1/M \tag{35}.$$

Thus the FTIR will in this case have a signal to noise ratio smaller than that of the grating instrument by a factor of M.

The choice of the best type of instrument for the largest ratio of signal to noise therefore depends on what the dominant noise source in the system is expected to be. If the operation is expected to be limited by detector noise, clearly the multiplex advantage of FTIR makes it the better choice. On the other hand, if the detector has low enough noise that the dominant noise source is expected to be photon noise, both types of instruments are equivalent in S/N ratio. Finally, if the dominant noise source is expected to be from source fluctuations, the grating instrument is actually better.

Since we knew that photoconductive detectors with photon noise limited performance were available, we intended our instrument to work in this limit. Thus we chose to build a grating instrument, because it is much easier to cool than a Fourier transform instrument. In

addition, the development of infrared detector arrays of either the charge coupled device (CCD) or charge injected device (CID) would permit the grating instrument to be used as an infrared multichannel analyzer, with each channel seeing only the noise on its own signal. In fact, since our instrument is currently limited by some dc instability rather than detector noise, the grating instrument was probably the correct choice even if the photon noise limit is not attained.

III. DESCRIPTION OF APPARATUS

In order to measure the infrared emission spectrum from adsorbed molecules on a clean, single crystal metal surface at room temperature, we have designed and built an apparatus which consists of a liquid helium temperature grating spectrometer coupled to a conventional ultrahigh vacuum system. A horizontal cross-section through the apparatus is shown in Figure 5.

To observe infrared emission from a room temperature sample, we would like to put the sample into a cold environment so that the sample is the only source of warm radiation in the field of view of the detector. The environment of the sample should be cold enough that it does not contribute anything to the infrared signal. In practice, we approximate this situation by surrounding the sample with baffles at liquid nitrogen temperature (77K) and cooling our entire infrared spectrometer to liquid helium temperature (~5K). Inside the spectrometer is a very sensitive Si:Sb photoconductive detector. Even in the low flux levels provided by the cold spectrometer, the intrinsic noise of the detector is so low that the detector is capable of photon noise limited performance. This means that its performance is limited by the noise caused by the statistical fluctuations in the incoming photon field.

The sample is placed on a manipulator in a conventional ultrahigh vacuum (UHV) system so that it can be readily cleaned and characterized by several standard surface techniques. The sample is observed at near grazing angles for maximum surface sensitivity and surrounded by 77K baffles. The thermal radiation then passes through an infrared lens,

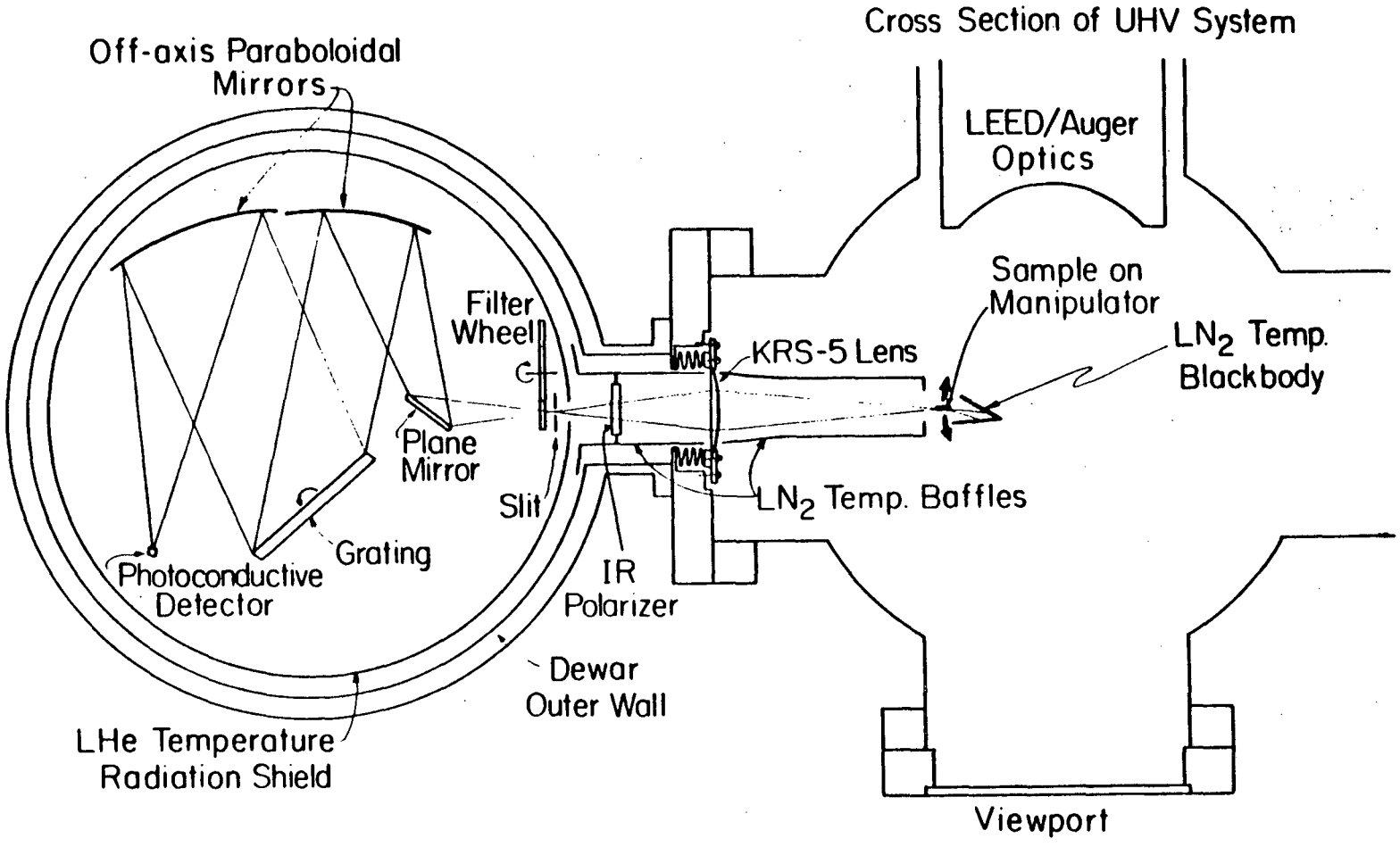

Fig. 5. Optical layout of infrared emission apparatus, with liquid helium cooled spectrometer on the left and ultrahigh vacuum system on the right.

which also serves as a vacuum window between the UHV system and the cold spectrometer. After passing through a cold infrared polarizer, the radiation enters the slit of the grating spectrometer at 5K. The radiation then passes through a long wavelength pass filter to eliminate second and higher orders of diffraction, reflects from a plane mirror and an off-axis paraboloidal mirror, diffracts from the grating as a parallel beam, and is then focused by another off-axis paraboloidal mirror onto the photoconductive detector.

In the following sections, we will discuss the individual elements of the apparatus in detail. In Section A, we discuss the cooled grating spectrometer. In Section B, we discuss the ultrahigh vacuum system and the optics there. In Section C, we discuss the methods of aligning the optics in the system. Finally, in Section D, we discuss the data acquisition system.

A. Cooled Grating Spectrometer

The infrared spectrometer is a grating instrument of the Czerny-Turner type[38] which is housed in a modified commercial cryostat and cooled by liquid helium (4.2K).

1. Cryostat

An Infrared Laboratories model HD-3 liquid helium dewar was heavily modified in order to contain a larger volume at liquid helium temperature to hold the spectrometer optics. A vertical cross section of the dewar is shown in Fig. 6. The liquid nitrogen (LN_2) can is located in the top part of the dewar, with the liquid helium (LHe) can below. The cryostat has a single vacuum space to thermally insulate both the LN_2 temperature objects at 77K and the LHe temperature objects at 4.2K. O-rings are used to seal the vacuum space where disassembly of the cryostat is possible. The original commercial cryostat was modified by welding an aluminum plate, 1/2 in. thick, 13 3/4 in. outer diameter (O.D.), and 6 1/4 in. inner diameter (I.D.) to the outside wall of the cryostat. The new cryostat bottom was then made from a 13 3/4 in. O.D., 1/2 in. wall aluminum tube, welded to a 3/8 in. thick plate. The bottom part is sealed to the top with a large O-ring, which has a diameter of 13 in. Two flanges have been welded into the side wall of the large cylinder; one is a high throughput pumping port, and the other is the optical port. The flange of the optical port can be screwed directly to the outside of an 8 in. O.D. flange on the UHV system.

The optical components of the spectrometer are screwed to a twelve in. diameter aluminum plate which is in turn screwed down to the copper bottom of the liquid helium can. The optical components are surrounded

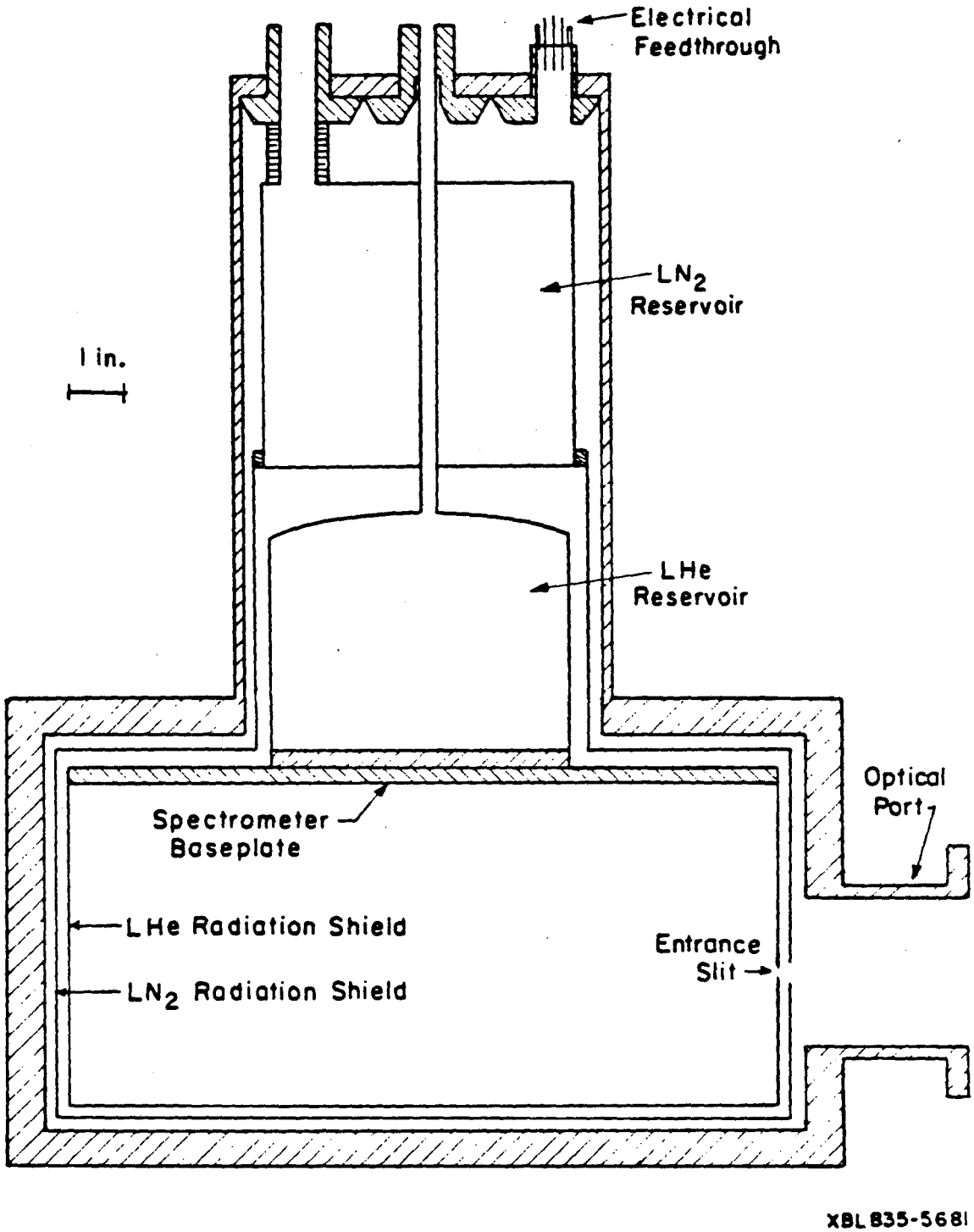

Fig. 6. Vertical cross section of liquid helium cryostat.

by a radiation shield at liquid helium temperature, which is in turn surrounded by a liquid nitrogen temperature radiation shield. These radiation shields are both made of 1/32 in. thick aluminum sheet. Inside the LHe temperature shield, all parts except for the optical elements themselves are painted with 3M Velvet Black paint to reduce stray reflections. The outside of the LHe shield, both the inside and outside of the LN_2 shield, and the inside wall of the cryostat are all covered with aluminum foil, held down with double-sided tape, in order to reduce radiation loss. The radiation shields have no optical holes except for small openings for light to enter the entrance slit of the spectrometer.

The cryostat is equipped with several electrical feedthroughs. Three hermetically sealed Bendix 6-pin electrical connectors are soldered to brass pieces which are then sealed by O-rings under the top plate of the dewar. One of these is usually used for the connections for the detector circuitry, while the other two are normally used for four carbon resistance thermometer connections, leaving eight free leads going down into the dewar. Inside the dewar, the electrical leads are formvar-insulated manganin wires, 0.005 in. diameter, which are heat sunk by gluing them, with General Electric 7031 varnish, over thin strips of paper to the outside of the liquid nitrogen shield. Since the varnish can soften the formvar insulation on the wires, the paper provides additional electrical insulation from ground. To facilitate disassembly of the cryostat at several critical junctions, the wires are soldered to small connectors, made from single-in-line electrical sockets. After going through a small hole in the LHe radiation shield,

the wires are soldered to a small heatsink consisting of a fiberglass printed circuit board epoxied with Stycast 2850FT (Emerson and Cuming, Inc., Canton, MA) to a piece of aluminum which is screwed to the baseplate.[39] The leads at LHe temperature are #22 Teflon-insulated copper wires.

The cryostat also has several mechanical feedthroughs. Since the grating drive must always be connected between room temperature and LHe temperature, the shaft which connects the elements at these two temperatures is made from a thin-walled fiberglass tube, 1/4 in. O.D. and 4 1/2 in. long, which has very low thermal conduction at low temperatures, as well as high torsional strength. (See Fig. 7 for a drawing of the grating drive, which will be discussed in more detail in Section 3.) The tube has a brass coupling screwed to each end and also epoxied to it with Stycast 2850FT. One coupling is screwed to a 3/16 in. steel shaft at liquid helium temperature, using two setscrews at right angles. This shaft has a pinion helical gear pressed onto it which turns a large helical gear which is screwed onto the bottom of the grating table.

The LN_2 shield has an extension which surrounds the fiberglass shaft for half of its length. An extension of the cryostat vacuum space also surrounds this shaft. At the top of the cryostat extension, to transmit the rotational motion into the vacuum, we use a Ferrofluidic feedthrough, Model MB188-L-N-090, which has a 3/16 in. shaft going straight through the feedthrough from vacuum to atmospheric pressure, with magnetic fluid making the vacuum seal.

When the spectrometer is cold, two other mechanical feedthroughs

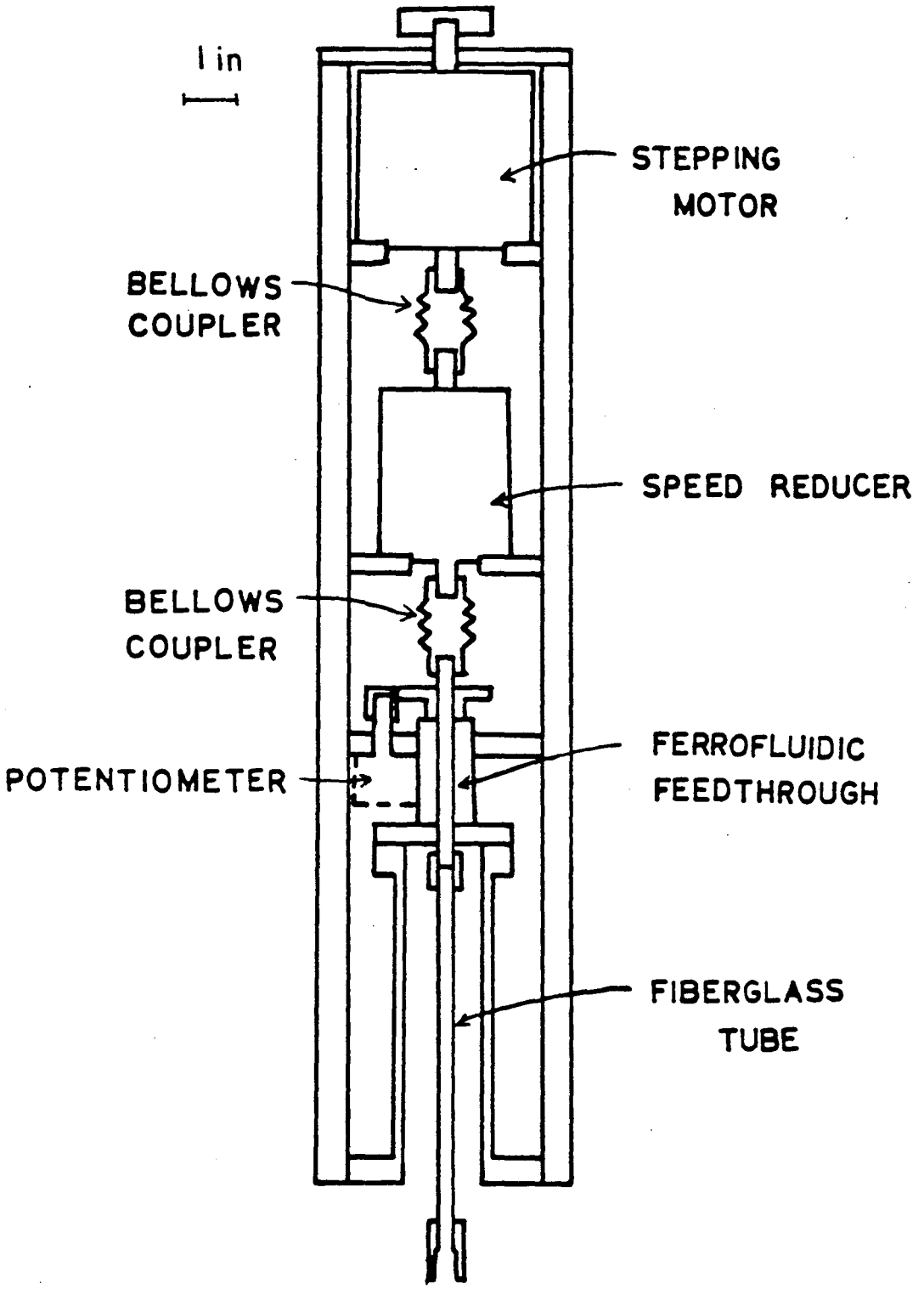

XBL 835-9628

Fig. 7. Grating Drive.

permit us to move the polarizer and the filter wheel. (See Fig. 8 for a diagram of the polarizer assembly, which will be discussed in more detail in Section 2.a.) In both cases, a detachable shaft is used to turn an element in the cold part of the dewar. Each shaft is composed of a knurled brass knob brazed to a 1/8 in. O.D., thin-walled stainless steel tube which has a piece of an Allen wrench epoxied into its other end using Stycast 2850FT. A brass Goddard Quikonnect was sealed to the outside of the dewar with either an O-ring sealed flange or epoxy. The detachable shaft can be pushed through an O-ring seal in the Quikonnect in order to engage an Allen head screw in the dewar and turn it. The screw is pinned to a pinion bevel gear which then allows the rotation of the polarizer or of the filter wheel, which are each mounted on a matching bevel gear. When the shaft is engaged, it connects room temperature to either LN_2 temperature in the case of the polarizer or LHe temperature in the case of the filter wheel. The thin-walled stainless steel tube of the shaft is of sufficiently low thermal conductivity that the heat loss is negligible for the small time that the shaft is engaged. When it is not needed, the shaft is retracted so that it does not contact any cold objects.

The procedure for cooling the cryostat is as follows. First it is evacuated by a mechanical pump and then a diffusion pump in order to obtain a good thermal vacuum. Then the cryostat is cooled by filling both its liquid helium can and its liquid nitrogen can with liquid nitrogen. Because of the large thermal mass of the optical components, about five hours are required to cool the cryostat to 77K. In practice, this precooling is usually done overnight. Then the liquid nitrogen in

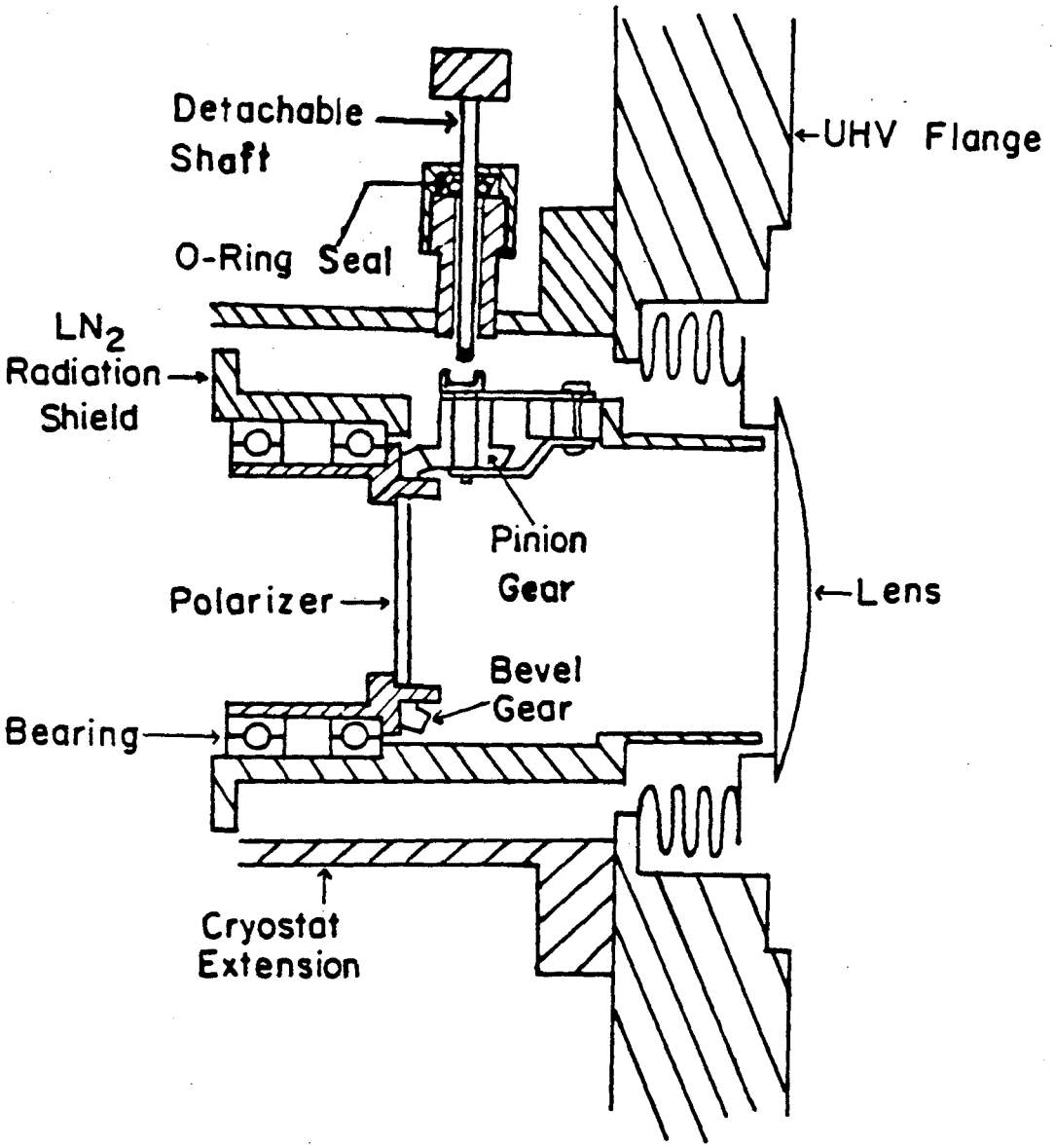

Fig. 8. Cross section of polarizer assembly, with detachable shaft at top of figure.

the liquid helium can is blown out under ~10 psi pressure of nitrogen gas. The liquid helium is transferred at a pressure of ~0.30 psi over a time period of one hour, using about 8 to 10 liters of LHe. Once the cryostat is cold, it is very efficient despite its large surface area of cold radiation shields. As long as the LN_2 can is kept cold, often with an automatic liquid nitrogen filler, the 1.2 liters of liquid helium last for 12 to 13 hours. The 1.4 liters of LN_2 last only 5 to 6 hours. Subsequent liquid helium transfers take only five minutes and use only 1.5 to 2 liters of LHe. It is therefore not difficult to keep the spectrometer at LHe temperature continuously for several days.

2. Optical Components

a. Infrared Polarizer

The infrared polarizer is a Perkin Elmer model 1860240 polarizer which is composed of gold evaporated wire grids on a AgBr substrate. It is mounted in an aluminum assembly which is screwed to the side of the LN_2 radiation shield inside the optical port of the cryostat. (See Figure 8.) The one in. O.D. polarizer is glued with a dot of Stycast 2850FT to an aluminum tube which is press fit into an aluminum bevel gear and also into two sets of steel ball bearing races. The ball bearings are then pressed into the aluminum radiation shield extension, which is painted with 3M Velvet Black paint to act as a LN_2 temperature baffle, preventing stray radiation from entering the entrance slit of the spectrometer. The polarizer can then be turned by engaging the detachable shaft with the pinion bevel gear, as described above. The polarizer is restricted by mechanical stops to rotation through an angle of 90^{o}, from passing radiation polarized parallel to the grating grooves

to passing radiation polarized perpendicular to them.

b. Entrance Slit

The entrance slit of the cryostat is composed of two razor blades glued to a piece of brass shim stock with Stycast 2850FT. The razor blades, separated by 1.0 mm, are stuck over a 3.0 mm hole in the shim stock. The size of the entrance slit is thus 1.0 mm wide by 3.0 mm high. This shim stock was soldered to a 0.5 inch diameter brass tube which was then mounted in the support for the filter wheel.

c. Filter Wheel

The filter wheel is a modified bevel gear with six openings for filters. We have six different long wavelength pass filters, purchased from Optical Coating Laboratory, Inc., which can be mounted on this wheel in order to eliminate second and higher orders of diffraction. The characteristics of these filters are tabulated in Table III. Figure 9 shows the transmittance of these filters as a function of the infrared frequency. The pinion bevel gear can be turned by a detachable stainless steel shaft at room temperature so that different filters can be rotated into the beam when the spectrometer is cold. As we turn the shaft, a detent mechanism, consisting of a phosphor bronze clip which fits into slots in the outer edge of the wheel, permits us to feel when a filter is in the proper position in the beam. The filter wheel is heat sunk through a piece of 1/4 in. diameter copper braid, which is epoxied to the wheel on one end and screwed to the spectrometer baseplate on the other. Typically, four filters are mounted on the wheel at a time, one opening is covered with a piece of aluminum foil to act as a cold beam block, and the last hole is left completely open so

TABLE III

Filter Transmission Bands of Long Wavelength Pass Filters for Grating Spectrometer

Filter Number	Transmission Band	
	Frequency (cm^{-1})	Wavelength (μ)
1	1820 - 4000	2.52 - 5.50
2	1250 - 2290	4.36 - 8.00
3	830 - 1540	6.50 - 12.00
4	690 - 1220	8.20 - 14.50
5	400 - 750	13.40 - 25.00
6	300 - 460	21.7 - 33.3

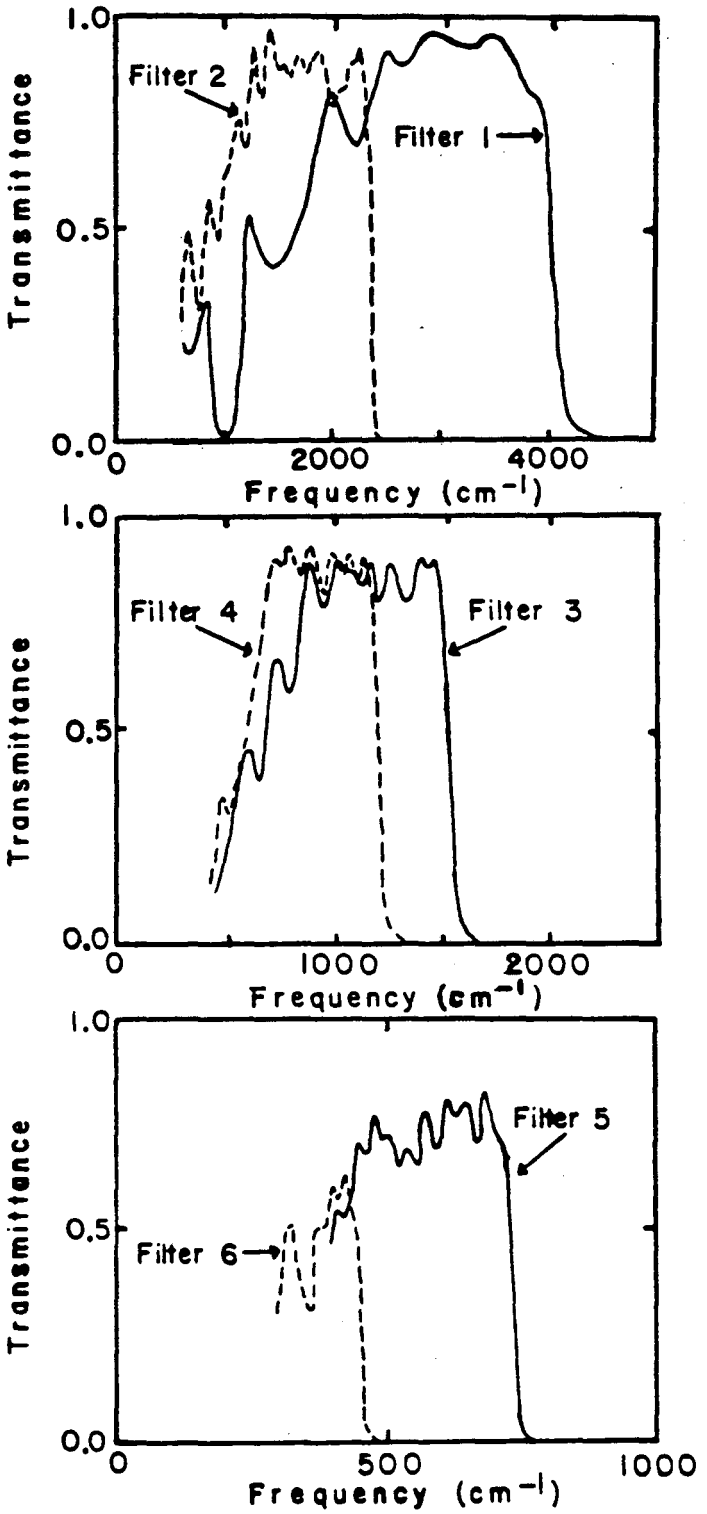

Fig. 9. Transmittance of filters for spectrometer, as a function of frequency.

that visible light from a helium neon laser can be sent through the spectrometer to calibrate the frequency scale. The filters are held onto the wheel by small clips made of phosphor bronze and also glued down with General Electric 7031 varnish, which serves to heat sink them to the wheel.

d. Plane Mirror

A small plane mirror, 2 inches wide by 1 1/2 inches high, reflects the light from the entrance slit to the collimating mirror. The plane mirror is a gold front surface mirror on a 1/4 inch glass substrate. It was cut from a larger mirror, made by Edmund Scientific Company. The mirror is held by small phosphor bronze clips against an aluminum supporting piece which is screwed onto the filter wheel stand at the appropriate height. The optical axis of the spectrometer is horizontal and 2 3/4 inches from the base plate.

e. Paraboloidal Mirrors

Both the collimating and condensing mirrors in the spectrometer are off-axis paraboloidal mirrors which were cut by Special Optics from a large paraboloidal mirror which had been spun. The mirrors are composed of a brass substrate with nickel plating, a layer of evaporated aluminum for high reflectivity, and a protective coating of SiO. The mirrors used in the spectrometer are 4 inch diameter circles with an effective focal length of 7.25 inches and an off-axis angle of 26^{o}. Each mirror is epoxied with a small dot of Stycast 2850FT to a brass holder which is screwed onto an L-shaped aluminum bracket which permits its adjustment in three directions at room temperature.

f. Diffraction Grating

We have three different diffraction gratings purchased from Bausch and Lomb Corp., which can be placed into the spectrometer one at a time to cover the range of frequencies from 330 cm^{-1} to 3000 cm^{-1}. The gratings are replicas on an aluminum substrate, whose dimensions are 90 mm x 90 mm x 16 mm. The characteristics of these gratings are summarized in Table IV. The optimal grating and filter combinations for operation in various frequency ranges are given in Table V. In Fig. 10, we show the frequency ranges for each grating in the instrument as a function of the grating angle.

The original design for the spectrometer mounted all three gratings simultaneously on a grating table. The grating table was therefore shaped somewhat like a spool, with three sets of flat edges against which the gratings rest. We had difficulty, however, in simultaneously cooling three of these gratings, with their large thermal mass, while still allowing the grating table to rotate through 360^{o}. By using only one grating at a time and constraining its rotation to $\sim 70^{o}$, we can adequately heat sink the grating table with large pieces of copper braid. The axis of rotation of the grating table, however, is still located 1.625 in. behind the face of the grating as a result of the original design constraints.

The grating is pushed against one set of flat edges on the grating table by two small clamps, one of which pushes the bottom of the grating against the table in two spots, while the other pushes the top of the grating against the table in the center. On the back of the grating, in the area which rests against the flat edges, is placed GC Electronics

TABLE IV

Characteristics of Diffraction Gratings for Spectrometer.

Grating Label	Number of Grooves per mm	Groove Spacing (μ)	Blaze Angle (degrees)	Blaze Wavelength (μ)	Blaze Frequency (cm^{-1})
A	60	16.67	28^{o} 41'	16.0	625
B	150	6.67	36^{o} 52'	8.0	1250
C	300	3.33	36^{o} 52'	4.0	2500

TABLE V

Optimum Frequency Ranges for Spectrometer Operation

Grating	Filter	Wavelength Range (μ)	Angular Range (Degrees)	Frequency Range (cm^{-1})
C	1	2.5 - 4.8	22.5 - 48.0	4000 - 2000
C	2	4.3 - 5.6	41.5 - 60.0	2325 - 1786
B	2	5.6 - 7.0	26.0 - 33.0	1786 - 1428
B	3	7.0 - 11.0	32.5 - 58.5	1428 - 909
A	4	10.0 - 14.0	17.5 - 25.5	1000 - 714
A	5	14.0 - 23.0	25.5 - 56.5	714 - 435
A	6	23.0 - 30.0	56.5 - 68.0	435 - 333

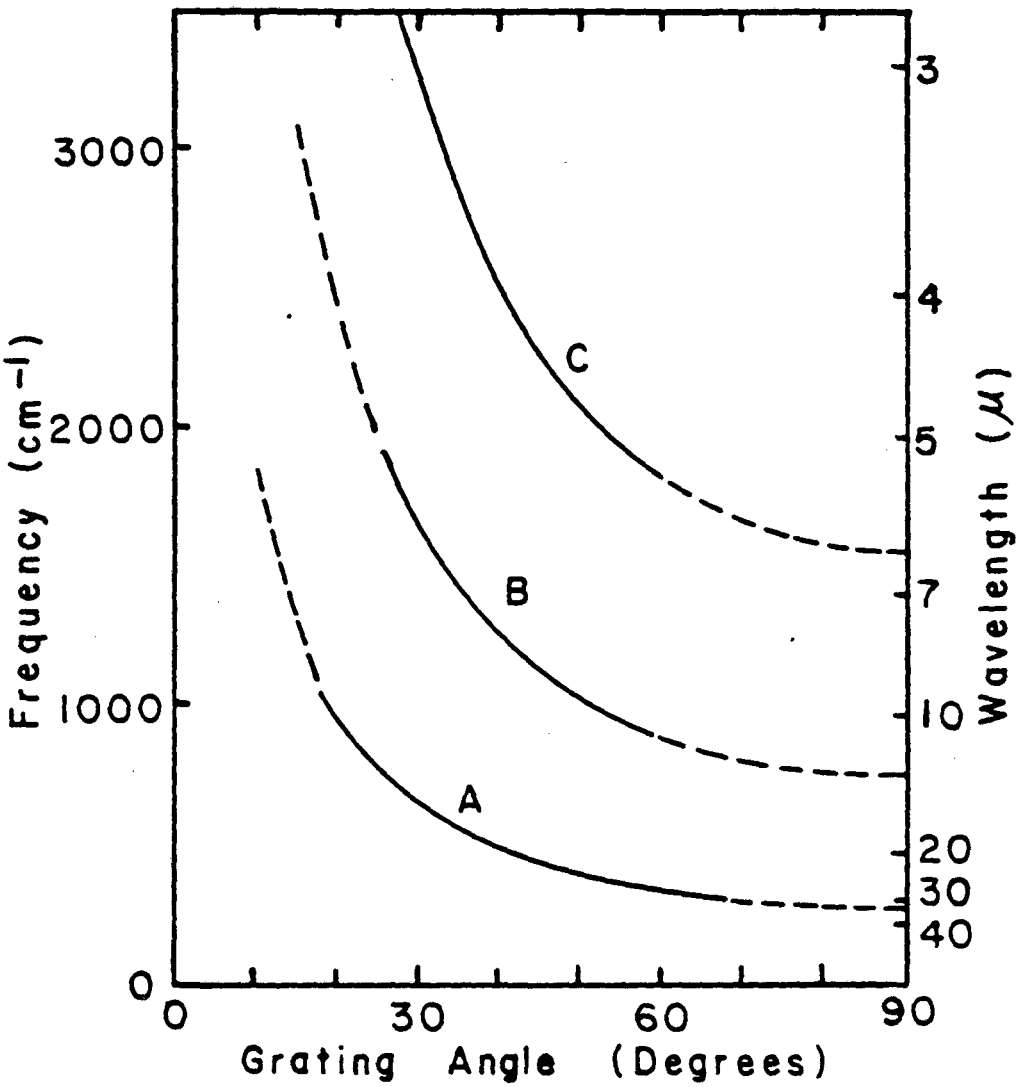

Fig. 10. Frequency versus grating angle for Gratings A, B, and C in spectrometer. The solid line indicates the suggested ranges of use of each grating.

Type Z9 Silicone Super Heat Sink Compound to heat sink the massive aluminum grating blank to the table. The grating table is rotated on a pair of stainless steel ball bearings about a fixed shaft, as is shown in Fig. 11. On the bottom of the grating table is mounted a large helical gear with 140 teeth. This gear mates with a small helical pinion gear which drives the grating motion with a 10:1 gear reduction. The pinion gear is pressed onto a 3/16 inch shaft which rotates in a fixed supporting piece on another pair of stainless steel ball bearings. All of the sets of ball bearings were carefully degreased to insure that they would be able to turn at liquid helium temperatures. Since the aluminum supporting piece contracts more than the stainless steel bearing races, the races were only loosely fit into their mating parts at room temperature so as to allow enough clearance for the bearings to turn when they are cooled. Before installation into the spectrometer, cold tests at liquid nitrogen temperature were performed to test the mechanical performance of these moving parts.

g. Detector

The detector in this experiment is an Si:Sb photoconductor, made by Rockwell International. Such detectors were developed for use in satellite astronomy, where high responsivity and low noise even in very low background fluxes is essential. Our detector is of a quality suitable for astronomical work on NASA's Infrared Astronomy Satellite. Using the amplifier circuit described below, we have measured its noise equivalent power as 10^{-16} watt/$Hz^{1/2}$ at 2000 cm^{-1}. The dimensions of the detector are 2 mm x 1 mm x 1 mm. The detector is mounted inside a gold-plated copper integrating cavity with a front aperture 2 mm high x

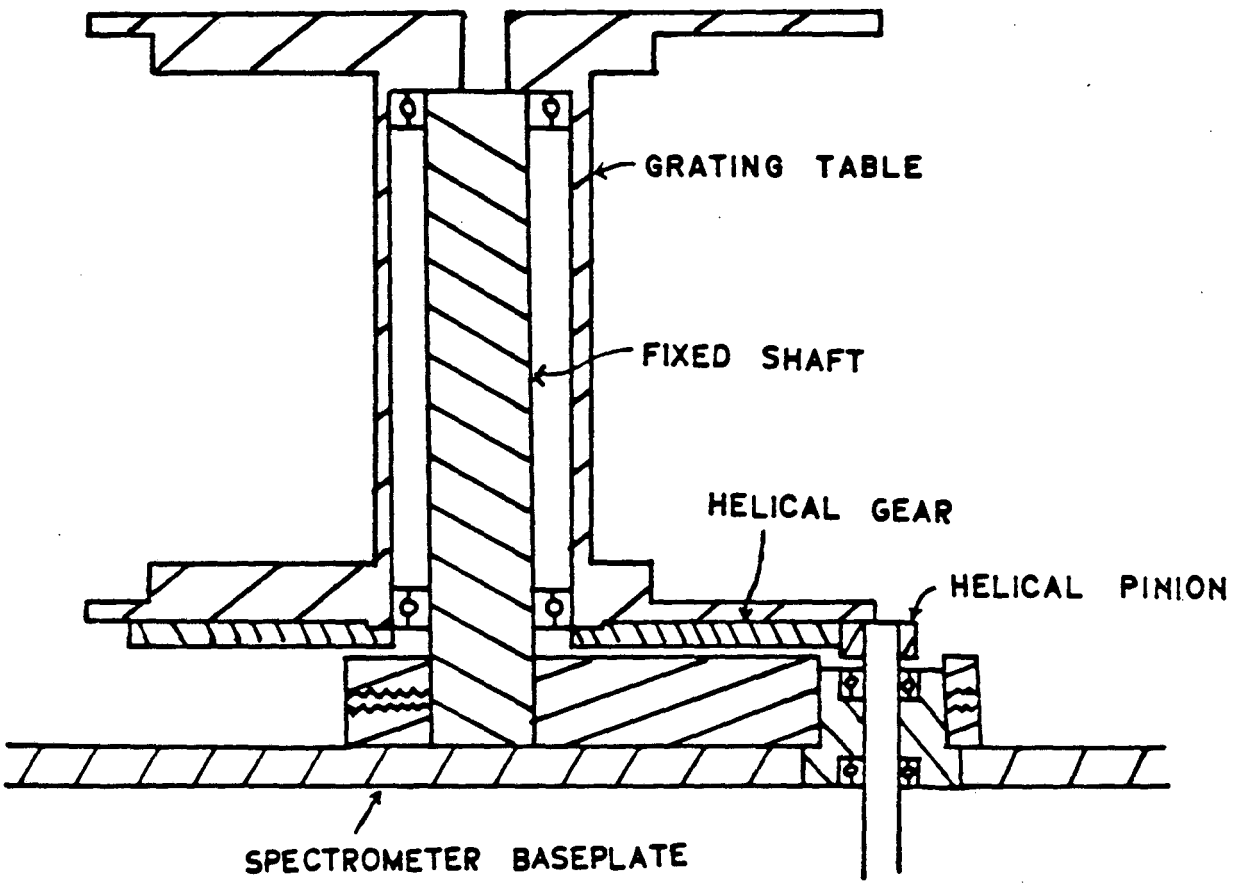

Fig. 11. Vertical cross section of grating table assembly.

1 mm wide. The detector is turned at a 45^{o} angle with respect to the front surface of the cavity so as not to reflect too much light directly backwards.

With a constant voltage bias on the detector, the current through the detector is directly proportional to N, the number of photons per second incident upon the detector.[40]

$$I = eG\eta N \tag{36}$$

In this equation, I is the current through the detector, e is the charge of the electron, G is the photoconductive gain, η is the quantum efficiency of the detector, and N is the number of photons per second.

The detector has extremely high impedance at low background fluxes, ranging from 10^{9} Ohms when the entrance slit of the spectrometer is open to room temperature radiation to 10^{12} Ohms when it is filled by liquid helium temperature radiation. Since the impedance of the detector is so high, we must place a preamplifier with high input impedance and low noise very close to the detector. A special transimpedance amplifier (TIA) circuit, with such a preamplifier stage, is used to convert the current through the detector into an output voltage.[41] This circuit is shown in Figure 12. The preamplifier is a source follower with unity gain, using a JFET 00 package from Infrared Laboratories, which contains two matched J230 junction field effect transistors (JFETs). This package is designed so that its outside can be clamped to a surface at liquid helium temperature while the JFETs generate enough heat to work at their operating temperature of about 90K. The load resistor in the TIA circuit is a 10^{9} or 10^{10} Ohm Victoreen metal oxide resistor. The detector, the load resistor, and the JFET package are all mounted

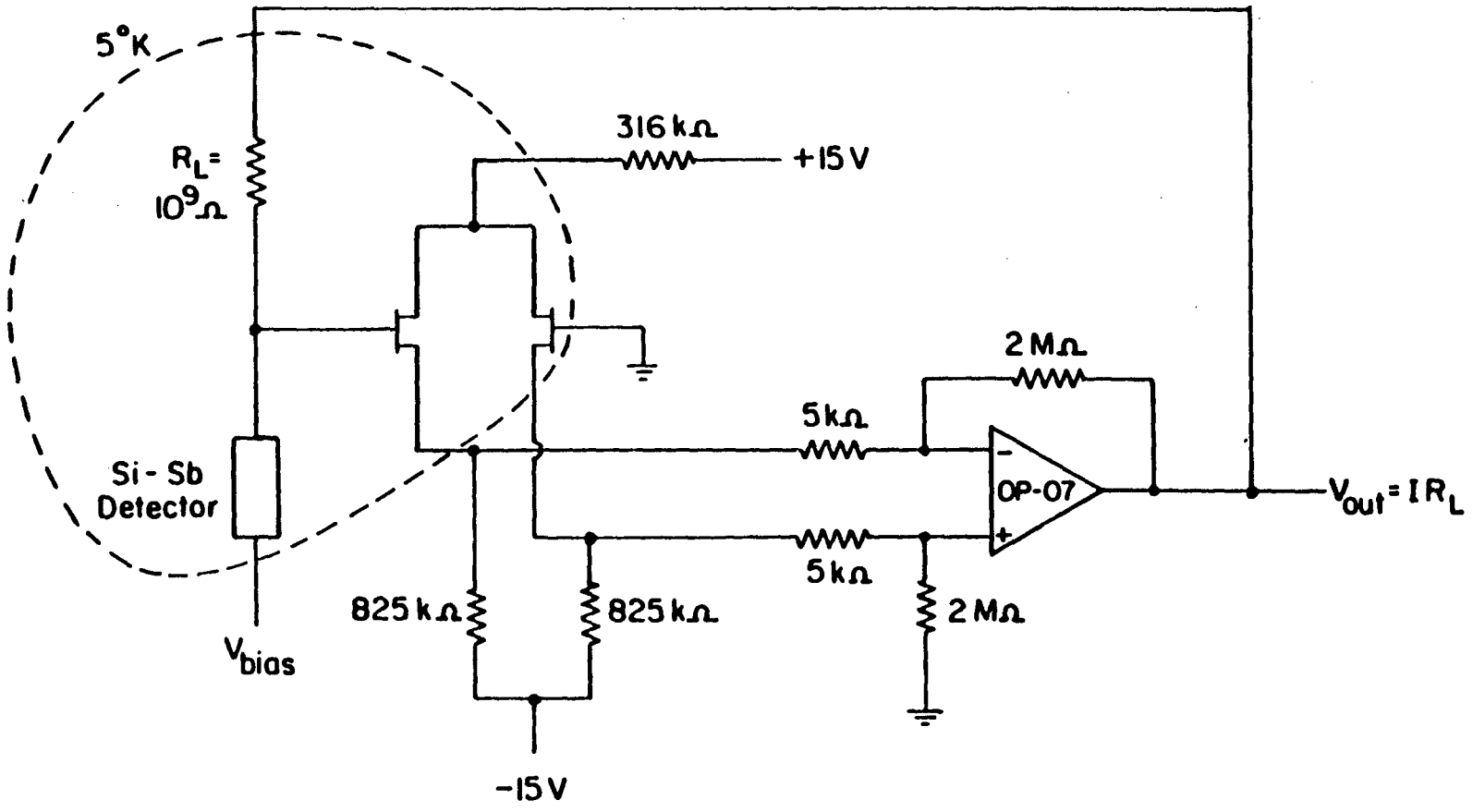

XBL 835-5685

Fig. 12. Transimpedance amplifier detector circuit.

together on a small printed circuit board about 2 inches wide by 4 inches high. This board is then mounted on a small translation stage so that, when the spectrometer is open, it can be moved forward and backward in order to focus the best image on the detector. These components are connected through the dewar wiring to an external electronics box which contains the other elements in the circuit. A low noise OP-07 operational amplifier by Precision Monolithics is used in the circuit.

In the TIA circuit, the detector is operated under constant voltage bias, and the output voltage of the circuit is proportional to the current through the detector. The JFETs are biased to hold the node between the detector and load resistor at a virtual ground. A pair of mercury batteries and a voltage divider supply the bias voltage to the other side of the detector. Incoming photons cause a change in the current through the detector. Since the current cannot flow into the gate of the JFET because of the high input impedance, it is forced to flow through the load resistor. Thus the voltage at the output of the operational amplifier is equal to the current through the detector times the load resistance, by Ohm's law. This output voltage, which is proportional to the number of photons/sec incident on the detector, can then be measured on a voltmeter or sent to the analog-to-digital converter of a computer.

3. Grating drive

The grating drive is mounted on the outside of the dewar and was shown in Figure 7. Each component of the drive mechanism is supported on a plate between two long aluminum side pieces. The grating motion is

driven by a Slo-Syn stepping motor, which is controlled by a Slo-Syn preset indexer. Under computer control, the indexer steps the motor a fixed number of steps at a time. At the top of the motor, a knob permits the grating drive to be turned manually when the indexer is turned off. The output shaft of the motor is connected by a bellows coupler to a PIC 20:1 speed reducer. This output shaft from the speed reducer is connected by another bellows coupler to a Ferrofluidic feedthrough, described earlier in Section 1 of this chapter.

A voltage readout has been provided to indicate the angular position of the diffraction grating. On the input of the ferrofluidic feedthrough is mounted a small spur gear. It turns another spur gear which is mounted on a ten-turn potentiometer. A voltage of 9.00 V is applied across the potentiometer, and the voltage at the wiper can be read on a voltmeter or applied to the x-axis of a chart recorder. The 5:1 gear ratio is chosen so that the voltage across the potentiometer corresponds to the rotation of the grating at a rate of 0.25 V per 2^{o} of grating rotation. Our primary measurement of the change in the angle of the grating during a spectrum, however, is the number of steps of the stepping motor between data points. Absolute calibration of the grating angle is done by measuring the angular positions of helium-neon laser lines, as is described in Chapter IV.

As mentioned above, the grating angle is constrained within $\sim 70^{o}$ by the copper braids used to heat sink the grating table. If the grating is accidentally turned so that its angle is outside of this range, something in the grating drive, such as a bellows coupler, may break. Therefore, a electrical interlock has been installed to prevent the

accidental movement of the grating, under computer control, outside of the permissible range.

B. Ultrahigh Vacuum System

1. Facilities

The ultrahigh vacuum (UHV) system is a conventional Varian system, made completely of stainless steel. The bottom half is a Varian FC-12E pumping station, equipped with five small ion pumps surrounding the chamber. Each has a pumping speed of 40 l/sec, so that the entire system pumping speed is 200 l/sec. The system is also equipped with a titanium sublimation pump (TSP) composed of a source with three filaments and a TSP shield. Above these two pumps is an 8 inch poppet valve with a Viton O-ring seal, which can be used to seal off the pumps from the rest of the system. The top half of the system is a stainless steel bell jar with many auxiliary ports and flanges. It is equipped with four 8 inch O.D. ports around the sides, one 6 inch O.D. port at the top, and eleven 2 3/4 inch ports. It is sealed to the bottom half of the system by a 12 inch diameter Wheeler flange, with 18 clamps holding the copper wire seal. Except for the indium seal of the infrared lens to a stainless steel flange, all other seals on the system are made with Varian Conflat flanges, with the knife edges in the flanges cutting into flat copper gaskets to make a seal. The base pressure of the system is 1×10^{-10} torr. If the system has been baked for several days, the pressure is often in the mid-10^{-11} torr range.

The system is equipped with a Varian model UHV-24 nude Bayard-Alpert ionization gauge and a Granville-Phillips model 271 ionization gauge controller, with an electron bombardment gauge degassing facility,

to measure pressures between 10^{-3} and 10^{-11} torr. It also has a Varian 3 keV ion gun with power supply for argon ion sputter cleaning of samples. In addition, a Huntington sample manipulator is mounted in the top 6 inch flange and described in more detail in Section 2 below.

The UHV system is rough pumped by an exterior manifold which has a Varian Vacsorb molecular sieve sorption pump and a liquid nitrogen trapped diffusion pump. A bakeable valve seals the system from the rough pumping line. When the system is pumped down from atmospheric pressure, the first stage of pumping is done with the liquid nitrogen cooled sorption pump until the pressure is below 100 microns. Then the diffusion pump is used to bring the pressure down to about 10^{-7} torr before the roughing manifold is sealed off from the UHV system. The ion pumps are then permitted to pump on the system. The diffusion pump, Varian model HS-2, is backed by a mechanical roughing pump with a molecular sieve trap between the mechanical pump and the diffusion pump. The water cooled diffusion pump has a temperature interlock to shut off the pump heater if the pump becomes too hot. The diffusion pump is equipped with a Varian model 325 cryotrap, which is a liquid nitrogen cooled trap to prevent diffusion pump oil from backstreaming into the UHV system. The sorption pump and the diffusion pump are individually sealable from the roughing manifold. Both the sorption pump and the molecular sieve trap on the mechanical pump are baked when necessary to regenerate the sieve.

The UHV system is also equipped with a gas handling manifold for the admission of controlled amounts of gas for sample cleaning and dosing. A Varian leak valve is mounted on a 2 3/4 in. flange on the UHV

system and is connected through a stainless steel tube to the rest of the gas manifold. The stainless steel bakeable gas line is connected through a valve to the roughing manifold so that it can be pumped out by the sorption pump and the diffusion pump. The gases are admitted from Matheson lecture bottles through stainless steel valves to the gas line.

The UHV system is well equipped with facilities for characterizing the surfaces of samples by standard techniques. The system is equipped with a Varian electron gun and optics for low energy electron diffraction (LEED). Potentials can be applied to the grids in the LEED optics to enable the measurement of Auger spectra by the retarding field Auger technique, thus permitting the detection of atomic contaminants on the surface. In addition, the system is equipped with a mass spectrometer, VG Micromass model Supavac, for measuring the partial pressures of residual gases in the vacuum system in the range 10^{-4} to 10^{-11} mbar. The mass spectrometer is also used for measuring thermal desorption spectra, which measure the partial pressure of a particular gas in the system as the sample temperature is ramped upwards at a constant rate.

The ultrahigh vacuum system is equipped with ovens for system bakeout after exposure to atmospheric pressure. When the system must be opened to the atmosphere, it is vented using dry nitrogen gas from a cylinder. After rough pumping as described above, the system is pumped by the ion pumps down to the 10^{-7} to 10^{-8} torr pressure range. Then it is baked for one or two days at 110^{o}C to reach its ultimate pressure.

The ultrahigh vacuum system is mounted inside an aluminum table, built by the LBL Installation Shop. The table has a frame made from

aluminum pieces with a square cross section that have flanges attached for the connection of side panels. The table has a bottom panel made of 3/8 inch aluminum sheet which has large wheels connected to it on the underside so that the whole table can roll. The side panels are made of 1/8 inch thick aluminum sheet. The table top is made from 1 inch thick Colorlith (Johns Manville Co., Denver, CO), a material which is made from pressed asbestos fibers so that it has good thermal insulation properties. On each panel which surrounds the bottom of the ultrahigh vacuum system is mounted Owens Corning fiberglass building insulation, type R-11. Six General Electric Calrod strip heaters are attached directly to the outside of the bottom half of the stainless steel vacuum system. These strip heaters are each 17 3/4 in. long, with power consumption of 500 watts each at 120 volts. Thus the bottom part of the table which surrounds the vacuum system acts as an oven.

A separate oven was constructed to bake out the top part of the system. This oven is constructed from 1/32 in. aluminum sheet rolled into two concentric shells separated by 2 in. ceramic spacers and fiberglass insulation. The outer shell of this oven is 38 in. in diameter and 38 in. high. Four strip heaters are mounted on the inside of the oven, supported by ceramic spacers. The oven is suspended from the ceiling by a block and tackle over the top of the ultrahigh vacuum system. When it is needed for bakeout, it can then be conveniently lowered over the system.

The temperature of the top oven is regulated by a Honeywell Dialapak on-off temperature controller. This instrument turns the current to the top oven on or off depending on the relationship of the

temperature sensor to the setpoint. The sensor is a chromel-alumel thermocouple which is screwed to the outside of the 8 inch flange for the infrared optics. The setpoint of the controller is set to 110 degrees so as not to melt the indium which seals the infrared lens into that flange. At this temperature, bakeout of 24 hours is usually sufficient to reach a base pressure of 10^{-10} torr.

The temperature of the bottom of the system during a bakeout can be read on another chromel-alumel thermocouple which is screwed to the bottom half of the system. In fact, this temperature could be regulated by the controller instead of the temperature of the top oven if that were desirable.

In practice, each bank of heaters is connected to a Variac in order to better control its current. The Variac for the top oven is then plugged into the temperature controller so that its current can be regulated. The Variac for the bottom heaters is connected to the line voltage. In addition, a heating tape is wound around the tubing and the bakeable valve which connect the lower part of the vacuum system to the roughing line. This heating tape is then connected to a third Variac which is connected to the line voltage.

2. Sample Holder

The sample is mounted on a holder on the end of a Huntington high precision sample manipulator, model PM-600XYZRC, which is mounted in the top 6 inch O.D. flange of the system. This manipulator permits x and y translations of up to $\pm$12.5 mm $\pm$0.003 mm, translation in the z (vertical) direction up to 50.00 mm $\pm$0.01 mm, rotation through 360

degrees, and 13.0 mm of linear coaxial travel. In this vacuum system, Varian designed the stainless steel bell jar and the LEED optics so that the sample position should be 2 1/2 inches from the center of the chamber for LEED and retarding field Auger studies. Since the manipulator axis is located at the center of the chamber, the sample holder includes an L-shaped bracket to mount the sample off the axis of the chamber. (See Figure 13.) The sample can then be moved along a circular path by changing the rotation angle of the manipulator. This movement of the sample around the chamber positions it, in turn, in front of various pieces of apparatus for different types of analysis. In the rear of the chamber, the sample faces the LEED optics for LEED and retarding field Auger spectroscopy. The sample can be also be moved to the left side of the chamber in front of the infrared port. In the front of the chamber, it can be easily viewed through the large glass viewport. Finally, it can be moved to the right side of the chamber for argon ion sputtering.

The other mechanical parts of the sample mount are designed to turn the coaxial linear motion of a small shaft inside the principal manipulator shaft into a rotation of the sample about the vertical axis in the plane of the sample. This permits the sample to be turned from normal incidence to the LEED electron gun and optics to near grazing incidence for maximum infrared surface signal.

The mechanism, which is shown in Figure 13, consists of a stainless steel pushrod which is pushed by the manipulator's inner coaxial shaft against the end of an L-shaped lever. Attached to the other end of the lever is a rack which then turns a small gear which is pressed onto the

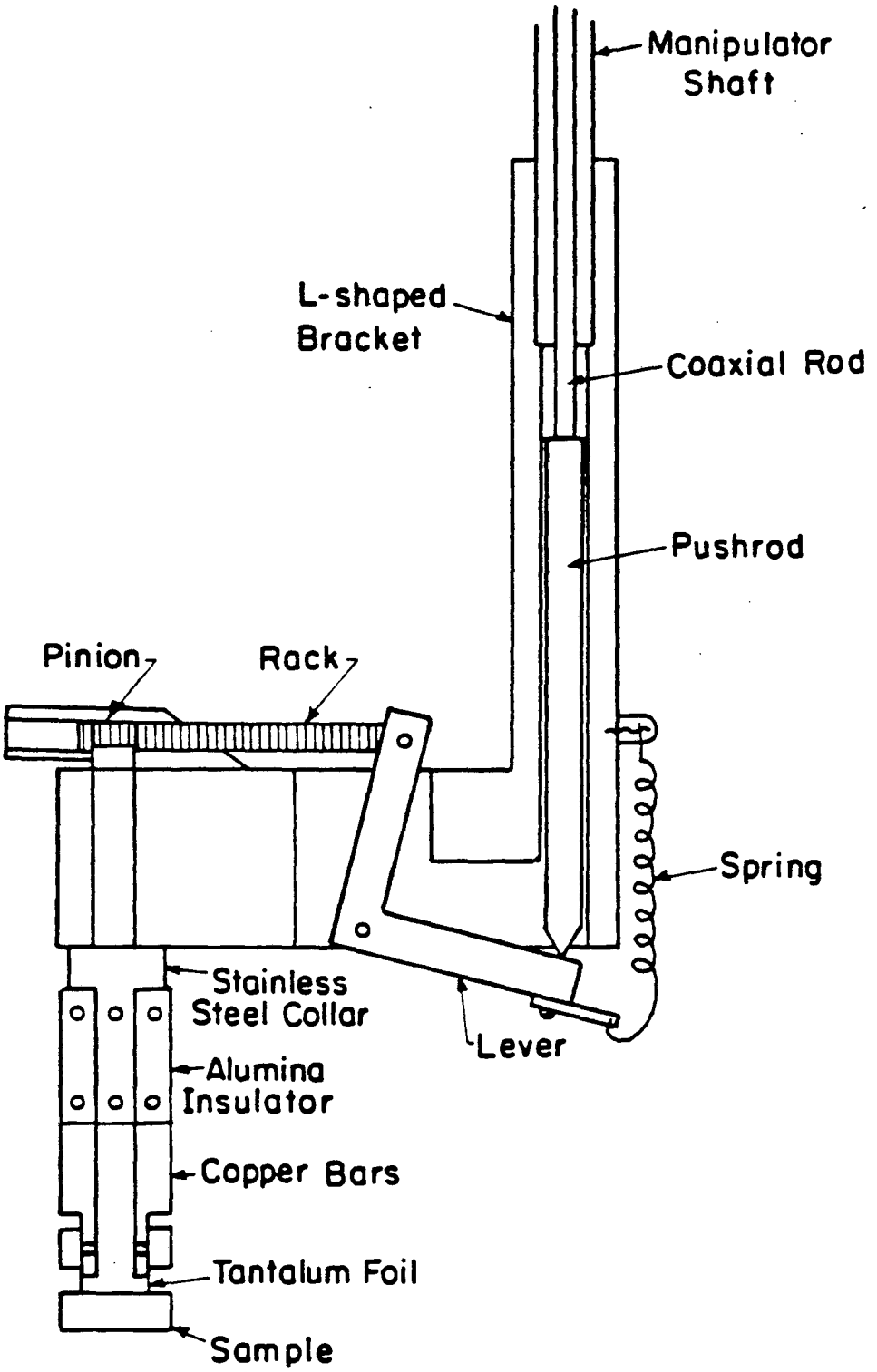

Fig. 13. Sample holder, with cut-away view of L-shaped bracket showing mechanism which turns the sample from normal to grazing incidence.

shaft on which the sample rotates. Thus, the sample is able to perform the required rotation about the vertical axis in its plane.

The sample must be heated to temperatures in the range 600 to 900^{o}C in order to clean it. The sample is spot welded directly to 0.006 in. thick tantalum strips, and current is run directly through it to heat it resistively at the spot welds. These strips are then screwed to copper bars, 3/16 in. square by 1 5/8 in. long. The copper bars are screwed to an alumina insulator, which is in turn screwed to a stainless steel extension on a collar which is pinned to the aforementioned shaft. The bars are connected by 3/16 in. copper braid, which is insulated by fiberglass sleeving, to 1/4 in. copper feedthroughs which are mounted on the 6 inch O.D. flange of the manipulator. These feedthroughs are then connected by #6 welding cable to a Hewlett-Packard 6260A power supply, which is capable of providing up to 100 amperes at 10 volts. The current required to heat the sample depends on the resistance of the spot welds to the sample. If the resistance is high, less current is required to heat the sample, but the spot welds may more easily break under thermal cycling, necessitating the removal of the sample manipulator from the UHV system in order to repair the spot welds. Clearly a compromise is required between the strength of the spot welds and their resistance. We have usually had good success using three to five spot welds with 12 watt-sec of spot welding energy. Under these conditions, about 20 to 25 amperes of current usually suffices to heat the sample to about 700 degrees Celsius. The current leads from the power supply to the feedthroughs on the manipulator have a 35 ampere fuse to prevent unintentionally destroying the spot welds with too much

current.

The sample has a chromel-alumel thermocouple junction spot welded to its back surface so that its temperature can be measured. The thermocouple wires are fastened to a Macor (Corning Glass Works, Corning, NY) insulator close to the sample in order to prevent the spot weld of the junction to the sample from breaking as the sample is rotated. Beyond the point where they are fastened, the wires are insulated with fiberglass sleeving and spot welded to a chromel-alumel thermocouple feedthrough mounted on the manipulator flange.

The sample temperature is regulated by a feedback temperature controller, built by the Department of Physics Electronics Shop, which controls the sample current in proportion to the difference in the sample temperature and the temperature setpoint. (See Fig. 14) The output of the chromel-alumel thermocouple on the rear of the sample, with a thermocouple reference junction in an ice bath at $0^{o}C$, is fed into the input of the temperature controller. The controller has a Precision Monolithics OP-27 ultra-low noise operational amplifier as its input stage, with a gain of 100. The output of the first stage can be measured on a voltmeter to yield a sample temperature reading. The difference between this voltage and a preset voltage reference is amplified and applied to the programming terminals of the Hewlett Packard power supply which supplies the heating power. The power supply is operated in the constant current mode, with the output current linearly proportional to the programming voltage. The output of the temperature controller has a diode which limits the programming voltage to the power supply, causing the current through the sample to be

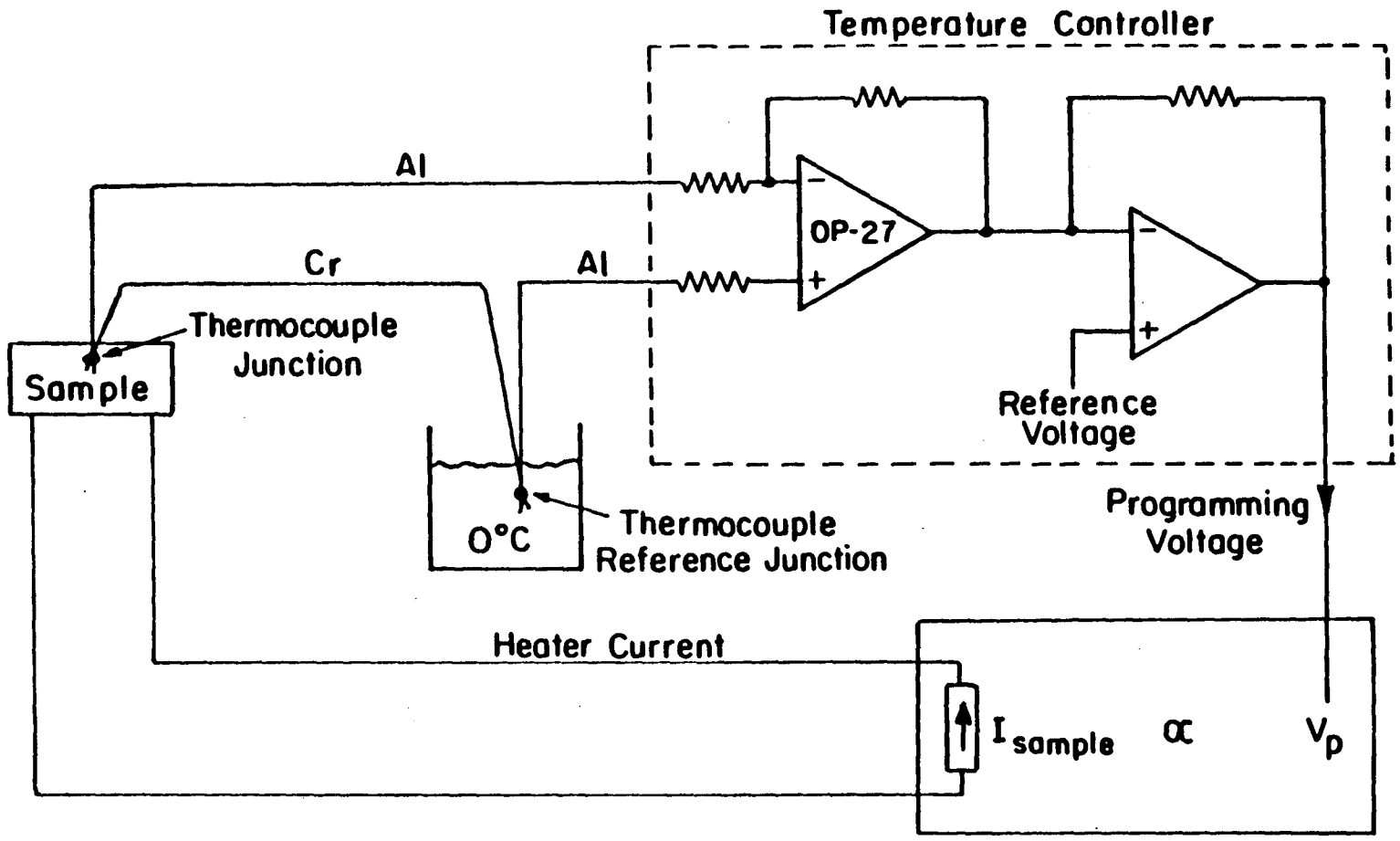

Fig. 14. Block diagram of feedback loop controlling sample temperature.

limited to 60 A. In addition, a potentiometer can be set to limit the current to some smaller amount.

When the sample temperature is to be held constant, the voltage reference for the controller is provided by an LM399, which is a temperature stabilized Zener diode with 6.95 V output. This voltage is applied to any one of six potentiometers, providing various fixed temperatures by switch selection.

The voltage reference for the sample temperature controller can also be connected to a digitally generated ramp voltage with speed adjustable by a ten turn potentiometer between 60 and 200 mV per second. This type of voltage reference thus permits the performance of thermal desorption spectroscopy (TDS) with a constant temperature rate of 7 to 25 degrees Kelvin per second. The ramp voltage is controlled by buttons to start, stop, and reset the ramp. The ramp can either be run continuously or in a single sweep mode. The maximum voltage which the ramp attains can be set on one of three small potentiometers which are each adjustable with a small screwdriver.

Finally, the temperature controller has a manual override mode in which the voltage reference is set to the maximum provided by the 6.95 V temperature stabilized Zener diode, and the current to the sample is then controlled directly by the current limit potentiometer.

3. UHV Optics

In order to perform the emission experiment, a limited number of optical components are needed inside the ultrahigh vacuum system. These components are all mounted together on one 8 in. O.D. flange which is bolted into the large port on the left side of the vacuum system in

Fig. 5. Thus, a similar flange could be bolted into any conventional ultrahigh vacuum system with a suitable port, thus permitting the performance of infrared emission spectroscopy on the sample in addition to other more conventional surface analysis techniques. The vertical cross-section of this assembly is shown in Figure 15.

Since the largest surface signal is obtained at near grazing incidence, and the sample is a highly reflective metal, we must place a cold, black object behind the sample to keep the warm background of the surrounding stainless steel ultrahigh vacuum system from reaching the entrance slit of the infrared spectrometer. Therefore, we place a liquid nitrogen temperature blackbody behind the sample. This blackbody consists of concentric circular grooves made with a lathe tool, with an angle of 25 degrees, in a circular piece of copper about 1/4 inch thick. This blackbody will have properties similar to that of a cone of which has an angle of 25 degrees, except that the ridges will have additional reflections. A cone with such an angle would have every ray incident upon it reflect at least four times before leaving it. Our blackbody is then blackened with gold black, which consists of particles of evaporated gold.

Using our spectrometer, we have measured the emissivity of gold black to be ~0.97 in the range from 900 to 1600 cm^{-1}. The gold black is placed onto the optical components by evaporating gold in ~10 torr argon atmosphere in a separate evaporator. This process causes the gold to form small particles, about 100 Å in diameter, which then scatter light in such a way that they are highly absorptive for wavelengths much greater than the particle size.[42]

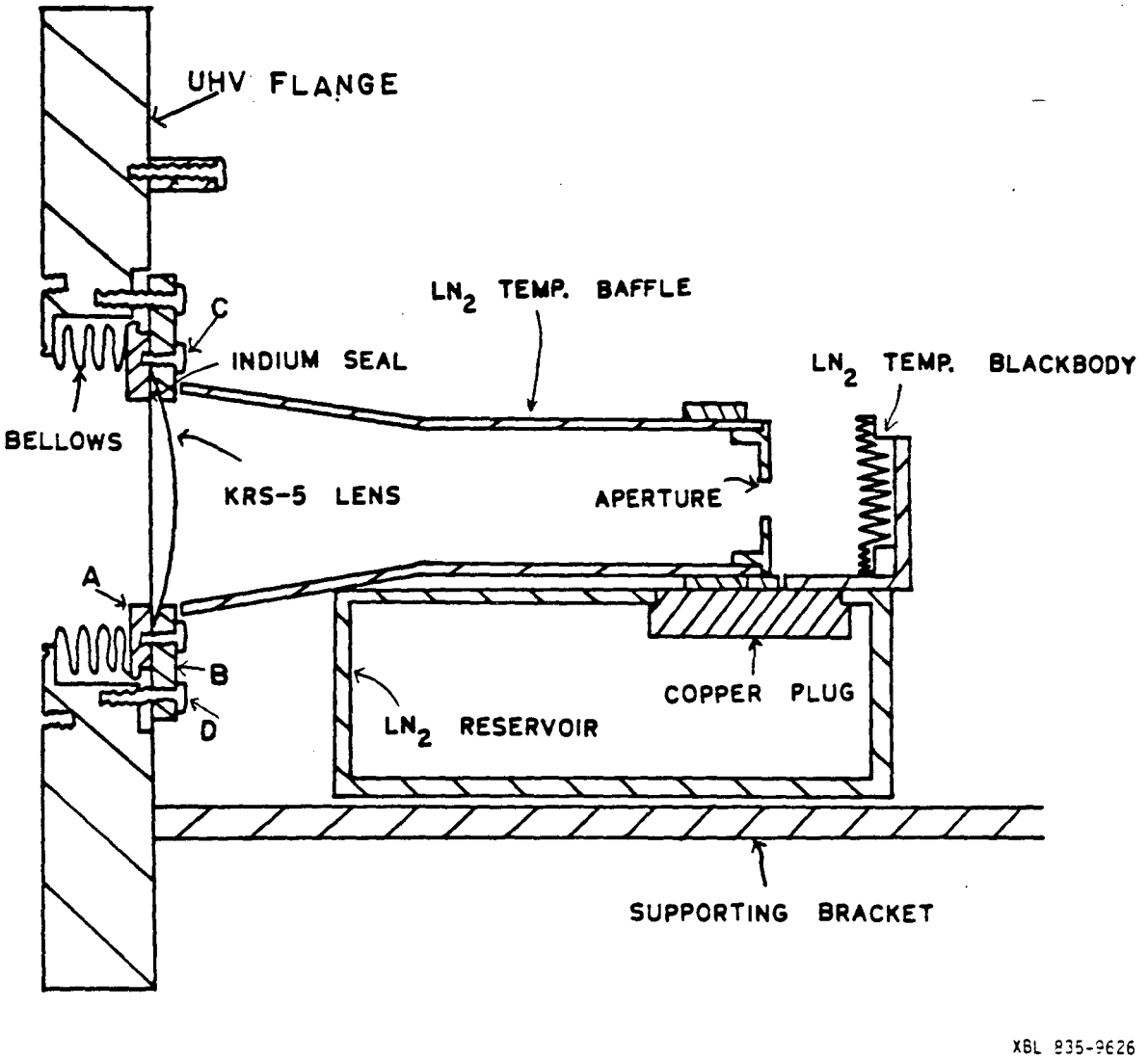

Fig. 15. Vertical cross section of flange with UHV optics. Labels A-D aid the discussion in the text of the indium seal of the lens to the flange.

A piece of stainless steel machined from a section of a tube is mounted onto the 8 in. O.D. flange as a strong supporting piece. Its dimensions were chosen to fit into the available 8 in. porthole. It was made quite long so that additional optical components could be easily mounted behind the sample if necessary, such as an infrared source for the more conventional reflection-absorption type of experiment.

A liquid nitrogen reservoir is mounted in the ultrahigh vacuum system. This can is made from a piece of stainless steel rolled into a section of a cylindrical shell with flat plates welded on top and on the ends. The can fits neatly between the optical path and the stainless steel supporting piece described above, to which it is connected by four stainless steel strips, 1/4 in. wide by 2 in. long by 0.020 in. thick. Before the assembly of the can was completed, a copper plug was vacuum brazed into its top to act as a liquid nitrogen temperature heat sink for the cold optical components needed in the UHV system. Inside the can, a piece of copper sheet, soldered to the bottom of the plug, reaches around the inside of the can to its bottom to provide heat conduction between the liquid nitrogen and the copper plug, even when the nitrogen level is very low. The volume of the can is 0.3 liter, and it is able to hold LN_2 for about two hours.

The can is supplied with LN_2 through two feedthroughs made of stainless steel which were welded into the flange. The feedthroughs were designed with a 3/16 in. tube going from the outside of the system to the can, and larger 3/8 in. tubes welded to the outside of the smaller tubes and to the large flange. This re-entrant design provides some vacuum insulation for the feedthroughs. Inside the UHV system, the

feedthrough tubes are welded to 1 1/3 in. mini-Conflat flanges, which mate with similar flanges on the can to permit easy assembly.

All of the cold optical components in the UHV system are made of oxygen-free, high conductivity (OFHC) copper. They are all clamped to copper brackets which are screwed to the copper plug brazed into the top of the liquid nitrogen can. Indium foil, 0.005 in. thick, is pressed between each pair of surfaces to obtain high heat conductivity from the heat sink to each optical component.

A large, cold copper baffle surrounds the optical path between the sample and the infrared lens. In the end of the baffle near the sample is mounted a circular copper piece with an hole in it, which acts as an oversized slit to permit radiation from the sample to reach the lens. The baffle and the piece with the aperture are both blackened with gold black.

The large flange also has three small radial ports built into it using 1/2 in. O.D. tubing and mini-Conflat flanges. Only one of these ports is currently in use. It has an eight-wire electrical feedthrough mounted in it, with four pairs of chromel-alumel thermocouple wires spot welded to it. The spot welded thermocouple junctions are screwed to various cold optical components so that their temperature can be monitored. The thermocouple screwed to the back of the LN_2 blackbody typically produces a voltage of -6.36 mV, relative to room temperature, so that its temperature is probably about 100K.

In the center of the 8 in. O.D. flange is mounted the plano-convex KRS-5 (thallium bromide mixed with thallium iodide) infrared lens, obtained from Unique Optical Company. Refer to Figure 15 for the

following discussion of the vacuum seal of the lens to the UHV flange. A stainless steel bellows was welded to the large flange and, on the other end, to a stainless steel ring with a flat surface (A). A ring of indium, 0.005 inch thick, was placed onto this flat surface, and the plane side of the lens was laid against the indium. Then another stainless steel ring (B), which had been machined on one surface to have the same curvature as the lens, was placed over the lens and screwed down hard onto the other ring with twelve screws (C). The indium foil thus forms the vacuum seal between the lens and the pieces welded to the flange. The vacuum integrity of this seal was checked by placing an auxiliary O-ring sealed flange on the outside of the large flange, pumping out the space on the outside of the lens, and checking it with a leak detector. Other screws (D) between the stainless steel ring assembly and the large flange fix the position of the lens by allowing the expansion or contraction of the bellows, thus adjusting the lens distance from the large flange. The lens is currently is at room temperature and is thus the only warm optical component in the beam. Since it is mounted on a thin bellows, it could probably be cooled if necessary.

On the outside of the large flange are eight tapped holes so that the cold grating spectrometer can be bolted directly onto the side of the UHV system. Thus the infrared lens acts as a vacuum window between the two systems. The entire optical path is evacuated, since the apparatus consists of a UHV system on one side, pumped down to 10^{-10} torr, and a cryostat with thermal vacuum on the other, pumped down to 10^{-6} torr with a diffusion pump before it is filled with cryogens which

certainly bring the pressure down further.

C. Methods of Optical Alignment

The spectrometer was aligned at room temperature when it was open to the atmosphere. We placed a visible lamp in front of the entrance slit and observed the focussed image by eye. The diffraction grating was replaced by a plane mirror for the alignment procedure. We adjusted the collimating mirror to obtain a nearly parallel beam at the position of the plane mirror on the grating table. Then we adjusted the condensing mirror to obtain the sharpest image at the detector. Although the detector assembly is mounted on a translation stage so that it can be moved towards the condensing mirror for better focussing, in practice, that direction of movement is not very critical to the alignment.

Since the adjustment screws for the KRS-5 lens are only accessible when the UHV flange is on the bench, the alignment of the UHV optics cannot be done when the flange is inside the vacuum system. We measured the focal length of the lens at infrared frequencies by using a nichrome filament source and a room temperature pyroelectric detector. We then adjusted the lens position to focus light from the position of the sample onto the entrance slit of the spectrometer. Since the lens is the only optical element inside the UHV system, it is fairly easy to position it properly.

Very little optical alignment can be performed when the spectrometer and the UHV system are both under vacuum. In the horizontal direction, the rotation of the diffraction grating will move the image onto the detector, so that small alignment errors in the

horizontal plane are not important. The entrance slit to the spectrometer is deliberately oversized in the vertical direction in order to be certain that radiation will be incident on the detector. We have found, however, by laborious trial and error procedures that we obtain more infrared photons at the detector if the room temperature visible image is not centered on the detector, but displaced about 2 mm vertically. Making small changes in the optical alignment of the spectrometer is very cumbersome because it is important to know the effects of the changes when the instrument is cooled. Thus, the change must be made at room temperature when the instrument has been opened; then the spectrometer must be cooled to liquid helium temperature in order for the detector to operate so that the modification can be evaluated. If the alignment still needs to be corrected, the instrument must then be warmed back to room temperature before further adjustments can be made.

We can, however, adjust the sample position with the manipulator when the whole system is assembled and ready to measure data. In fact, we performed an experiment on CO on nickel to determine the sample position for the maximum signal from the adsorbed molecules. Once we have determined the correct sample position for the infrared experiment, we can replace the sample reproducibly in that position for many weeks, or even months, to obtain infrared emission spectra of adsorbed molecules which have a good signal to noise ratio.

D. Data Acquisition System

In this experiment, we wish to observe the extremely small infrared emission signal from the molecules on the surface in the presence of the signal from the bulk emission from the substrate, which is larger by a factor of 10^2 to 10^4. In order to observe this small signal, we use a data acquisition system controlled by a minicomputer so that subsequent spectra stored digitally can easily be compared by taking their ratio.

A Digital Equipment Corporation PDP-11/20 minicomputer is used to collect and analyze the data for this experiment. This computer is equipped with a sample and hold amplifier, an analog-to-digital converter with 16 bit accuracy when averaged over 1000 samples, and a programmable clock. It also has facilities for viewing incoming data on a cathode ray tube (CRT) screen and for plotting the data on an x-y recorder, as well as standard interfaces to a terminal and printer. In addition, it has an interface to a Superior Electric Slo-Syn preset indexer for control of a stepping motor. Since this computer has been very heavily used in our laboratory for data acquisition on systems using infrared Fourier transform spectrometers with stepping motors identical to the one used on the grating drive for the cold grating spectrometer in this experiment, it was possible to use much of the existing software developed by William Challener. The existing software consisted of a FORTRAN monitor program which supervises many FORTRAN data analysis subroutines and several assembly language subroutines for data acquisition and the viewing of the data on the CRT. The monitor program and the data acquisition and analysis subroutines were then changed and customized to meet the needs of this experiment.

A block diagram of the data acquisition system is shown in Figure 16. For the purposes of this discussion, the infrared optical system is schematically represented only by the sample, the spectrometer, and the detector. In order to obtain an infrared spectrum of the sample, we wish to measure the signal at the detector as a function of the grating position. The minicomputer is able to control the grating position by sending a signal to the Slo-Syn indexer which then issues a signal to step the stepping motor, turning the grating drive. Each step of the stepping motor consists of a fixed number of jogs which is preset by turning several dials on the front of the Slo-Syn controller box. One jog is the smallest controllable movement of the stepping motor. The grating drive is arranged so that 10,000 jogs of the stepping motor correspond to exactly 90^{o} of grating rotation.

The current through the photoconductive detector is transformed by the transimpedance amplifier circuit, discussed in Section A.2.g above into a voltage which is fed into the input of the sample and hold amplifier and then digitized by the analog to digital converter. The digitized data are then stored in the memory of the minicomputer.

The typical data acquisition sequence is as follows. The grating position is adjusted to the initial desired angle for the desired spectrum, by either turning the grating manually or stepping it under computer control. With the indexer set for the number of jogs per step to give the required number of points per resolution element, the command to measure a fixed number of data points is issued to the computer. For each data point, the computer is usually told to average 1000 samples of 1 msec. each. It issues the appropriate commands to the

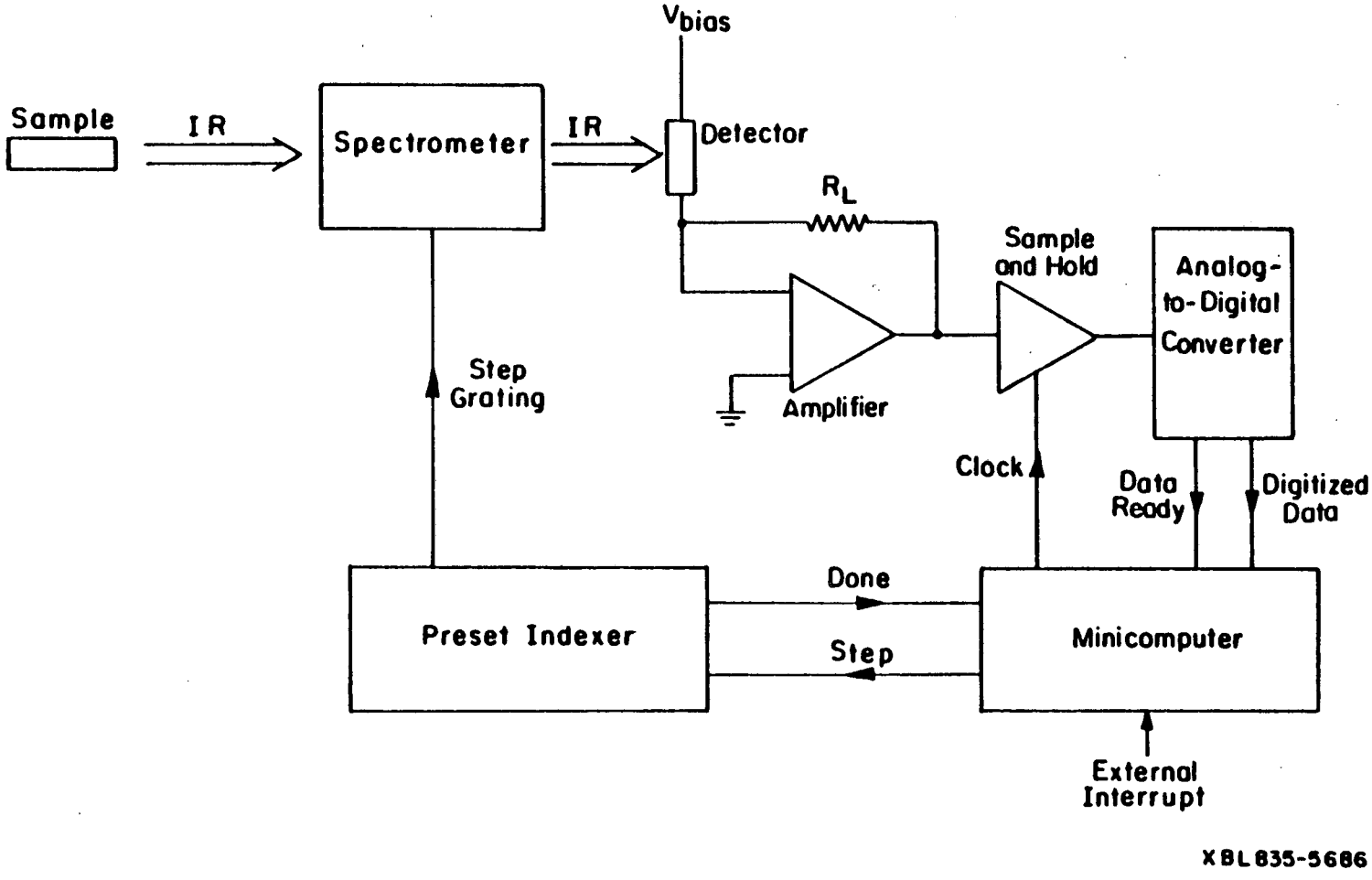

Fig. 16. Block diagram of data acquisition system.

analog-to-digital converter, waiting for the interrupt caused by each conversion. Upon completion of the required number of conversions, the computer then issues a command to step the grating to the Slo-Syn indexer. After waiting for an interrupt caused by the Slo-Syn "Done" signal, it waits an additional 300 msec. for the system to settle down from the vibrations caused by the grating movement. It then repeats this procedure for each data point until it has completed the required number of data points. Finally, at the end of the measurement of the spectrum, the computer causes the grating drive to rewind, including an additional 3^{o} of rewind in order to remove the backlash from the grating drive system, and finally turning the grating back in the forward direction to leave it at its initial starting position for the beginning of another spectrum.

In practice, we first measure the reference spectrum of a clean sample. Then we measure the spectrum of a sample which has been dosed with molecules. We then measure the difference of these two spectra and scale it by a factor of 256. Then we divide this scaled difference by the original reference spectrum to remove systematic effects caused by variations in the blackbody curve and optical efficiency. The resulting spectrum gives the emissivity of the molecules alone. It corresponds to taking the ratio of the spectrum of the sample with molecules to the reference spectrum of a clean sample and subtracting a constant. The computations, however, are performed in the order described above so as not to exceed the 16 bit integer arithmetic of our minicomputer.

The data acquisition software is also capable of running the system as a type of slow digital lock-in amplifier. The command to the

computer can cause it to measure n data points, where $n \geq 1$, between each step of the grating. It can have the computer wait for an external interrupt before the measurement of each data point. Thus, a possible way to run the system in this mode could be to have a very slow chopper cause an external interrupt each time it changed something in the optical path. If it did this twice per cycle, the computer can be asked to measure two data points between each step of the grating. These data points could then later be compared digitally to give the comparison of the signal with the two different chopper states. This mode of operation would thus, in effect, be a digital lock-in amplifier.

IV. SYSTEM PERFORMANCE

We are particularly interested in using our infrared emission apparatus to measure the linewidths of low frequency adsorbate-substrate modes, which have signals at least one to two orders of magnitude weaker than the signal from the C=O stretching vibration of CO. Since we want to observe such small signals, we must investigate the sources of noise which limit the sensitivity of the instrument. This chapter presents a quantitative analysis of the present performance and limitations of our apparatus, together with some suggestions for improving its sensitivity. First we discuss the calibration of the spectrometer frequency scale and the spectrometer resolution. We compare the measured efficiency and noise of our spectrometer with the predicted values. Because modulation has not yet been implemented, the sensitivity of the instrument is currently limited by long term instabilities in the optics and electronics, rather than by photon noise. With the addition of modulation, the apparatus should be capable of photon noise limited performance in which its principal noise source would be the fluctuations in the incoming photon stream.

A. Calibration of Spectrometer Frequency

The calibration of the spectrometer frequency scale is performed by sending a visible helium-neon laser beam, with a wavelength of 6328 Å, through the spectrometer. The characteristics of the grating drive give the change in angle of the grating with the number of steps of the motor. Thus, the angular differences between the observed laser lines of different orders are easily measured. Using the method described

below, the measurement of at least two laser lines in a spectrum allows an absolute calibration of the angles for these two laser lines.

For the calibration measurement, the laser enters the ultrahigh vacuum system through the large window in the front. With the sample turned at an angle of about 45^{o}, the laser can be positioned to reflect light from the front surface of the sample into the entrance slit of the spectrometer. The filter wheel is turned so that the empty hole in the wheel is behind the entrance slit, allowing visible light to pass into the spectrometer. The detector is then able to see sharp laser lines of many orders as the diffraction grating is turned.

Using the grating equation, we obtain for two different orders of laser light the following two equations:

$$\lambda_1 = n_1\lambda = 2d \sin \theta_1 \cos\phi \tag{37}$$

$$\lambda_2 = n_2\lambda = 2d \sin \theta_2 \cos\phi \tag{38}$$

Here λ is the wavelength of the light, n_1 and n_2 are the two different orders of light which we can obtain by counting the number of lines from zero order, ϕ is one half of the angle between the incident and diffracted beams of light at the grating, and θ_1 and θ_2 are the unknown angles. We thus have two equations in three unknowns, ϕ, θ_1, and θ_2. We obtain a third equation by measuring χ, the difference in angle between the two laser lines.

$$\chi = \theta_1 - \theta_2 \tag{39}$$

These three equations can easily be solved to give $\tan \theta_2$, $\cos \phi$, and θ_1.

$$\tan \theta_2 = \frac{\lambda_2 \sin \chi}{\lambda_1 - \lambda_2 \cos \chi} \tag{40}$$

$$\cos \phi = \frac{\lambda_2}{2d \sin \theta_2} \tag{41}$$

$$\theta_1 = \chi + \theta_2 \tag{42}$$

Using this calibration method for several different pairs of laser lines, we obtain $\cos\phi = 0.938$ and $\phi = 20.3^{\circ}$. We also obtain the absolute angles of the grating for the observed laser lines. Such a calibration spectrum is measured at least once during each run of the spectrometer to be sure that the frequencies of the adsorbate lines are accurately determined.

B. Spectrometer Resolution

The angular resolution of the instrument was measured by taking a spectrum of the zero order diffracted peak from the grating and measuring its width. Such a spectrum is shown in Figure 17. The angular full width at half maximum of this peak is 0.30°. This corresponds well with the design figure of 0.31° derived in Chapter II.

This measurement of the angular resolution of the spectrometer is reconfirmed by measuring the width of a line from the helium-neon laser, as described in the previous section. The full width at half maximum of the seventh order line is 0.26°, which corresponds well with both the width of the zero order peak and the theoretical estimate of the angular resolution.

We can calculate the spectral resolution of the spectrometer from Eq. (15) in Chapter II.

$$\frac{d\nu}{\nu} = \frac{d\theta}{\tan \theta} \tag{15}$$

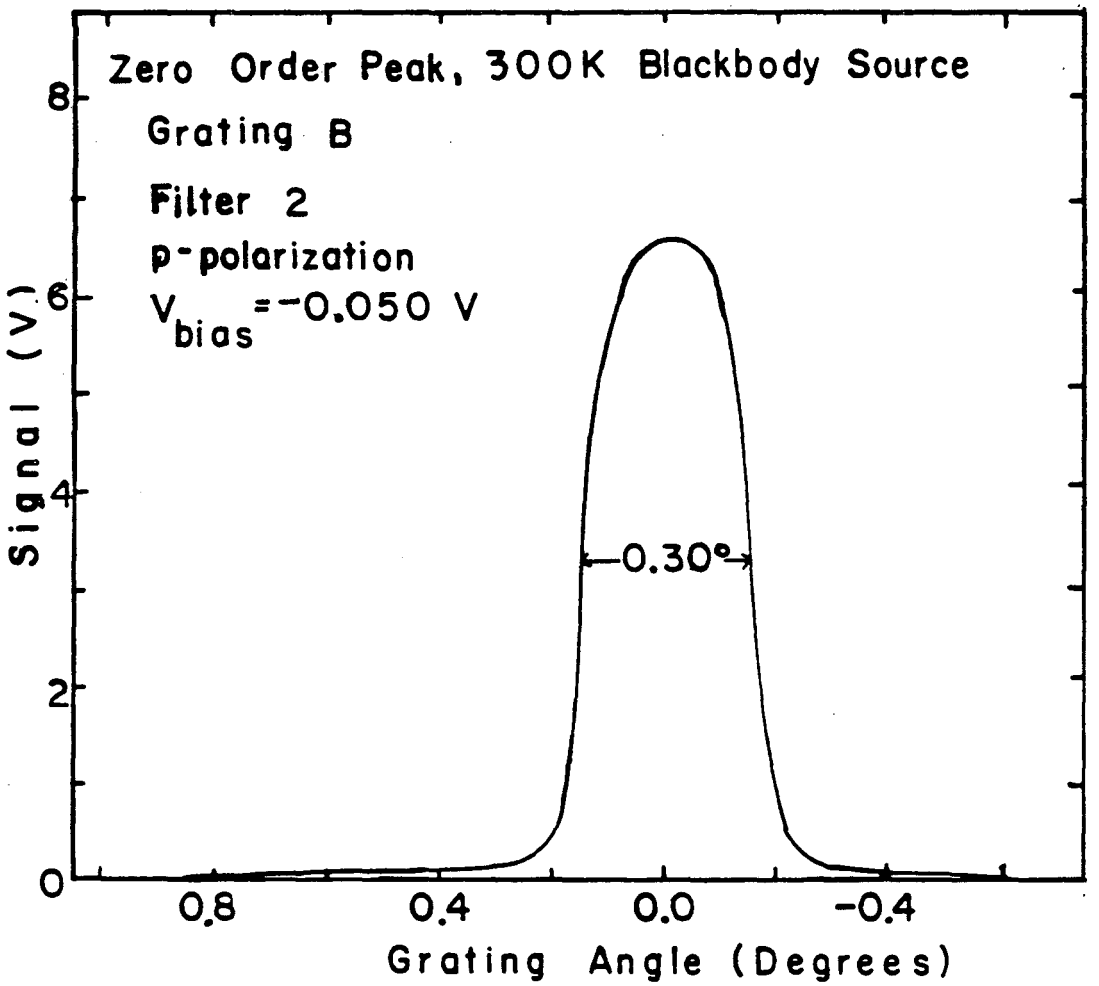

Fig. 17. Observed zero order peak from spectrum measured with cold grating spectrometer.

We can express $\tan\theta$ in terms of ν by using the grating equation. Thus we obtain for the resolution of the spectrometer

$$d\nu = \nu\, d\theta \Big/ \sqrt{\nu^2 \left(2d \cos\phi \right)^2 - 1} \qquad (43)$$

Using the measured values of $d = 0.30^0$ and $\cos\phi = 0.938$, we plot in Figure 18 the resolution of the spectrometer as a function of frequency from Eq. (43). We see that the spectrometer resolution is 1 to 20 cm^{-1} over the spectral range from 330 to 3000 cm^{-1}. At the 2000 cm^{-1} frequency of the carbon-oxygen stretching vibration of adsorbed CO, the resolution is either 7 or 20 cm^{-1} depending on which grating we use. At the lower frequency of the carbon-nickel stretching vibration at 470 cm^{-1}, the resolution of the instrument is 2.5 cm^{-1}.

C. Detector Calibration

An understanding of the properties of the photoconductive detector is necessary in order to compute how the measured signal compares with the predicted signal. We need to know the detector's response as a function of optical frequency, as well as the constants which determine the current through the detector when a flux of photons is incident upon it. Although we have used both Si:As and Si:Sb detectors in the cooled spectrometer, the present detector circuit has a Si:Sb detector with a cold JFET preamplifier stage, as was described in Chapter III. This detector system was built and calibrated by Roger Tobin.

The relative spectral responsivity of each detector was measured from 50 to 650 cm^{-1} by immersing it in liquid helium at the end of a light pipe connected to a room temperature Fourier transform spectrometer. The spectrometer output was normalized by computing its

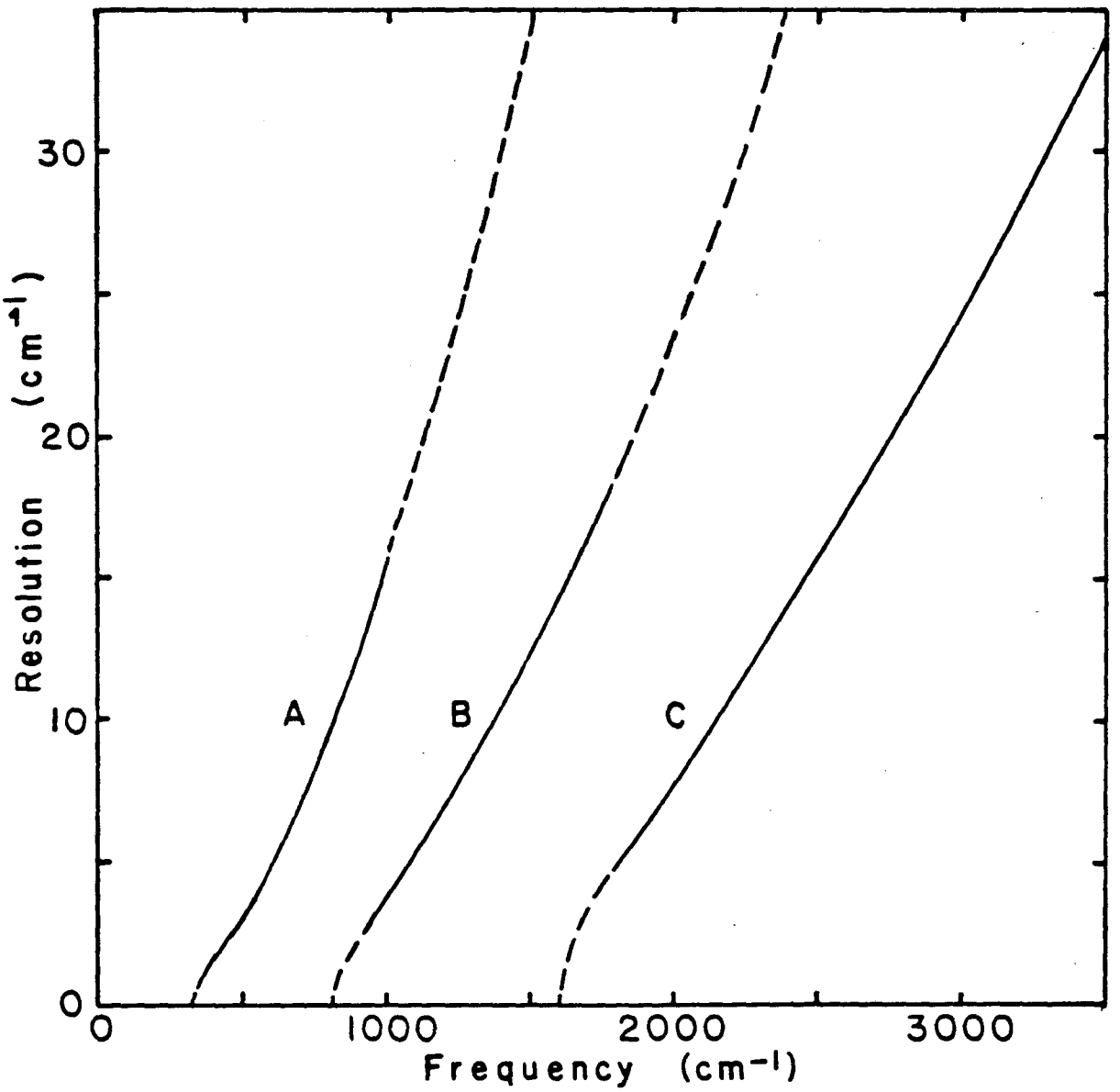

Fig. 18. Resolution of the spectrometer for Gratings A, B, and C as a function of the frequency. The solid lines indicate the suggested ranges of use of each grating.

ratio to the output of a Golay cell. This measurement was performed in a much higher background flux than that which is incident on the detector in the liquid helium cooled grating spectrometer. The spectral responsivity, in arbitrary units, is shown in Figure 19 for both the Si:As and Si:Sb detectors. The low frequency cutoff is 425 cm^{-1} for the As doped detector and 330 cm^{-1} for the Sb doped detector. The Sb doped detector was installed into the spectrometer because we were particularly interested in extending the system response to lower frequencies.

The Si:Sb detector was calibrated in a liquid helium temperature black-walled box with an internal blackbody source.[43] From those measurements, we extrapolate the values for the photoconductive gain, G, and the quantum efficiency, η, at 2000 cm^{-1}, for a chopping frequency of 10 Hz and a bias voltage of -3.0 V. We obtain G=0.84 and η=0.33 for these conditions. Recall from Eq. (36) of Chapter III that the current through the detector is directly proportional to the number of photons per second incident upon it, with ηG and the electronic charge as proportionality constants.

$$I=eG\eta N \tag{36}$$

Figure 20 shows the measured current versus voltage (I-V) characteristic of the Si:Sb detector in the liquid helium cooled grating spectrometer. This curve gives the dc response of the detector as a function of the bias voltage. The measurements were performed at an optical frequency of 1000 cm^{-1} using illumination from a room temperature blackbody source. Note that, for bias voltages between 20 mV and 200 mV, the current, I, is directly proportional to the voltage,

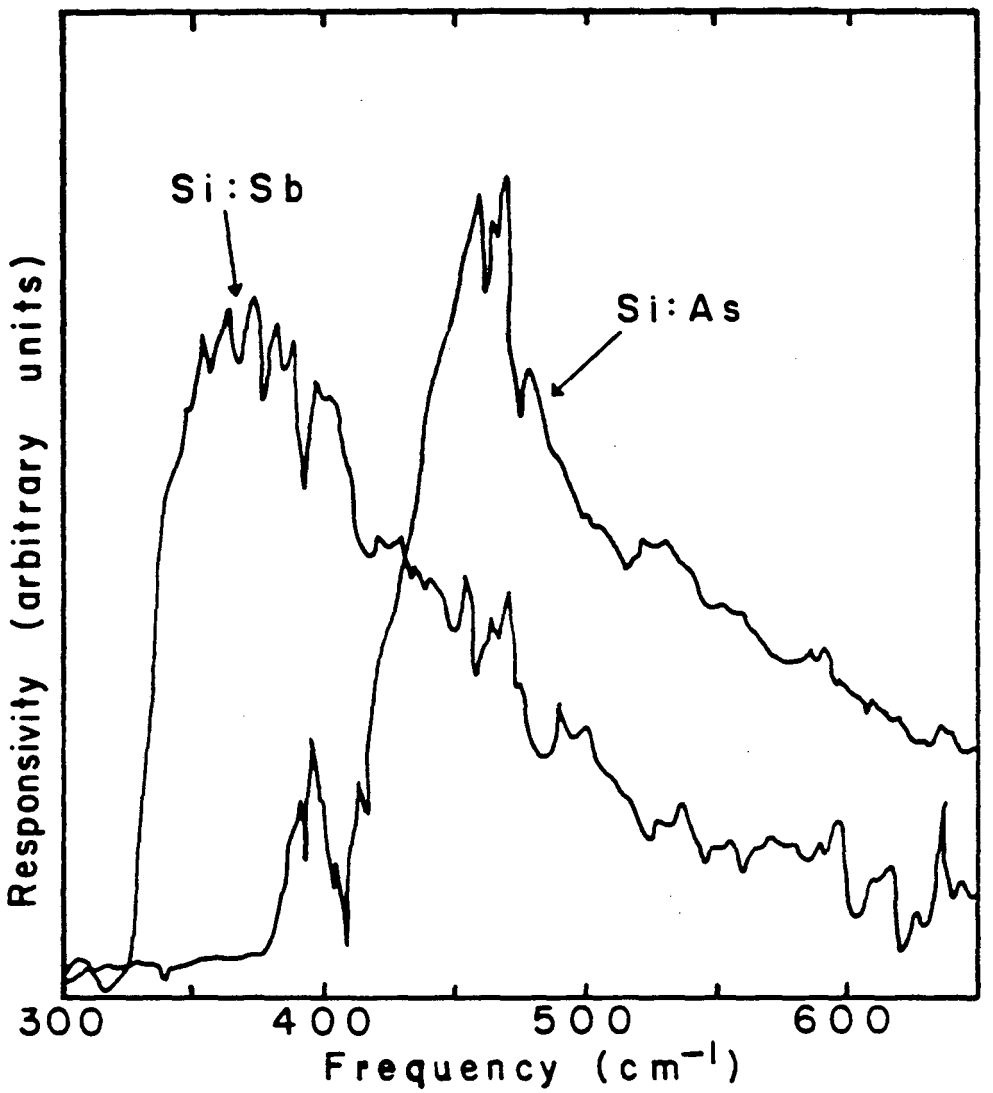

Fig. 19. Measured detector responsivity, in arbitrary units, as a function of frequency for Si:Sb and Si:As photoconductive detectors.

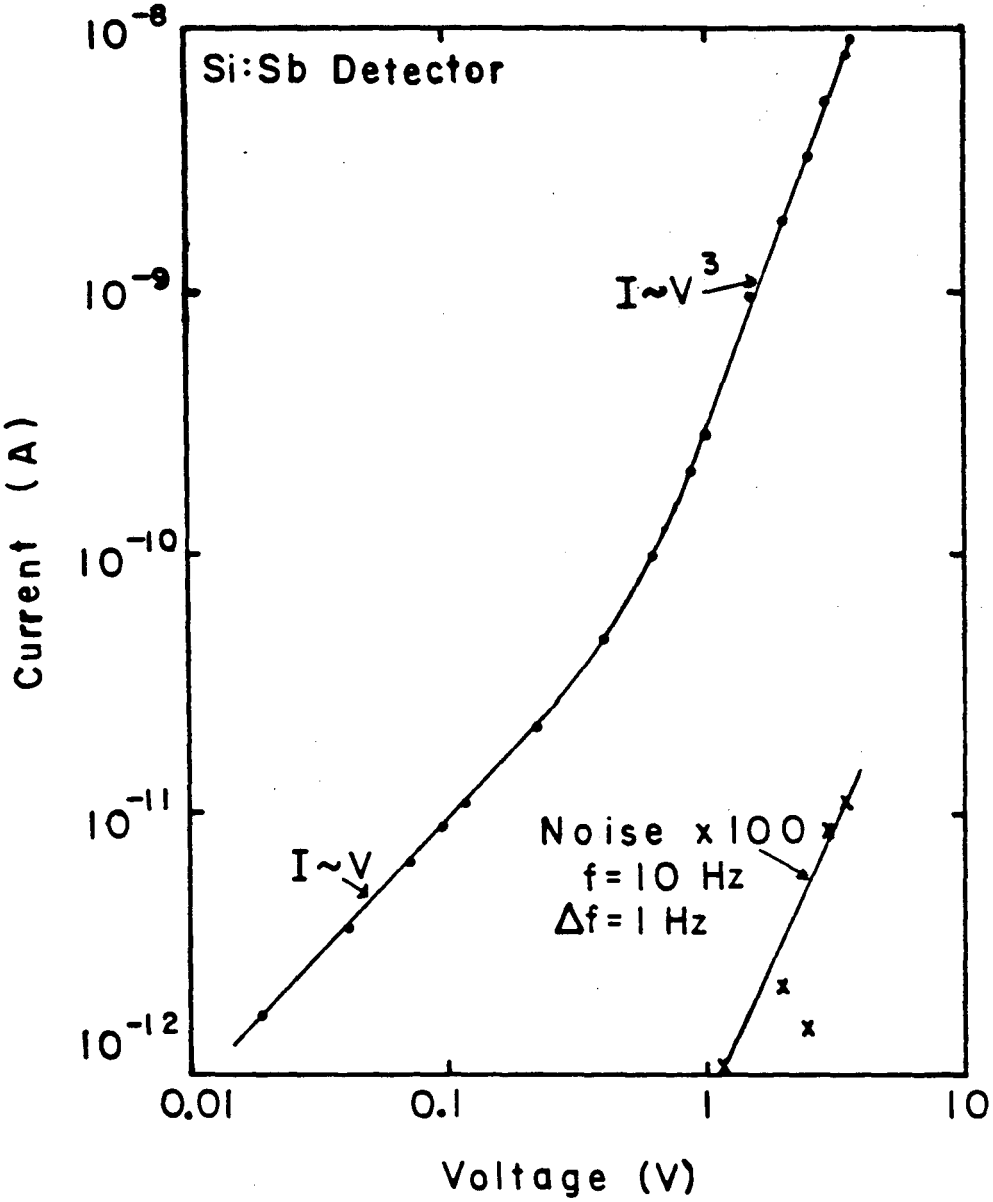

Fig. 20. Current versus voltage characteristic of Si:Sb detector in spectrometer.

V. For bias voltages between 0.9 V and 4.0 V, however, I is proportional to V^3. The noise, on the other hand, increases more slowly with the voltage until large current spikes in the detector occur at a bias voltage of about 4 V.[44] Thus, the optimum signal to noise ratio is obtained by raising the bias as high as possible without exceeding the threshold voltage of 4 V for the spiking noise.

D. Spectrometer Efficiency

We define the spectrometer efficiency, E, as the ratio of the measured number of photons per second at the detector to the predicted number from the source accepted by the throughput of the spectrometer. This efficiency is expected to be considerably less than unity due to the transmission and reflection losses of various optical elements.

We can estimate these losses from our knowledge of the characteristics of the optical elements in the system. We expect E to be a product of these factors.

$$E = p\ w\ f\ r\ g\ a \tag{44}$$

Here p is the polarizer transmittance, w is the window transmittance, f is the filter transmittance, r is the product of the reflectances of the three mirrors inside the spectrometer, g is the grating efficiency, and a is the factor due to errors in optical alignment. Except for a, these values can be easily estimated at a frequency of 2000 cm^{-1}, as is shown below.

p = (0.5 for polarization) x (0.7 for AgBr transmittance)

= 0.35

w = 0.7 for KRS-5 transmittance

f = 0.8 for Filter 2 transmittance at 2000 cm^{-1}

$r = (0.98)^3$ for product of reflectances of three mirrors

$= 0.94$

$g = 0.52$, extrapolating from Bausch and Lomb's specifications for Grating B

So, if the optical alignment were perfect, E would be the product of these five factors, which is 0.10.

From our measured signal of 0.5 V at 2000 cm^{-1}, from a room temperature blackbody source at a bias voltage of -1.25 V, we can now calculate the measured efficiency of the spectrometer. We measured only the p-polarized light. The cold load resistor had a resistance, R_L, of 5.9×10^{10} Ohms. Using the values of G and described above, we can easily calculate the experimental number of photons per second at the detector. Since the current through the detector is proportional to V^3, and our knowledge of the detector parameters G and η is at a bias volage of -3.00 V, we will first scale the signal by $(3/1.25)^3$, obtaining an effective voltage signal of 6.91 V. Then we substitute this value into the following equation:

$$N_{exp} = \frac{I}{eG\eta} = \frac{V_{sig}}{R_L eG\eta} \qquad (45)$$

$$= 2.6 \times 10^9 \text{ photons/sec}$$

Because of the polarization effects of the diffraction grating, this is about 1/3 of the signal expected with unpolarized light.

$$N_{exp\ unpol} = 7.8 \times 10^9 \text{ photons/sec} \qquad (46)$$

We now compare this value with our theoretical number from Table 2 in Chapter II, which assumed that the spectrometer efficiency was 0.10 and that the substrate emissivity was 0.25. Since our source for this

efficiency measurement is a room temperature blackbody, we need to multiply the number in the table by a factor of 4. But, in fact, we currently have an entrance slit at the front of the detector cavity which is 0.5 mm wide and 1 mm long, which is a factor of four smaller than the area of the detector assumed in the calculation. So these two factors of four cancel, and we obtain

$$N_{theor} = 2.35 \times 10^{10} \text{ photons/sec} \tag{47}$$

Thus we obtain an measured spectrometer efficiency of

$$E = \frac{N_{exp}}{N_{theor}} \times 0.10 = 3.3\ \% \tag{48}$$

Therefore, the loss of signal due to optical misalignment is about 67 %.

E. Calculated Noise

We can calculate the expected noise in the system from two major sources: (1) The amplifier noise in the detector circuit. (2) The photon noise in the system. These calculations will then be compared in the following section with the measured noise in the system.

1. Amplifier Noise

We can model the detector circuit by the equivalent noise circuit shown in Figure 21.[41] In this model, e_n and i_n are the equivalent voltage and current noise sources for the JFET preamplifier, respectively. R_D is the detector resistance with capacitance C_D from the gate of the JFET to ground, while R_L is the load resistor with its capacitance C_L. The equivalent Johnson noise current sources for the detector and load resistances are i_D and i_L, respectively. We will assume that all of these noise sources are uncorrelated.

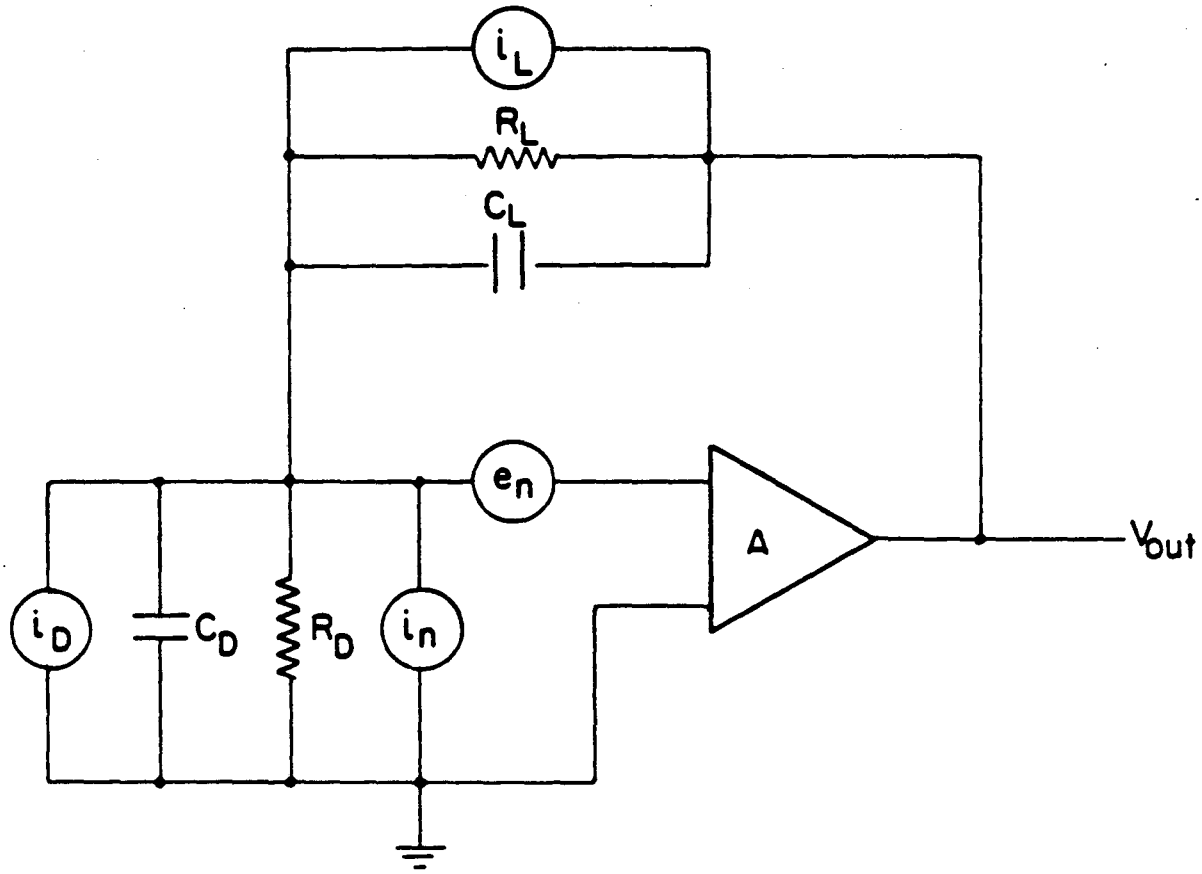

Fig. 21. Equivalent noise circuit for transimpedance amplifier. After Ref. 41.

We need to find the contribution to the noise at the output of the circuit from each of these noise sources. Here Z_L is the complex impedance of the load resistor and its associated capacitance.

$$Z_L = \frac{R_L}{1 + i\omega R_L C_L} \tag{49}$$

Similarly, Z_D is the complex impedance of the detector and the capacitance at the gate of the JFET.

$$Z_D = \frac{R_D}{1 + i\omega R_D C_D} \tag{50}$$

The voltage at the output, V_v, due to the voltage noise source e_n can then be expressed as

$$V_v = -e_n\,(1 + Z_L/Z_D) \tag{51}$$

Expressed in terms of the resistances and capacitances for computational purposes, the quantity in parentheses is

$$(1 + Z_L/Z_D) = \frac{R_D + R_L + i\omega R_D R_L\,(C_D + C_L)}{R_D\,(1 + i\omega R_L C_L)} \tag{52}$$

Noise from each current source simply flows through the load impedance to appear as an output voltage. For example,

$$V_I = i_n\, Z_L \tag{53}$$

The Johnson noise currents, in bandwidth Δf, from the detector and load resistances are easily expressed as

$$i_D = \sqrt{4kT\Delta f/R_D} \tag{54}$$

and

$$i_L = \sqrt{4kT\Delta f/R_L}\ . \tag{55}$$

Now we can insert some numbers into these formulas and see what they predict for the contributions from the various noise sources. We assume a modulation frequency of 10 Hz. The computation will be done in the extremely low background limit where the entrance slit to the

spectrometer is blocked by aluminum foil at liquid helium temperature. The low temperature resistance of the load resistor was measured to be $3 \times 10^9 \Omega$ by immersing it in liquid helium before it was installed in the detector circuit. The ratio of the detector resistance to that of the load resistor is easily measured from the signal and bias voltages of the detector circuit.

$$R_D = R_L \, V_{bias}/V_{signal} \tag{56}$$

In very low background flux, we obtain $R_D = 4.5 \times 10^{13} \Omega$. The capacitance C_D is equal to the sum of the detector's capacitance due to its geometry, which is calculated as 3.5 pF, and the 12 pF gate capacitance of the J230 JFET obtained from its specification sheet. Finally, we estimate C_L as 0.5 pF from measurements of the voltage gain of the circuit as a function of modulation frequency, where

$$\text{Gain} = Z_L/Z_D \tag{57}$$

The measured noise voltage of the pair of JFETs is 20 $nV/Hz^{1/2}$ at 10 Hz. Since $\omega R_L C_L << 1$, and $R_D >> R_L$, (10) simplifies to

$$(1 + Z_L/Z_D) = 1 + i\omega R_L (C_D + C_L) \tag{58}$$

$$= 1 + 3\,i.$$

Therefore, $|V_v| = 0.06 \, \mu V/Hz^{1/2}$. (59)

At the spectrometer temperature of 5K, the Johnson noise currents from the detector and load resistor are

$$i_D = 2.47 \times 10^{-18} \text{ A/Hz}^{1/2} \tag{60}$$

and

$$i_L = 3.03 \times 10^{-16} \text{ A/Hz}^{1/2}. \tag{61}$$

Although the current noise from the JFETs is too small to measure easily, an upper limit on it is 5×10^{-17} $A/Hz^{1/2}$. Since these three current sources are uncorrelated, the total noise current from them will

add in quadrature. Clearly i_L, the contribution from the Johnson noise of the load resistor will dominate. The noise voltage from this source is

$$V_J = i_L Z_L = i_L R_L = 0.91 \ \mu V/Hz^{1/2}. \quad (62)$$

The total noise voltage from the amplifier is then expected to be

$$V_{amp} = (V_J^2 + V_v^2)^{1/2} \quad (63)$$
$$= 0.91 \ \mu V/Hz^{1/2}.$$

Note that this value should be independent of the flux on the detector.

2. Photon Noise

We can also calculate the expected photon noise for the background limited behavior of the detector. For $hc\bar{\nu}/kT>>1$, the fluctuations in the current due to the photon noise are given by the equation:[45]

$$\Delta I = 2eG\sqrt{N\eta} \quad (64)$$

Substituting for N from Eq. (36), we can easily find ΔI as a function of I.

$$\Delta I = 2\sqrt{eGI} \quad (65)$$

Since $V_{signal} = I R_L$, (66)

Eq. (65) can be expressed in terms of voltages as

$$\Delta V = 2\sqrt{eGR_L V_{signal}}. \quad (67)$$

Alternatively, we can express ΔN as a function of N as

$$\Delta N = 2\sqrt{N/\eta} \quad (68)$$

On a log-log plot of ΔV versus V or ΔN versus N, these equations give a straight line with slope 1/2.

F. Measured Noise

We have measured the noise in the spectrometer using the Si:Sb

detector and associated circuitry as a function of the background flux for an optical frequency of 2000 cm^{-1} and a modulation frequency of 10 Hz. This measurement, shown in Figure 22, was performed by first exposing the spectrometer to room temperature radiation and then successively reducing the flux on the detector by rotating the cold filter wheel to block part of the beam. The noise was measured as a function of the detector signal as the background flux was reduced. This detector signal was then converted, using Eq. (36) and the calibrated detector parameters, to an equivalent number of photons/sec at the detector for the abscissa of the plot. The ordinate of the plot is given both in terms of a noise voltage and in terms of a noise equivalent photon rate (NEN).

From this figure, we see that at high background flux, such as that on the right side of Figure 22, the noise is proportional to the square root of the flux, which dependence is expected for photon noise. The straight line on the right side is the theoretical calculation of the photon noise from Eq. (68), using the calibrated parameters of the detector. Clearly, this line fits the data very well.

At low background flux, such as that on the left side of Figure 22, the noise does not depend on the flux, as indicated by the straight horizontal line through the data points. This behavior is expected from amplifier noise. The measured noise voltage at low background is $\sim 4.5 \mu V/Hz^{1/2}$. Unfortunately, this measured value is about a factor of 5 higher than expected from our calculations above. Either the current noise of the JFETs is larger than we estimated above, or there is another source of excess noise in the detector circuit.

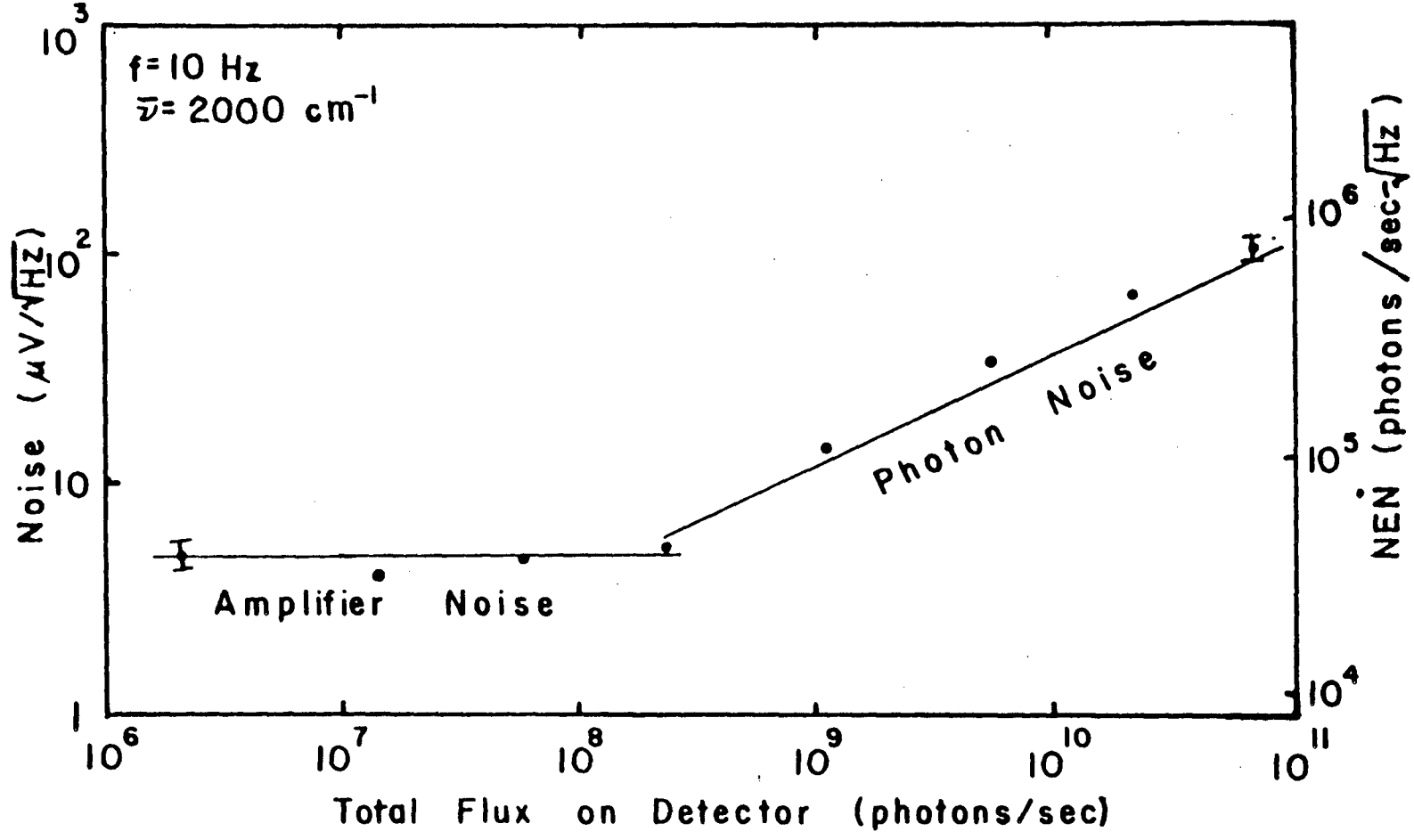

Fig. 22. Measured noise as a function of background flux on Si:Sb detector in cold spectrometer. The line on the right is a theoretical estimate of the photon noise using the measured parameters of the detector. The line on the left is a horizontal line, characteristic of amplifier noise, drawn through the data points.

G. Capabilities of the Instrument

We showed above that with high background flux incident on the detector, the system is capable of photon noise limited performance. Since it is not possible to escape this source of noise, this would be ideal performance. With our measured spectrometer efficiency of ~3%, the photon noise limited performance would permit the measurement of emission from the C=O stretching mode at a coverage of 0.01 monolayer, with a signal to noise ratio of unity in a one Hz bandwidth. Unfortunately, since modulation has not yet been implemented, our measurements of the emission spectra of CO adsorbed on nickel do not show such small amounts of noise. At the present time, the system is limited by instabilities in the source and apparatus. Even without further development, however, we can routinely measure emission from 0.05L CO on Ni, with a line center signal to noise ratio of 4 in a bandwidth of 1/2 Hz.

The fact that our system is remarkably stable permits us to measure adsorbed species even though we are measuring spectra at nearly zero audio frequency. Figure 23a shows an audio frequency noise spectrum for frequencies less than 1 Hz which was measured by sampling in time with a minicomputer and then performing a Fourier transform. We see that the noise spectrum is quite flat down to frequencies less than 0.1 Hz. Figure 23b shows a noise spectrum for frequencies up to 50 Hz. We see that a peak at 60 Hz from ac pickup is aliased back to 40 Hz in the noise spectrum. The system is also subject to some microphonic noise at 20, 25, and 30 Hz. Because of the very high impedances at the gate of

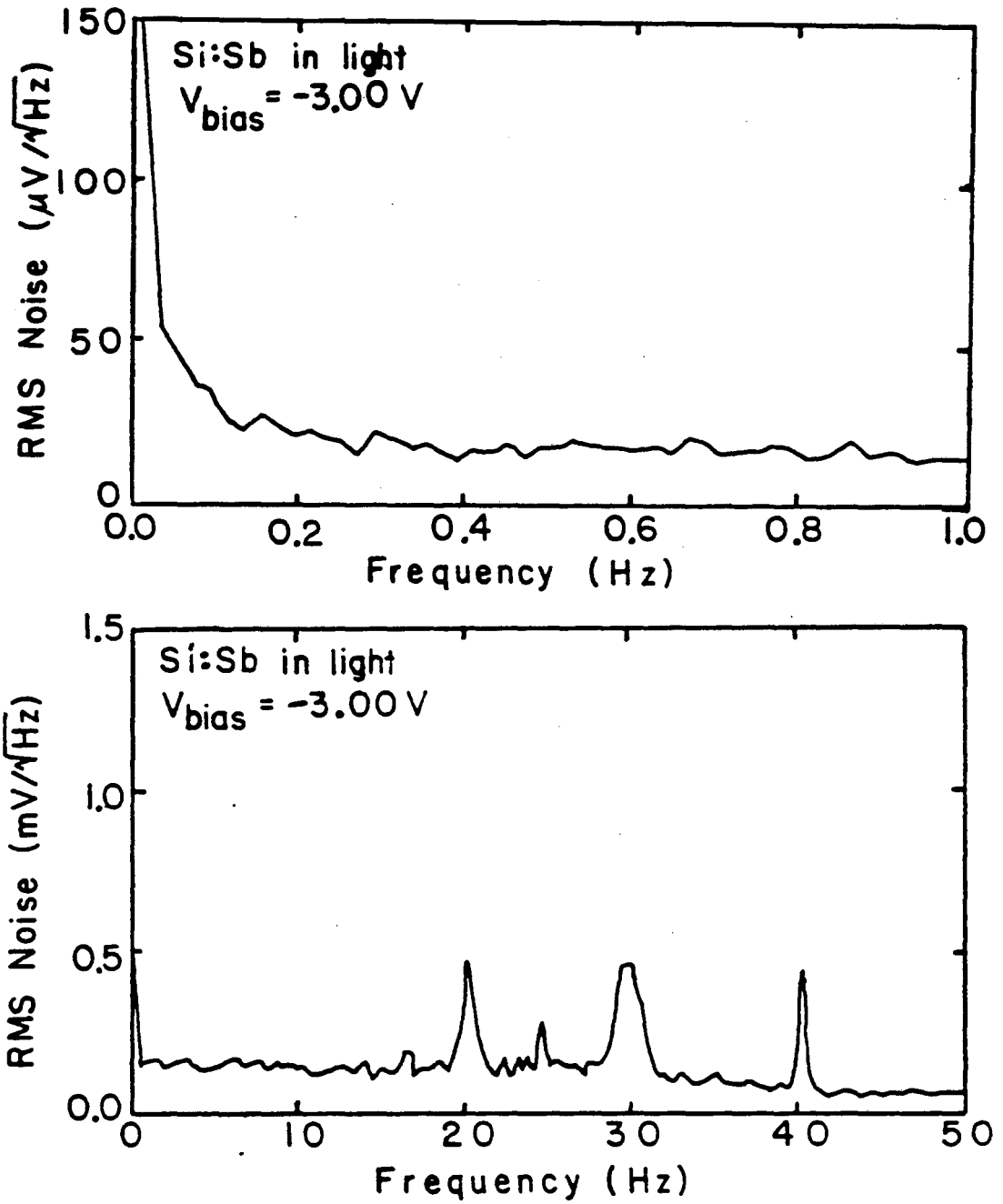

Fig. 23. Measured acoustic noise spectra of Si:Sb detector in cold spectrometer.

the JFET, special care was taken to make the connections there rigid enough to prevent them from vibrating and causing large amounts of microphonic noise. Nevertheless, if we tap on the outside of the dewar, we can cause large noise spikes on the signal. This type of noise, however, is generally at a discrete set of frequencies greater than zero and so has little effect on the dc signal. It also damps out in less than 1/3 second. Since the stepping of the motor which turns the grating causes such microphonic noise, the computer is programmed to wait for 300 msec after stepping the motor before measuring the signal.

For photon noise limited performance, Roger Tobin has calculated the detection threshold of the instrument for small molecular signals on top of the bulk emission of the metal, shown in Figure 24. As a function of the optical frequency, the plot indicates the minimum fractional surface signal ratio which could be measured by the instrument. This detection threshold is just the noise to signal ratio, which may be expressed as the fluctuation in the number of photons/sec, ΔN, divided by the number of photons/sec, N, incident upon the detector. These two quantities, ΔN and N, were each calculated in Chapter II. The calculation which led to Figure 24, however, assumed a sample emissivity of 0.10 for a platinum sample and included factors for the variation of the detector quantum efficiency, η, and the spectrometer resolution as a function of the infrared frequency.

The present detection threshold of the system is shown by the dashed line in Figure 24. Also shown are the observed surface signals from the C=O and C-Ni vibrations of CO on Ni(100) which were observed in the experiments described in Chapter V of this thesis. While it is easy

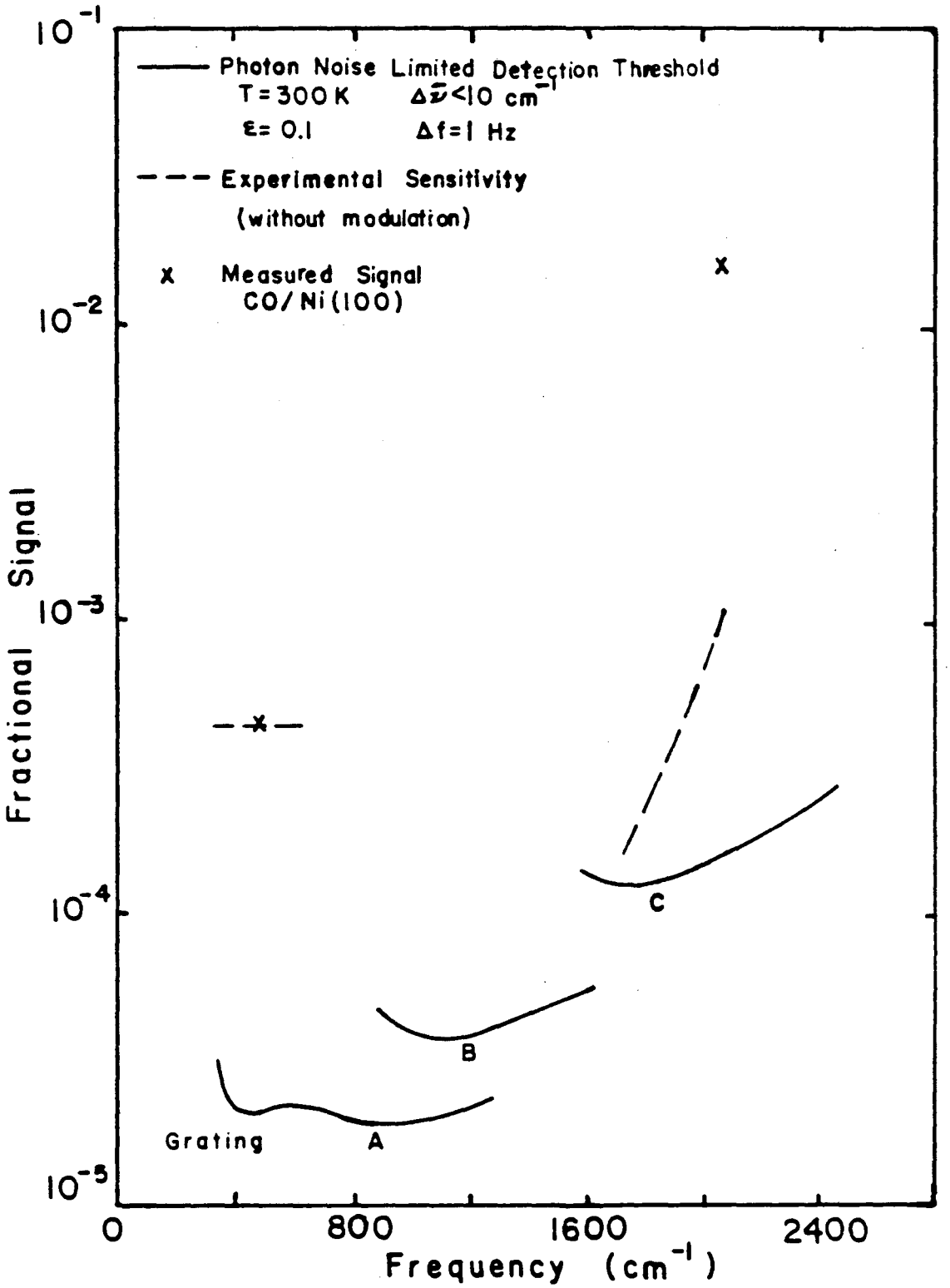

Fig. 24. The solid curves show the calculated detection threshold for an emission apparatus limited by photon noise. The dashed lines show our current experimental sensitivity without modulation. The x's show our measured surface signal from CO on Ni(100).

to observe the C=O stretching vibration with the present sensitivity of the system, the size of the signal from the C-Ni mode is the smallest which can be seen with the instrument without further improvements.

H. Sources of DC Signal Drift

Since we do not yet have a chopper installed in the system, the noise is currently limited by dc drifts. These drifts may have several possible sources. The dc signal has been measured to drift slowly downwards by about 10% over the first five hours after the first liquid helium transfer. After that time, it is stable to <0.1%. Since we see such effects even when the detector is replaced in the circuit by a cold resistor, we take this measurement to be evidence for gain fluctuations in the amplifier circuit, which are probably due to temperature drifts of the load resistor. The dc signal has also been observed to change rapidly by about 1% when either the liquid nitrogen can in the cryostat or the liquid nitrogen can in the ultrahigh vacuum system is refilled, taking about 1/2 hour to stabilize again. In addition, the signal rises about 1% over 5 minutes when the liquid nitrogen in the reservoir in the UHV system has completely evaporated.

A drift in temperature of the LN_2 temperature blackbody has a direct effect on the signal. Since the blackbody is reflected from the sample into the entrance slit of the spectrometer and is thus always in the field of view, the detector will see directly any changes in signal due to a change in the temperature of the blackbody. Small changes in temperature of the blackbody occur as the level of liquid nitrogen in the reservoir decreases. Measurements of the blackbody temperature using a chromel-alumel thermocouple indicate that the temperature

increases by about 5K over the two hour hold time of the reservoir, probably due to inefficient heat sinking of the blackbody and baffles to the bath as the level of liquid decreases. Variations in temperature of the cold baffles, both in the UHV system and in the cryostat, can cause similar effects. As mentioned above, the signal rises very rapidly when the liquid nitrogen in the UHV reservoir has evaporated. This indicates that the temperature stability of the blackbody and baffles is extremely important to the stability of the total signal. The lack of such stability is probably a major source of noise in the experiment at the present time.

A drift in the sample temperature clearly leads to a change in the signal. The sample temperature is regulated so that the chromel-alumel thermocouple voltage is stable within 2 V. This indicates that the sample temperature may fluctuate as much as 50 mK. We can calculate the effect of the temperature fluctuation on the photon flux. Equation (7) in Chapter II gives N, the number of photons per second at the detector as a function of optical frequency and temperature. Differentiating this equation with respect to temperature, we obtain

$$\frac{dN}{N} = \frac{1}{1 - \exp(-h\nu/kT)} \frac{h\nu}{kT^2} dT \qquad (69)$$

For a 300K source, at 2000 cm^{-1}, we find $dN/N = 1.5 \times 10^{-3}$. We obtain $dN/N = 4.2 \times 10^{-4}$ at 500 cm^{-1}. Note, however, that these values are integrated over all frequencies. These values are within a factor two of the observed noise to signal ratios, which were displayed in Figure 24 at those two infrared frequencies. Nevertheless, at the present time, we believe that other drifts in the system, particularly the drift

due to a temperature change of the baffles and blackbody, are larger than those caused by the instability of the sample temperature.

Another possible source of dc drift is a variation in the temperature of the KRS-5 lens. Although the lens transmits only 70% of the radiation incident upon it, almost all of the loss is from reflection at the front and back faces because of its high index of refraction of 2.4 at infrared frequencies. Since the lens has very low emissivity, we are able to obtain reasonable data without cooling the lens. Note that the lens itself is not imaged on the entrance slit. However, after first filling the LN_2 reservoir in the UHV system, the signal is not stable enough to obtain a flat ratio of two subsequent spectra taken under identical conditions until approximately one hour has passed. It seems likely that the lens radiates to the cold baffles so that it takes some time to come to temperature equilibrium.

Fluctuations in the sample position can also lead to dc noise. Thus if the sample position were changing slightly, this could cause fluctuations in the signal. We have no direct way of measuring the size of this noise source, though we know that it is smaller than the noise caused by temperature fluctuations in the blackbody or baffles as described above.

Another source of dc signal drift may be non-reproducibility of the diffraction grating angle. We are currently relying on the positioning of the helical gears driving the grating table to assure the reproducibility of the grating angle. We have plans to spring load the grating drive to help eliminate this possible source of dc drift.

It is also possible that changes in the room temperature ambient

radiation are affecting our signal. We have tried, however, to prevent stray radiation from reflecting from the lens and entering the spectrometer by careful placement of the cold baffles.

G. Methods of Modulation

It is clear that the noise in the system could be reduced by measuring an ac signal rather than a dc signal, thus making the measured signal less subject to 1/f noise and drifts. In order to decide on the best type of chopper to implement, it is necessary to know which are the principal noise sources in the system and then to design the chopping scheme to eliminate them from the measured signal. These noise sources were discussed in the sections above.

The installation of a chopper into the system is non-trivial because it must involve either ultrahigh vacuum or cryogenic technology, or both. The presence of gain drifts in the amplifier means that, ideally, one would want to chop between a signal which depends on the adsorbed molecules and a signal which does not, with the same total amplitude of signal on the detector in each case. In addition, the chopper should be as close to the sample as possible, so as to modulate only the radiation from the sample and not any other background radiation which may leak into the entrance slit to the spectrometer. Unfortunately, these conditions are not easy to arrange with the necessary stability in the chopper. Since the noise level in this system is already less than 10^{-3} of the total signal on the detector, one needs a very stable chopper so as not to introduce more noise with the chopper by doing an ac measurement than is originally on the signal

in the dc measurement. Although several easily implemented chopping methods have been tried, these methods were not successful in reducing the noise on the measured signal. The rest of this section will discuss the unsuccessful methods of chopping which have been tried, plus several possible methods which have not yet been implemented.

At one time, we tried a method of chopping the signal which consisted of moving the sample in and out of the beam at a frequency of about 1 Hz. A motor, connected mechanically to the outside of the manipulator, moved the sample and sent an external interrupt to the computer twice per cycle. The computer was then able to detect the signal at this frequency using the digital lock-in amplifier program described in Chapter III, Section C. Without turning the diffraction grating, we measured the signal from the sample as the sample was moved in and out of the beam. We discovered that the irreproducibility of the sample position caused ~1% fluctuations in the total signal. Since this method of chopping resulted in more noise on the signal than had our previous dc measurements, we abandoned it. Part of the problem is probably the lack of a beam defining aperture near the sample; the aperture which is attached to the end of the cold baffle is currently considerably oversized. If some type of hard stop were placed inside the UHV system to try to assure the reproducibility of the sample position, it might be possible to make this system work so as to reduce the total noise. In practice, since this would be extremely difficult, a chopping scheme which does not move the sample is preferable.

Since the signal from the adsorbed molecules is polarized, a modulation scheme which varies the polarization of the measured signal

could be ideal. The implementation of this type of modulation, however, involves a number of difficulties. First, the signal from the diffraction grating as a function of grating angle is much different for the polarization parallel to the grooves from that for the polarization perpendicular to the grooves, both in amplitude and slope.[46] We can see this dependence in our observed spectra of a room temperature blackbody for the two different polarizations, shown in Figure 25. Thus, it is important to try to eliminate this dependence from the chopped signal so as to see the polarization-dependent signal from the adsorbed molecules. The easiest way to eliminate the dependence of the signal on the diffraction grating is to install a fixed polarizer between the moving polarizer and the diffraction grating. For an ideal polarizer, the polarization of the optical signal when it reaches the diffraction grating is then always the same.

Since we have a movable polarizer, from Perkin Elmer Co., in the beam between the KRS-5 lens and the entrance slit of the spectrometer, it was easy to try a crude polarization modulation scheme. Our movable polarizer can be rotated back and forth through only 90^{o}, from a position where it passes radiation polarized perpendicular to the sample surface (p-polarized), to a position where it passes radiation polarized parallel to the sample surface (s-polarized). Recall that the signal from the adsorbed molecules is p-polarized. For the modulation test, we replaced the filter wheel by a fixed polarizer with gold lines evaporated on a KRS-5 substrate, made by Cambridge Physical Sciences Laboratory. This fixed polarizer was oriented at 45^{o} with respect to the grating grooves. We then moved the movable polarizer back and forth

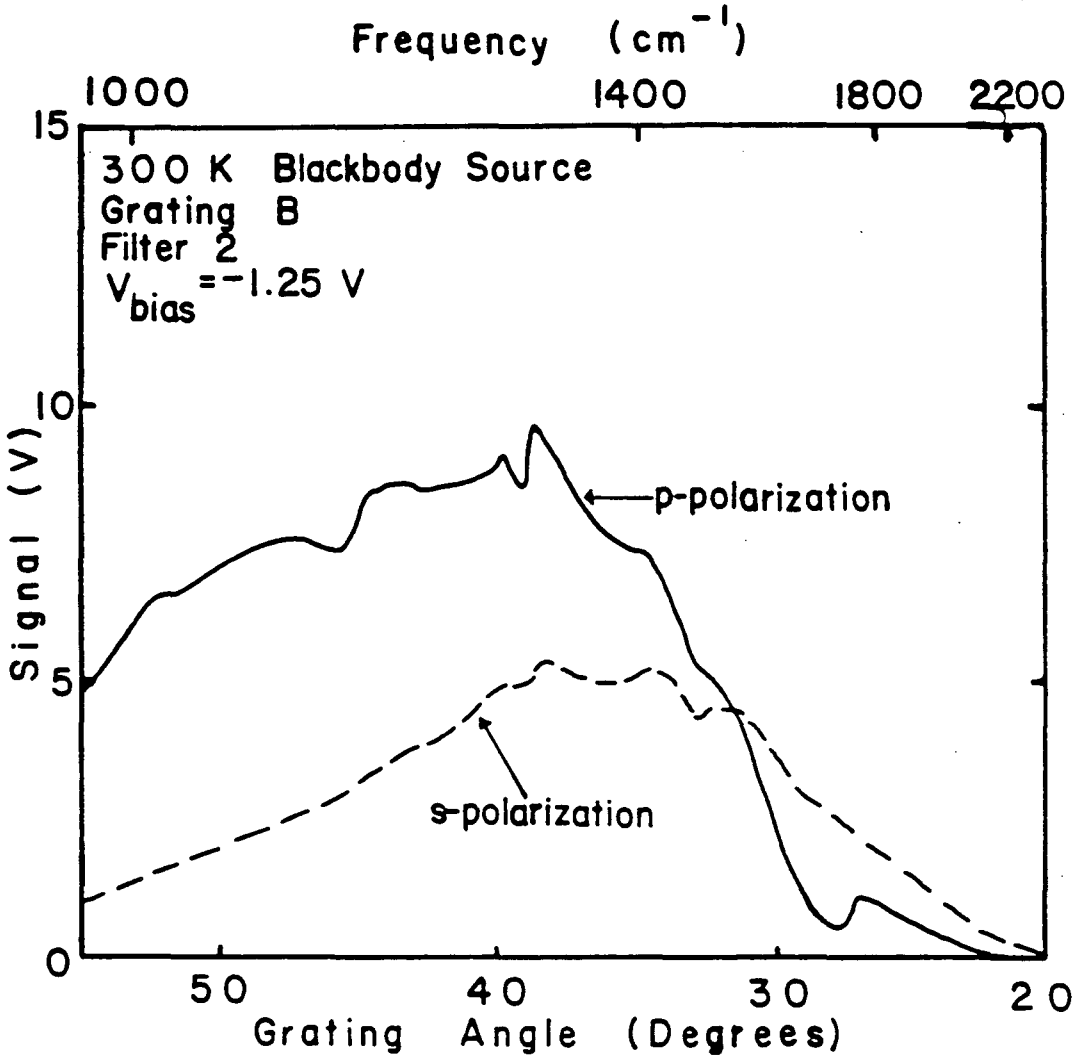

Fig. 25. Observed spectra of 300K blackbody source, measured with cold grating spectrometer. Notice the differences in the spectra for s and p-polarized light.

by hand, sending an external interrupt to the computer each time the polarizer was in position at either extreme angle of its travel. The computer then waited for 1/2 second before measuring a datum. Unfortunately, this method of modulation resulted in more noise on the signal than the dc measurement, apparently because the reproducibility of the polarizer angle is not sufficiently precise, despite the hard stop. Thus, the signal level changes even though the polarizer is replaced in the same nominal position.

Since the reproducibility of the polarizer angle is a problem, clearly a better method of polarization modulation would involve rotating the polarizer continuously through 360^{o}. Such a system has been used by Bradshaw and co-workers in many different experiments, using the reflection-absorption technique.[47] The primary difficulty in implementing this method is that there is very little space in the optical path between the UHV system and the spectrometer, because the system was designed for large throughput. The physical space limitations make it rather difficult to install a motor and assembly to rotate the polarizer continuously. To gain more space, it might be desirable to redesign part of the optical system so as to have a parallel beam between the UHV system and the spectrometer.

Another method of implementing polarization modulation would involve the use of a commercial photoelastic modulator.[48] This type of modulator is used by Overend's group to discriminate between surface and bulk signals.[49] In such a modulator, the application of a voltage to a piezoelectric crystal places strain on a photoelastic crystal, causing the rotation of the polarization of the light. Several difficulties

would arise in the implementation of this method of modulation into our system. First, the space limitation mentioned above would make it extremely difficult to fit a photoelastic modulator into the optical path. Secondly, this type of modulator is able to rotate the polarization of the light by 90^0 only in the range of optical frequencies from 1200 to 20000 cm^{-1}. Since we intend to use our system for lower frequencies to observe adsorbate-substrate vibrations, this is a serious limitation. Finally, the acoustic frequency of operation for this type of modulator is typically 37 kHz, which is much too fast for our detector circuit which rolls off at about 150 Hz. The latter two limitations might be circumvented by using two such modulators in series, both to obtain greater rotation of the polarization and to detect a lower acoustic beat frequency between the two modulators.[48]

Clearly, a mechanical chopper could also be used to modulate the signal. A torsion bar chopper in the ultrahigh vacuum system close to the sample is probably the easiest type of chopper to build and install. Work is currently in progress to build and test such a chopper. When the sample is blocked from the beam, such a chopper would need either to reflect a cold black object into the spectrometer or to be cold and black itself. Alternatively, to reduce the contribution of gain drifts in the amplifier, the reference could be a temperature stabilized object with the same emissivity as the bulk sample. In the latter case, the temperature regulation of the reference object has to be as good as the temperature regulation of the sample itself.

Wavelength modulation is another possibility. This method has been used successfully by Ryberg to observe adsorbates.[50] We tried briefly

to implement this type of modulation by scanning our diffraction grating back and forth quickly over a small region of the spectrum. Unfortunately, there is too much backlash in the present grating drive to permit this to operate successfully.

Another type of modulation might involve chopping between two samples, one clean and one dosed with molecules. This method, however, would involve the cleaning of two identical samples and a careful scheme to dose only one of them with gas molecules. Finally, a suitable method of imaging each sample alternately onto the entrance slit of the spectrometer, such as perhaps vibrating a mirror, would have to be implemented.

V. EXPERIMENTS ON CARBON MONOXIDE ADSORBED ON NICKEL

We chose to study the system of carbon monoxide adsorbed on single crystals of nickel for several reasons. Since this system has been studied for many years using many different experimental techniques, we are able to compare our results to many published results. In addition, carbon monoxide has a large dynamic dipole moment, which makes the C=O stretching vibration easy to see using infrared techniques; thus, most infrared experiments on surfaces have studied systems with adsorbed carbon monoxide. In addition, the catalytic hydrogenation of carbon monoxide over nickel to form methane is a reaction of practical importance in the chemical industry.

This chapter is organized as follows. In Section A, we briefly summarize a small subset of the published work on the system of CO adsorbed on Ni(100). Our experimental procedures are discussed in Section B, followed by a discussion of our observed emission spectra for CO adsorbed on nickel in Section C. In Section D, we explain some of the proposed mechanisms for frequency shifts in vibrational spectra as a function of coverage, while we discuss in Section E some of the possible damping mechanisms which may cause our observed linewidths.

A. Summary of Previous Work

Some of the earliest work on chemisorbed carbon monoxide was performed by Eischens, et al.[51] in 1956. They observed the infrared transmission spectra of CO adsorbed on small particles of copper, nickel, palladium, and platinum supported on silica. For CO on Ni, they observed one band at wavelengths of 4.8 to 4.9 microns (2040-2083 cm^{-1}), and a second band at 5.1 to 5.3 microns (1890-1960 cm^{-1}). By comparing with infrared data on metal carbonyls, they made the assignment of bands in 4.8 to 5.0 micron (2000 to 2080 cm^{-1}) region to CO bonded through the carbon atom to single metal atoms, while bands in the region 5.0 to 5.4 microns (1850-2000 cm^{-1}) were assigned to CO molecules bridge bonded between two metal atoms. As the amount of CO on the surface was increased, the bands showed a slight shift to shorter wavelengths which was attributed to interaction effects among the molecules.

Kroeker et al.[52] used inelastic electron tunneling spectroscopy to study the system of CO adsorbed on alumina-supported nickel in a tunnel junction. They observed three vibrations which were attributed to linear species: the CO stretch at 2069 cm^{-1}, the Ni-C stretch at 480 cm^{-1}, and a metal-CO bending mode at 367 cm^{-1}.

The adsorption of CO on Ni(100) was studied by Tracy[53], using LEED, Auger, and work function measurements to measure the temperature versus coverage phase diagram of the system. His LEED results were completely reversible for CO pressures between 10^{-9} torr and 10^{-4} torr, with temperatures less than 475K. For CO coverage on the surface of 0.5 monolayer, he observed a c(2x2) LEED pattern, which changed to a "hexagonal" pattern when the coverage was increased to 0.61 monolayer

and then a compressed "hexagonal" pattern at a coverage of 0.69 monolayer.

Angular resolved photoemission measurements of CO on Ni(100) by Allyn et al.[54] established that the adsorbed CO molecule is perpendicular to the surface within an uncertainty of order $\pm 5^{o}$, with the carbon end of the molecule closest to the substrate. Upon chemisorption of the CO on the surface, they observe two additional energy bands at 8 and 11 eV below the Fermi level. The level at -8eV was identified as a combination of states derived from the 5σ and 1π of the CO molecule. Gustafsson et al.[55] had previously assigned the level at -11 eV to the 4σ level of the CO molecule.

Electron energy loss spectroscopy experiments have previously observed the vibrational modes of CO on Ni(100). With resolution of ~80 cm^{-1}, Andersson[56] has observed vibrations at 2069 cm^{-1} for the carbon-oxygen stretch and 480 cm^{-1} for the carbon-nickel stretch for a c(2x2) overlayer of CO on Ni(100) at 293K. By comparing with the CO stretching vibrations of gaseous $Ni(CO)_4$, the CO modes for the c(2x2) overlayer are attributed to molecules linearly bonded to the nickel atoms. The higher frequency peak also shows a small shoulder at 1936 cm^{-1}, which is thought to be related to disorder in the c(2x2) structure. At the lower exposure of 0.3L CO where no ordered CO structure was observed, the room temperature EELS spectrum shows clearly two high frequency peaks, 2065 and 1932 cm^{-1}, attributed to CO in linear and bridge bonded sites, respectively, and one lower frequency peak at 480 cm^{-1}, which is the C-Ni vibration for the linear site.

Bertolini and Tardy[57] have also measured EELS spectra of CO on

Ni(100). For coverage $\theta_{CO} \simeq 0.5$ monolayer, they observe intramolecular vibrations at 2015 and 1935 cm^{-1} and carbon-metal stretch at 460 and 365 cm^{-1} for on-top and bridge sites, respectively. Unlike Andersson's data, the intensities of the lines from the linear and bridge sites in their spectra are quites similar, for a saturation coverage of CO on Ni(100) at room temperature.

B. Experimental Procedures

We have observed thermally emitted infrared radiation from carbon monoxide adsorbed on two different single crystal samples of nickel. Both crystals were obtained from the Materials Research Laboratory of Cornell University. One was cut at about 8^{o} from a (100) surface, while the other was within 1^{o} of a (100) surface. Each crystal was 0.5 cm high x 1.5 cm wide x 1 mm thick. These dimensions were chosen so that the sample, when turned at grazing incidence and imaged by the KRS-5 lens, would completely fill the entrance slit of the cold grating spectrometer.

For each set of measurements, the nickel single crystal was mounted on a sample manipulator in the method described in Chapter III. The crystal was cleaned by repeated cycles of argon ion bombardment, annealing, and oxidation to remove residual carbon. Since these samples did not have much sulfur contamination, it was possible to remove sulfur from the surface by sputtering (1 μA at 1000 eV). After sputtering, carbon was usually left on the surface, most of which could be removed by simply annealing the sample at 650^{o} C for 10 minutes. Any residual carbon was then removed by oxidation in 2×10^{-8} torr of oxygen at 600^{o} C. If the oxidation treatment resulted in an oxide forming on the

surface, the cleaning cycle, beginning with the argon ion sputtering, was begun again. The sample was considered to be clean when retarding field Auger spectroscopy indicated that contamination from sulfur, carbon, and oxygen was less than 0.1 monolayer. Although the clean Ni(100) single crystal gave very sharp LEED spots, we have observed only a fuzzy c(2x2) pattern from an overlayer of carbon monoxide on that surface.

To obtain an infrared spectrum, the voltage at the output of the detector circuit was measured as a function of the grating angle, with one second of signal integration per point. An infrared spectrum of the clean nickel surface was measured to serve as a reference. For measurements of the C=O stretching vibration, the sample was exposed to doses of 0.05L or 0.10L CO by letting 10^{-8} torr of CO gas, of 99.5% purity, into the UHV system through a leak valve for 5 or 10 seconds. The spectra of nickel with CO were then divided by the reference spectrum to eliminate variations in blackbody intensity and optical efficiency of the instrument. After subtraction of a constant background, the results from 3 or 4 independent experiments, with spectral scans of one minute each, were averaged together to yield a series of spectra. Fig. 26 shows the observed spectra of the carbon-oxygen stretching vibration for 0.2L and 0.5L CO on Ni(100), while Fig. 27 shows a series of spectra of the same vibrational mode on Ni(100)8^{0}. Our signal to noise ratio permits the routine measurement of the signal from as little as 0.05L CO on Ni.

To measure the carbon-nickel stretching vibration of CO on Ni(100), a similar procedure was followed, using a grating suitable for

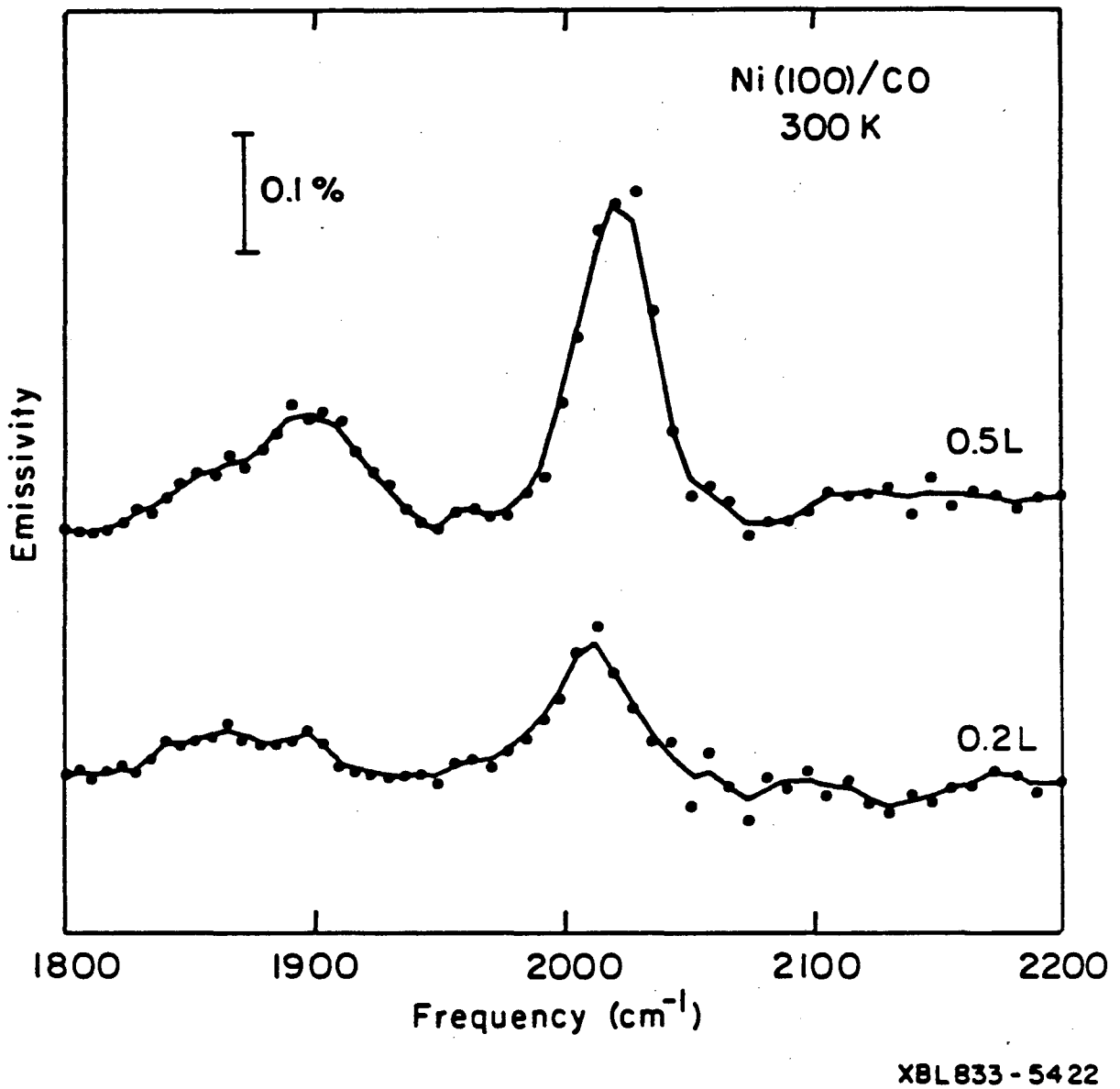

Fig. 26. Observed spectra of C=O stretch on Ni(100) for 0.2 and 0.5L exposure to CO. The vertical bar indicates 0.1% absolute emissivity. The instrumental resolution was 20 cm^{-1}.

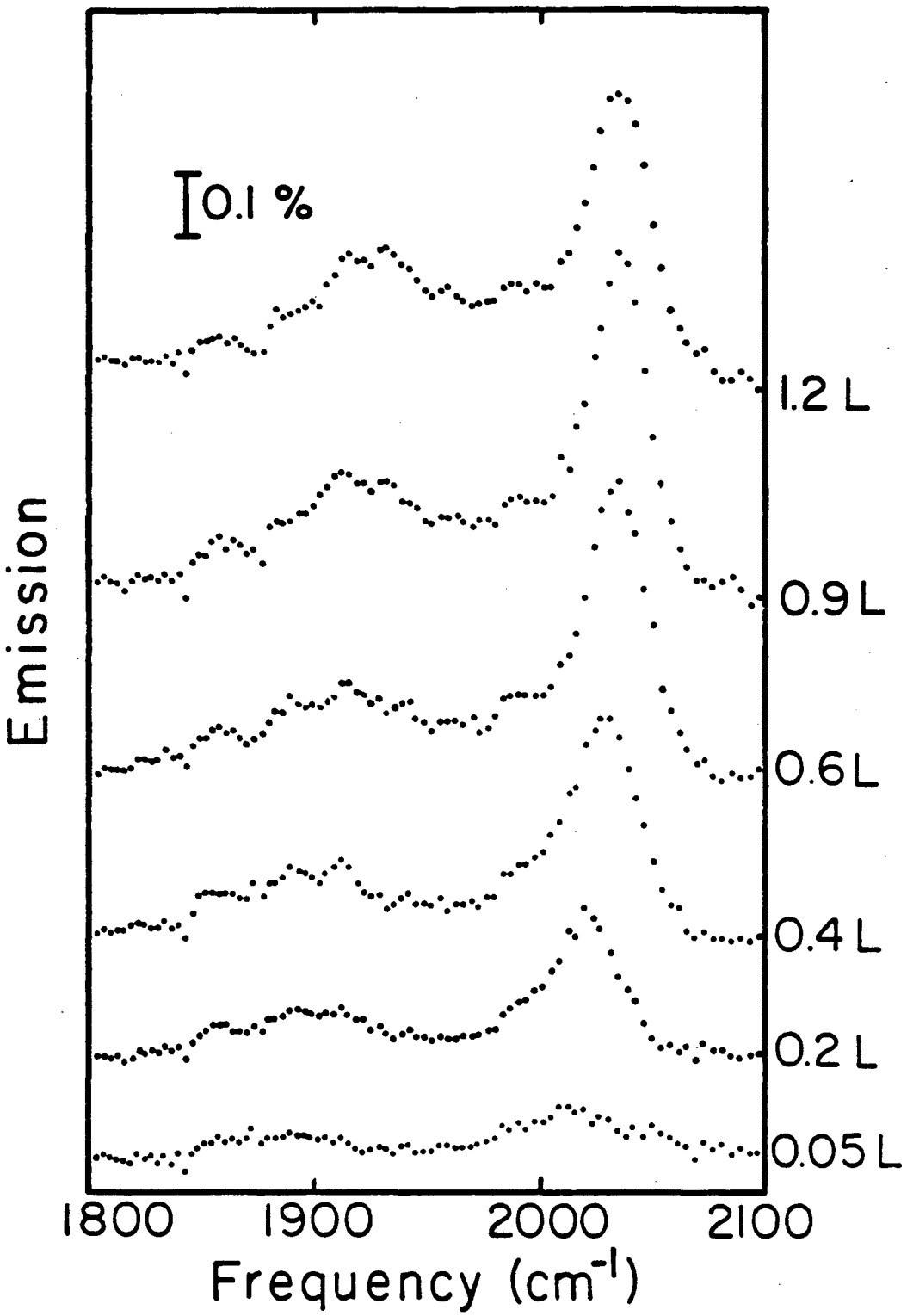

Fig. 27. Observed spectra of C=O stretch on stepped Ni(100)8°. The instrumental resolution was 15 cm^{-1}.

measurements of lower frequencies. Since the surface signal due to this mode is about ten times weaker than that of the carbon-oxygen vibration, a correspondingly longer integration time was required. The spectrum shown in Fig. 28 is the result of five independent experiments, with a total integration time of about 30 seconds per point.

C. Discussion of Observed Spectra

In the high frequency range near 2000 cm^{-1}, two emission bands from the carbon-oxygen stretching vibration occur. The stronger peak, in the range 2010-2035 cm^{-1}, has a width of about 35 cm^{-1} almost independent of coverage. The weaker band in the range of 1850-1930 cm^{-1} has a width of 60 to 80 cm^{-1}. Peaks in these two frequency ranges have been attributed by Eischens et al.[51] to CO molecules in on-top sites and in bridge sites, respectively, as discussed in Section A.

Figures 29 and 30 show the peak positions and integrated intensities of the two C=O bands on Ni(100)8^{0} as a function of coverage. Before calculating the areas of the bands, a quadratic baseline was subtracted; uncertainty in the determination of this baseline is the primary source of error in these values. For both bands, the peak frequencies shift continuously upward with increasing exposure, reaching a total shift of 25 cm^{-1} for the on-top site at an exposure of about 0.5L, and a total shift of 35 cm^{-1} for the bridge site at an exposure of about 0.8L. At saturation, the on-top site has a little over twice the intensity of the bridge site. These shifts are comparable to those previously observed on Ni(100)[57,58], but they are much smaller than those observed on Ni(111)[57,59,60] and on evaporated nickel films.[19,61] Both lines seem to reach their maximum intensity at an exposure of 0.8L

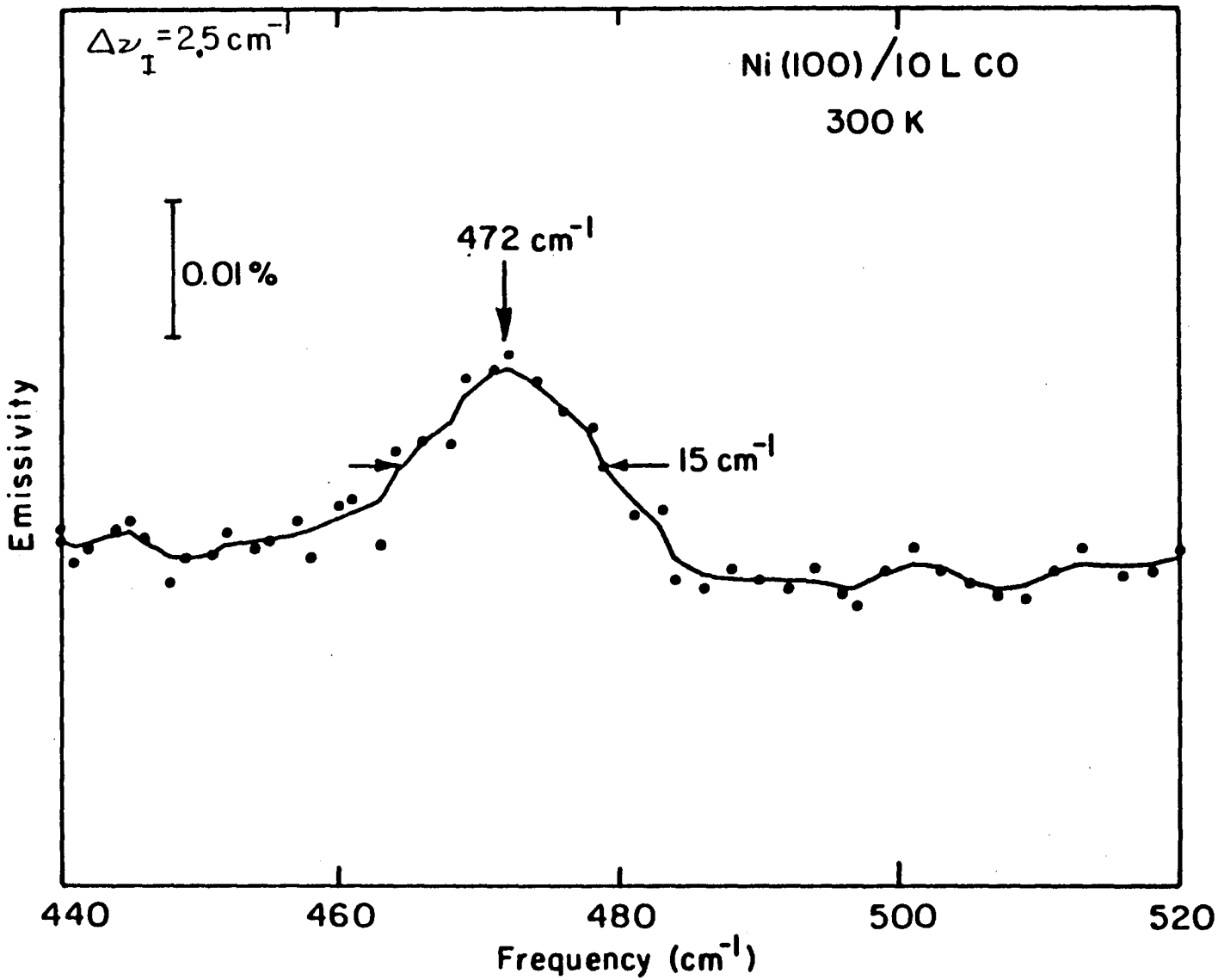

Fig. 28. Observed spectrum of C-Ni stretch on Ni(100).

XBL 833-5421

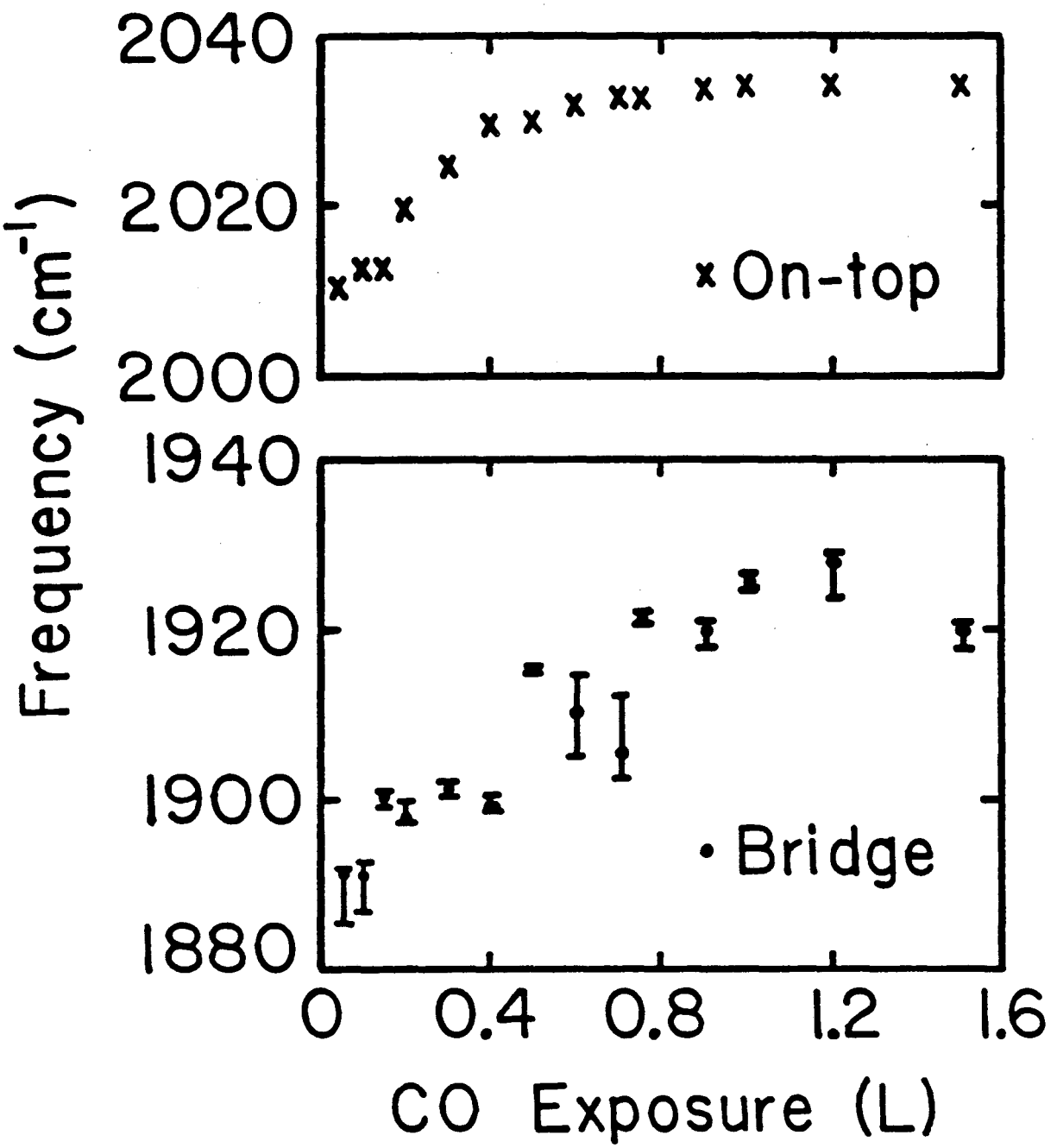

XBL 828-9599

Fig. 29. Peak positions for on-top and bridge sites as a function of CO exposure for CO on Ni(100)8°.

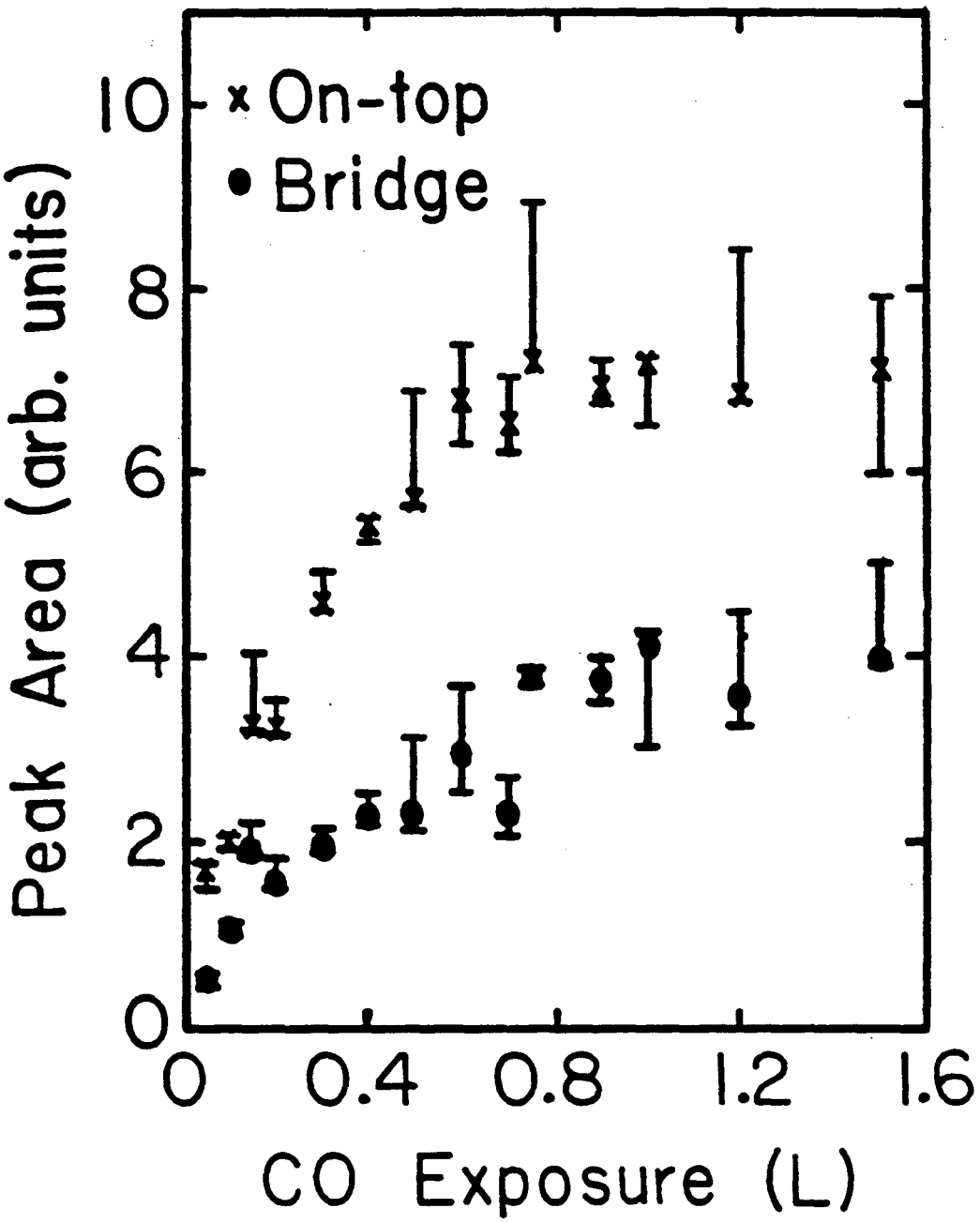

XBL 828-9600

Fig. 30. Peak areas for on-top and bridge sites as a function of CO exposure for CO on Ni(100)8°.

CO, which presumably corresponds to a saturation coverage on the surface of ~0.5 monolayer at room temperature.

Our emission apparatus is the first surface apparatus with sufficient sensitivity and resolution to be able to measure the linewidth of the carbon-nickel vibration of CO on Ni(100). The frequency of the observed C-Ni vibration at 472±5cm^{-1} agrees well with previous EELS results, which were discussed above.[56,57] With instrumental resolution of 2.5 cm^{-1}, the observed linewidth, measured full width at half maximum (FWHM), is 15 ±2cm^{-1}. In the frequency range between 440 and 520 cm^{-1}, we measure only one vibrational line which we attribute to the carbon-nickel bond of CO molecules in an on-top sites on Ni(100). The adsorbate-substrate vibration for CO molecules in bridge sites may be at lower frequencies outside the range of the present measurement. Other possible reasons for not observing it here are that its intensity may be too weak or its width too broad.

D. Causes of Frequency Shifts with Coverage

The observed frequency shifts with coverage of the carbon-oxygen stretching mode of CO on nickel may have several causes. Although frequency shifts can occur as molecules change their adsorption sites on the surface, the observed shifts are not large enough for this to be the case here. We will discuss below two more likely explanations: (1) Changes in the back-donation of electrons in the adsorbate bonding. (2) Dipole-dipole interactions.

Blyholder has described the chemisorption bonding of CO to metals using Huckel molecular orbitals for the metal-carbon-oxygen bonds.[62] The bonding is thought to occur by donation of electrons from the 5σ

bonding orbital of CO to the metallic d orbitals, with back donation of electrons from the d bands of the metal to the $2\pi^*$ antibonding orbital of CO, thus decreasing the binding energy of the carbon to the oxygen. This explains the lowering of the C=O stretching frequency upon chemisorption, compared with that of the CO molecule in free space. As the coverage of adsorbed CO molecules increases, the competition for the electrons from the metal increases; less charge is available to put into each $2\pi^*$ antibonding orbital, causing the carbon to become more tightly bound to the oxygen so that the frequency of the vibration increases.

Dipole-dipole interactions between the adsorbed CO molecules on a metal surface can also cause the shift of the C=O band to higher frequencies with coverage. This effect was first considered by Hammaker et al. who calculated the direct dipole-dipole interactions of different excited molecules.[63] Although Mahan and Lucas also took into account the image charge screening by the metal substrate, they obtained a frequency shift of about 10 cm^{-1}, which is about one third of the experimental value, because they did not consider the interaction of a dipole with its own image dipole properly and used the wrong value for the polarizability.[64] By including this latter effect, Scheffler[65] was able to obtain a frequency shift which agrees with experiments for the system of CO adsorbed on Pt(111).

For the system of CO on Pt(111), Crossley and King performed an infrared reflection-absorption experiment in which they were able to separate the frequency shift due to changes in the chemical bonding from the contribution of dipole-dipole coupling.[66] While keeping the total coverage on the surface constant, they observed frequency shifts of the

infrared bands as they varied the isotopic mixtures of $C^{13}O^{16}$ and $C^{12}O^{16}$ on the surface. Since the total coverage was constant and the isotopes are chemically identical, the observed frequency shifts could not be due to changes in the chemical bonding, but must result from the dipole-dipole coupling interaction. Since they obtained the same frequency shift for the isotope experiment in which the coverage was held constant as for increasing coverage of only one isotope, they concluded that the entire 35 cm^{-1} shift observed with increasing coverage for $C^{12}O^{16}$ could be attributed to dipole-dipole coupling.

For the system of CO on Ni(111), Campuzano and Greenler measured the C=O stretching vibration using infrared reflection-absorption spectroscopy.[60] Although they attempted to do an isotopic experiment similar to that of Crossley and King, their bands for CO on Ni(111) were so wide, with a FWHM of 50 cm^{-1}, that they could not measure the frequency shifts with the variation of the isotopic mixture. Instead, they did a theoretical estimate of the shift due to the dipole-dipole coupling interaction and concluded that that shift was small compared to the shift resulting from bonding to different crystallographic sites for CO on Ni(111).

A theoretical calculation of the dipole-dipole coupling shift by Persson and Ryberg[67] for CO on Ru(001) agrees very well with the shift of +40 cm^{-1} observed by Pfnur et al.[68]. Woodruff et al.[69] have tabulated the dipole and chemical shifts for CO adsorption from experiments on isotopic mixtures. The dipole shifts for CO adsorbed on copper, platinum, and palladium are all in the range 26-53 cm^{-1}. Clearly, our observed frequency shift for the CO stretch on nickel is

also in this range, so it is possible that the frequency shift which we observe for CO on Ni(100) is due completely to dipole-dipole coupling. This cannot be confirmed, however, without performing the isotope experiment.

E. Causes of Linewidths of Vibrational Modes

The linewidths of the vibrational modes of adsorbed molecules are many orders of magnitude higher than the linewidths of free molecules, probably indicating very efficient transfer of energy from the molecule to the surface. The study of these linewidths for adsorbed molecules can give important insight into the processes which damp the vibration and cause the energy transfer between the molecule and the surface. Knowledge of the damping processes may also give information on adsorbate-induced electronic structure and on the rate of surface reactions.

One possible explanation for the large linewidths observed for vibrational modes of molecules adsorbed on surfaces is that the lines are inhomogeneously broadened. If the bonding sites on the surface are not identical, the molecules will have different environments with different bond strengths, leading to a broader vibrational line. Indirect evidence, however, suggests that the lines are not inhomogeneously broadened. Although even a polished, annealed single crystal metal sample may have some step and kink sites, an unannealed, evaporated metal film is expected to have a higher degree of site heterogeneity. Nevertheless, the observed linewidth of the C=O stretching vibration for the on-top site is seen in this emission experiment to be 31 cm^{-1}, when corrected for the instrumental

resolution; the same linewidth is obtained for the evaporated nickel film sample in the direct absorption experiment.[61] The fact that the linewidths are the same for these two very different samples indicates that site heterogeneity is probably not an important source of the line broadening.

If the line is homogeneously broadened, its width may indicate a vibrational decay lifetime. Persson and Persson[70] have calculated the vibrational lifetime for CO adsorbed on Cu(100). When they assume that the damping mechanism is the excitation of electron-hole pairs in the metal by the long range dipole field of the vibrating molecule, they obtain a lifetime which is two orders of magnitude larger than the value extracted from measurements of the linewidth. They then propose the model in which the $2\pi^*$ antibonding orbital of the adsorbed molecule results in an adsorbate induced resonance state near the Fermi energy, ε_F. Then, as the molecule vibrates, this resonance state moves up and down in energy near ε_F and charge flows between the CO $2\pi^*$ orbital and the metal, exciting electron hole-pairs in the metal. Using this model, they obtain the following equation for the lifetime, τ:

$$1/\tau = 2\pi\Omega\,(\delta n_a)^2 . \qquad (69)$$

Here Ω is the frequency of the vibration and (δn_a) is the fluctuation in the number of electrons in the orbital $|a\rangle$ during one vibration. The quantity (δn_a) can be obtained from experimental measurements of the dynamic dipole moment of the molecule. For the C=O vibration on Cu(100), they obtain $\tau_{(\text{theory})}=1.8 \times 10^{-12}$ sec., which agrees well with the value extracted from experiment, $\tau_{(\text{experiment})}=(3\pm1) \times 10^{-12}$ sec. For the system of methoxide on Cu(100), Persson and Ryberg[71] have a

similar explanation for the experimental data. They argue that electron hole pairs are excited because a resonance near the Fermi level fills and empties during the vibration.

A simple extrapolation of this theory of excitation of electron-hole pairs to the C-Ni line of CO on Ni(100) would give a linewidth about an order of magnitude narrower than our experiment indicates. Although this theory may be adequate for explaining the linewidth of the higher frequency C=O mode, it probably does not include the dominant damping mechanism for the lower frequency adsorbate-substrate mode.

Another damping mechanism for the vibrational lines of the adsorbed molecule is the excitation of phonons in the substrate. For a metal substrate, Metiu and Palke[72] calculated the linewidth assuming that the broadening mechanism was coupling between the vibration of the atom and the phonons of the lattice. Their calculation indicated that, for the case where the molecular vibrational frequency was much larger than phonon frequencies in the metal, such as the C=O stretching vibration on nickel, the theoretical linewidth was two orders of magnitude smaller than the experimental linewidth. Thus, they concluded that coupling between the adsorbate molecules and the phonons was not important. For the carbon-nickel bond observed in this emission experiment, however, the frequency of the vibration is low enough that it could decay by exciting only two or three substrate phonons. It then seems likely that coupling to the nickel phonons may be an important damping process.

It is also possible that the linewidth may be dominated by the phase relaxation (T_2) process, which destroys the coherent nature of the interaction between the adsorbed molecule and the surface, thus

broadening the line without changing its frequency.[73] These dephasing effects will dominate the broadening of the line for species with long lifetimes which are weakly coupled to the solid surface. Several mechanisms can cause these dephasing effects: (1) Dephasing of the interaction energy between the molecule and surface due to fluctuation of the molecular arrangement and the corresponding effective dipole moment. (2) Excitation-induced surface migration of the adsorbed molecules, leading to elastic collisions between molecules. (3) Other surface-induced broadening mechanisms involving phonon bandwidth and anharmonic coupling of the surface potential. There are no quantitative predictions of the magnitude of the dephasing effects for the vibrational excitations of adsorbates.

VI. CONCLUSIONS

We have demonstrated that the technique of infrared emission spectroscopy can be used to measure the vibrational modes of molecules adsorbed on clean, single crystal metal surfaces. An infrared emission apparatus, consisting of a liquid helium temperature grating spectrometer coupled to a conventional ultrahigh vacuum system, has been built and used to measure the vibrational modes of CO on Ni(100). This is the first apparatus which has had sufficient spectral range, resolution and sensitivity to measure the linewidths of both the intramolecular vibration and the very weak adsorbate-substrate mode for this system. Now that the linewidth of the carbon-nickel vibration has been measured, perhaps more theoretical and experimental work on the linewidths of vibrational modes will follow, yielding additional insight into the processes damping the modes and a better understanding of the chemical bonding between adsorbed molecules and the surface.

Several additional experiments are planned at this time to extend the work which has been presented here on CO on Ni(100). We plan to measure spectra of both the C=O and C-Ni stretching vibrations for a c(2x2) overlayer of CO on Ni(100). We would like to measure the linewidth of the low frequency mode as a function of temperature above 300K. Finally, we may also try to measure the frequency and linewidth of the low frequency mode using a different isotope, $C^{13}O^{16}$.

Although we have already demonstrated the usefulness of the infrared emission technique, further development of the apparatus should yield even higher sensitivity, with the possibility of observing fractional surface signals of less than 10^{-4}. The emission approach is

particularly useful for the observation, with high resolution, of low frequency vibrations in the range 100-800 cm^{-1} where most other methods have technical difficulties. With the addition of modulation to the emission apparatus, it should be capable of approaching the photon noise limit, enabling the observation of both the frequencies and linewidths of many other adsorbate-substrate vibrations for a wide variety of chemical systems.

ACKNOWLEDGMENTS

I would like to thank my thesis advisor, Prof. Paul L. Richards, for the idea of building a cold spectrometer to measure infrared emission from adsorbed molecules. He taught me how to design and build apparatus. I would also like to thank him for his continued support, encouragement, patience, and many ideas as the work progressed.

I would like to thank Roger Tobin for working with me on this project. He built the detector circuit and the polarizer assembly. His many other contributions to this project are too numerous to enumerate here. His help has been invaluable in making this experiment possible.

I would also like to thank many other people at Berkeley for their help during the course of this work, particularly other members of our research group. Bob Bailey, Steve McBride, and Jim Bonomo taught me many things about infrared spectroscopy and cryogenics. Bill Challener advised me on adapting the computer software to run this experiment. Mark Hueschen answered many questions on photoconductive detectors and low noise amplifiers. Harry Levinson acted as a consultant on surface science and sample cleaning.

I would also like to acknowledge grants from the Bell Laboratories Graduate Research Program for Women while I have been in graduate school. I have had much encouragement from many friends at Bell Laboratories, particularly Dr. Neville Smith and Dr. Gunther Wertheim.

This work was supported by the Director, Office of Energy Research, Office of Basic Energy Sciences, Materials Sciences Division of the U. S. Department of Energy under contract No. DE-AC03-76SF00098.

REFERENCES

1. P. A. Redhead, J. P. Hobson, and E. V. Kornelsen, The Physical Basis of ULtrahigh Vacuum (Chapman and Hall, London, 1968).
N. W. Robinson, The Physical Principles of Ultrahigh Vacuum Systems and Equipment (Chapman and Hall, London, 1968).

2. G. Ertl and J. Kuppers, Low Energy Electrons and Surface Chemistry (Verlag Chemie, Weinheim, 1974).

3. R. F. Willis, ed., Vibrational Spectroscopy of Adsorbates (Springer-Verlag, Berlin, 1980).

4. H. Ibach, H. Hopster, and B. Sexton, Applic. of Surf. Sci. 1, 1 (1977).

5. Gabor A. Somorjai, Chemistry in Two Dimensions: Surfaces (Cornell University Press, Ithaca, NY, 1981).

6. H. Ibach, J. Electron Spectrosc. and Relat. Phenom. 30, 237 (1983).

7. P. K. Hansma, Phys. Rep. 30C, 145 (1977).

8. See references in H. Seki, J. Electron. Spectrosc. and Relat. Phenom. 30, 287 (1983).

9. C. K. Chen, A. R. DeCastro, Y. R. Shen, and F. De Martin, Phys. Rev. Lett. 43, 946 (1979).
C. K. Chen, T. F. Heinz, D. Ricard, and Y. R. Shen, Phys. Rev. Lett. 46, 1010 (1981).

10. Alan Campion, J. Keenan Brown, and V. M. Grizzle, Surf. Sci. 115, L153 (1982).

11. J. D. Fedyk, P. Mahaffy, and M. J. Dignam, Surf. Sci. 89, 404 (1979).

12. Y. J. Chabal and A. J. Sievers, Phys. Rev. Lett. 44, 944 (1980).

13. F. Trager, H. Coufal, and T. J. Chuang, Phys. Rev. Lett. 49, 1720 (1982).

14. D. K. Lambert, J. Electron Spectrosc. and Relat. Phenom. 30, 59 (1983), and to be published.

15. M. L. Hair, Infrared Spectroscopy in Surface Chemistry (Dekker, New York, 1967).

L. H. Little, Infrared Spectra of Adsorbed Species (Academic Press, London, 1966).

16. See references in J. Darville, J. Electron Spectrosc. and Relat. Phenom. 30, 247 (1983).

17. Robert G. Greenler, J. Chem. Phys. 44, 310 (1966).

18. Robert G. Greenler, J. Chem. Phys. 50, 1963 (1969).

19. R. B. Bailey, T. Iri, and P. L. Richards, Surf. Sci. 100, 626 (1980).

20. J. F. Blanke, S. E. Vincent, and John Overend, Spectrochim. Acta 32A, 163 (1976).

J. F. Blanke and John Overend, Spectrochim. Acta 32A, 1383 (1976).

21. D. Kember, D. H. Chenery, N. Sheppard, and J. Fell, Spectrochim. Acta 35A, 455 (1979).

22. M. Primet, P. Fouilloux, and B. Imelik, Surf. Sci. 85, 457 (1979).

23. M. Primet, P. Fouilloux, and B. Imelik, J. Catal. 61, 553 (1980).

24. L. M. Gratton, S. Paglia, F. Scattaglia, and M. Cavallini, Appl. Spectrosc. 32, 310 (1978).

25. D. L. Allara, D. Teicher, and J. F. Durana, Chem. Phys. Lett. 84, 1 (1981).

26. John David Jackson, Classical Electrodynamics, 2nd Ed. (Wiley, New York, 1975), p. 335.

27. J. D. E. McIntyre and D. E. Aspnes, Surf. Sci. 24, 417 (1971).

28. W. Lukosz, J. Opt. Soc. Am. 71, 744 (1981).

29. D. L. Allara, unpublished results.

30. Robert Brian Bailey, Ph.D. Thesis, University of California, Berkeley, 1978.

31. J. R. Beattie and G. K. T. Conn, Phil. Mag. 46, 989 (1955).

32. F. Reif, Fundamentals of Statistical and Thermal Physics (McGraw Hill, Inc., New York, 1965), pp. 381-388.

33. Ibid., p. 346.

34. R. C. Jones, in Advances in Electronics (Academic Press, New York, 1953), Vol. 5, pp. 1-96.

35. Max Born and Emil Wolf, Principles of Optics (Pergamon Press, Oxford, 1975), 5th ed., pp. 401-414.

36. Rockwell International Co. Detector Measurements Data Sheet.

37. Robert John Bell, Introductory Fourier Transform Spectroscopy (Academic Press, New York, 1972), pp. 23-25.

38. M. Czerny and A. F. Turner, Z. Physik, 61, 792 (1930).
M. Czerny and V. Plettig, Z. Physik, 61, 590 (1930).

39. W. R. McGrath and P. L. Richards, Rev. Sci. Instrum., 53, 709 (1982).

40. Peter R. Bratt, in Semiconductors and Semimetals, edited by R. K. Willardson and Albert C. Beer (Academic Press, New York, 1977), Vol. 12, Chap. 2, pp. 39-142.

41. E. L. Dereniak, R. R. Joyce, and R. W. Capps, Rev. Sci. Instrum., 48, 392 (1977).

42. C. Doland, P. O'Neill, and A. Ignatiev, J. Vac. Sci. Technol. 14, 259 (1977).

43. E. E. Haller, M. R. Hueschen, and P. L. Richards, Appl. Phys. Lett. 34,495 (1979).

44. M. R. Hueschen (private communication).

45. R. H. Kingston, Detection of Optical and Infrared Radiation (Springer-Verlag, Berlin, 1978).

46. E. G. Loewen, M. Neviere, and D. Maystre, Appl. Opt. 16, 2711 (1977).

47. F. M. Hoffmann and A. M. Bradshaw, Proceedings of the Seventh International Vacuum Congree and the Third International Conference on Solid Surfaces (Vienna, 1977), p. 1167.

A. M. Bradshaw and F. M. Hoffmann, Surf. Sci. 72, 513 (1978).

48. Hinds International, Inc., P. O. Box 4327, Portland, Oregon, 97208.

49. W. G. Golden, Douglas S. Dunn, and John Overend, J. Catal. 71, 395 (1981).

John Overend, J. Electron Spectrosc. and Relat. Phenom. 30, 1 (1983).

50. R. Ryberg, Chem. Phys. Lett. 83, 42 (1981).

51. R. P. Eischens, W. A. Pliskin, and S. A. Francis, J. Chem. Phys., 22, 1786 (1954).

R. P. Eischens, S. A. Francis, and W. A. Pliskin, J. Phys. Chem., 60, 194 (1956).

52. R. M. Kroeker, W. C. Kaska, and P. K. Hansma, J. Chem. Phys. 74, 732 (1981).

53. J. C. Tracy, J. Chem. Phys., 56, 2736 (1972).

54. C. L. Allyn, T. Gustafsson, and E. W. Plummer, Chem. Phys. Lett. 47, 127 (1977).

55. T. Gustafsson, E. W. Plummer, D. E. Eastman, and J. L. Freeouf, Sol. St. Commun., 17, 391 (1975).

56. S. Andersson, Sol. St. Commun., 21, 75, (1977).

57. J. C. Bertolini and B. Tardy, Surf. Sci., 102, 131 (1981).

58. M. J. Dignam, in Vibrations at Surfaces: Proceeding of an International Conference at Namur, Belgium, R. Caudano, J.-M. Gilles, and A. A. Lucas (Eds.), (Plenum, New York, 1982).

59. W. Erley, H. Wagner, and H. Ibach, Surf. Sci., 80, 612 (1979).

60. J. C. Campuzano and R. G. Greenler, Surf. Sci., 93, 301, (1979).

61. H. J. Levinson, R. G. Tobin, and P. L. Richards, J. Electron Spectrosc. and Relat. Phenom. 30, 65 (1983).

62. George Blyholder, J. Phys. Chem., 68, 2772 (1964).

63. R. M. Hammaker, S. A. Francis, and R. P. Eischens, Spectrochim. Acta, 21, 1295 (1965).

64. G. D. Mahan and A. A. Lucas, J. Chem. Phys., 68, 1344, (1978).

65. M. Scheffler, Surf. Sci., 81, 562 (1979).

66. Alison Crossley and David A. King, Surf. Sci., 68, 528 (1977).

67. B. N. J. Persson and Roger Ryberg, Phys. Rev. B24, 6954 (1981).

68. H. Pfnur, D. Menzel, F. M. Hoffman, A. Ortega, and A. M. Bradshaw, Surf. Sci., 93, 431 (1980).

69. D. P. Woodruff, B. E. Hayden, K. Prince, and A. M. Bradshaw, Surf. Sci. 93, 431 (1980).

70. B. N. J. Persson and M. Persson, Sol. St. Commun., 36, 175 (1980).

71. B. N. J. Persson and R. Ryberg, Phys. Rev. Lett. 48, 549 (1982).

72. Horia Metiu and William E. Palke, J. Chem. Phys. 69, 2574 (1978).

73. Thomas F. George, Jui-teng Lin, Kai-Shue Lam, and Cheng-hui Chang, Optic. Engin., 19, 100, (1980).

This report was done with support from the Department of Energy. Any conclusions or opinions expressed in this report represent solely those of the author(s) and not necessarily those of The Regents of the University of California, the Lawrence Berkeley Laboratory or the Department of Energy.

Reference to a company or product name does not imply approval or recommendation of the product by the University of California or the U.S. Department of Energy to the exclusion of others that may be suitable.

TECHNICAL INFORMATION DEPARTMENT
LAWRENCE BERKELEY LABORATORY
UNIVERSITY OF CALIFORNIA
BERKELEY, CALIFORNIA 94720